Quantified phenotype analysis in a cell model for Autosomal Dominant Retinitis Pigmentosa

Rana A A Alghamdi

A thesis submitted for the degree of

Doctorate of Philosophy in Biological Sciences

School of Biological Sciences University of Essex

"The seeker after truth is not one who studies the writings of the ancients and, following his natural disposition, puts his trust in them, but rather the one who suspects his faith in them and questions what he gathers from them, the one who submits to argument and demonstration, and not the sayings of a human being whose nature is fraught with all kinds of imperfection and deficiency"

Abu Ali Ibn al-Haytham (Alhazen)

Abstract

Modern cell biology relies greatly on microscopy to assess distribution and dynamics of fluorescently labelled cellular proteins. Quantified image analysis allows not only measurement of clear differences between individual phenotypes and time points, but also discovery of subtle changes which are not obvious to an observer by visual inspection. In this dissertation, we quantitatively characterise wild type and mutations P23H/A/L in rhodopsin in a cellular model for autosomal dominant retinitis pigmentosa in stable HEK 293S cell lines and in GMK cells. Autosomal dominant retinitis pigmentosa is a genetic disorder which can lead to photoreceptor cell death and result in reduced vision and complete blindness. Endoplasmic Reticulum chaperone calnexin was also quantified from both immune-labelled fixed cells, and from transient co-transfection of live cells. The clinically relevant severity of rhodopsin mutations was in keeping with the phenotypes of the cellular model. The severe mutation P23H showed the lowest volume of rhodopsin-GFP in both cell lines in comparison to wild-type. We also reported a significantly higher calnexin volume in HEK293 and GMK expressing P23H rhodopsin (with $p<0.05$). Less severe mutants had a phenotype more similar to wildtype. Colocalisation was assessed using a simple approach of overlapping volume. As co-expression of rhodopsin and calnexin during time-lapse acquisition induced cytotoxicity and accelerated cellular death, we assessed phototoxicity caused by blue light illumination. We quantified motility and division rates in PC3 and GMK mammalian cell cultures, respectively. A surprisingly low phototoxicity threshold of 13.9 J/cm^2 was determined for imaging unlabelled GMK cells without inducing mitotic delay. To assess the production of reactive oxygen species, which are key to phototoxicity in fluorescence microscopy, the end-product hydrogen peroxide was monitored using a ratiometric biosensor. Finally, all findings are synthesised as practical guidelines for end users.

Acknowledgments

In the name of Allah, the Most Gracious and the Most Merciful, all praise to Allah for the strength He has granted me and His blessing in completing this thesis.

The following document summarizes years' worth of effort, frustration and achievement. However, there are several people in whom I am indebted for their contribution during the research, study and writing of this thesis.

I am forever grateful to my supervisor Dr. Philippe Laissue for having accepted to be my PhD supervisor and for having introduced me to the intricate world of bioimaging. His patience, guidance, moral support and effort were essential to the birth of this thesis and to my formation as a researcher. He has gone beyond the call of a thesis advisor to assume the role of an academic father, making an effort to not only explain the concepts of my project: he spawned the conception, research and writing of this thesis by his wealth of knowledge in the field of microscopy, bioimaging, cell biology and much more. Without his help and disposition, this thesis would not have been possible.

I am also grateful to Dr Phil Reeves my PhD advisor for his constant support and valuable feedback during supervisory meetings; Dr. Chikwado A Opefi for his help with ADRP stable cell lines; Dr Marino Exposito-Rodriguez for generously sharing his time and knowledge with regards to HyPer and the phototoxicity project.

I would also like to thank my friend Dr. Ashjan Shami, for listening, offering me advice, and supporting me through this entire process.

I would like to express my sincere thanks to Mrs Brenda Foulds for her generous time in proofreading.

I would like also to thank King Abdul Aziz University for financially sponsoring my PhD.

Deepest gratitude goes to my beloved parents and my sisters and brothers who have supported me through all of my adventures in life, I know it was not easy to be related to a rebel girl like me in a very conservative society where it is very limited what a female can or cannot do.

Last, but not least, I would like to dedicate this thesis to my husband Wael Alfaqih and my children: Reemas, Abdulaziz and Raad who have supported me throughout my academic trajectory despite the self-alienation that came as a result of pursuing my goals. Their love, patience, and understanding allowed me to spend most of the time on this thesis.

Contents

List of Figures

List of Appendices Figures

List of Table

Abbreviation

AAV	Adeno associated virus
ADRP	Autosomal dominant Retinitis Pigmentosa
ARPE	Human retinal pigment epithelial cell
BiP	Binding immunoglobulin protein
CCD	Charge coupled device
Cdks	Cyclin dependent kinases
CLSM	Confocal laser scanning microscope
CNX	Calnexin
DAPI	4',6-diamidino-2-phenylindole
DIC	Differential interference contrast
DMEM	Dulbecco's modified Eagle's medium
EDEM	ER degradation-enhancing alpha-mannosidase-like protein 1
EDTA	Ethylenediaminetetraacetic acid
ER	Endoplasmic reticulum
ERAD	Endoplasmic reticulum associated degradation
ERC	Early receptor current
ERdj5	ER-resident disulfide reductase protein 5
FBS	Fetal bovine serum
FRAP	Fluorescence recovery after photobleaching
FRET	Fluorescence resonance energy transfer
GFP	Green fluorescence protein
GMK	Green monkey Kidney cells

GPCRs	G protein–coupled receptors
Grp78	78 kDa glucose-regulated protein
GUI	Graphical user interface
HEK	Human embryonic kidney cells
LRAT	Lecithin retinol acyltransferase
LED	Light emitting diod
NA	Numerical aperture
PC3	Prostatic carcinoma cell
ROS	Reactive oxygen species
RP	Retinitis pigmentosa
RPE	Retinal pigment epithelial
RPE65	Retinal pigment epithelium-specific 65 kDa protein
RPMI	Roswell park memorial institute medium
TM	Transmembrane domain
UGGT1	UDP-glucose:glycoprotein glucosyltransferase1
UVB	Ultraviolet B
WFM	Widefield fluorescence microscopy
VC	Violet correction

Thesis overview

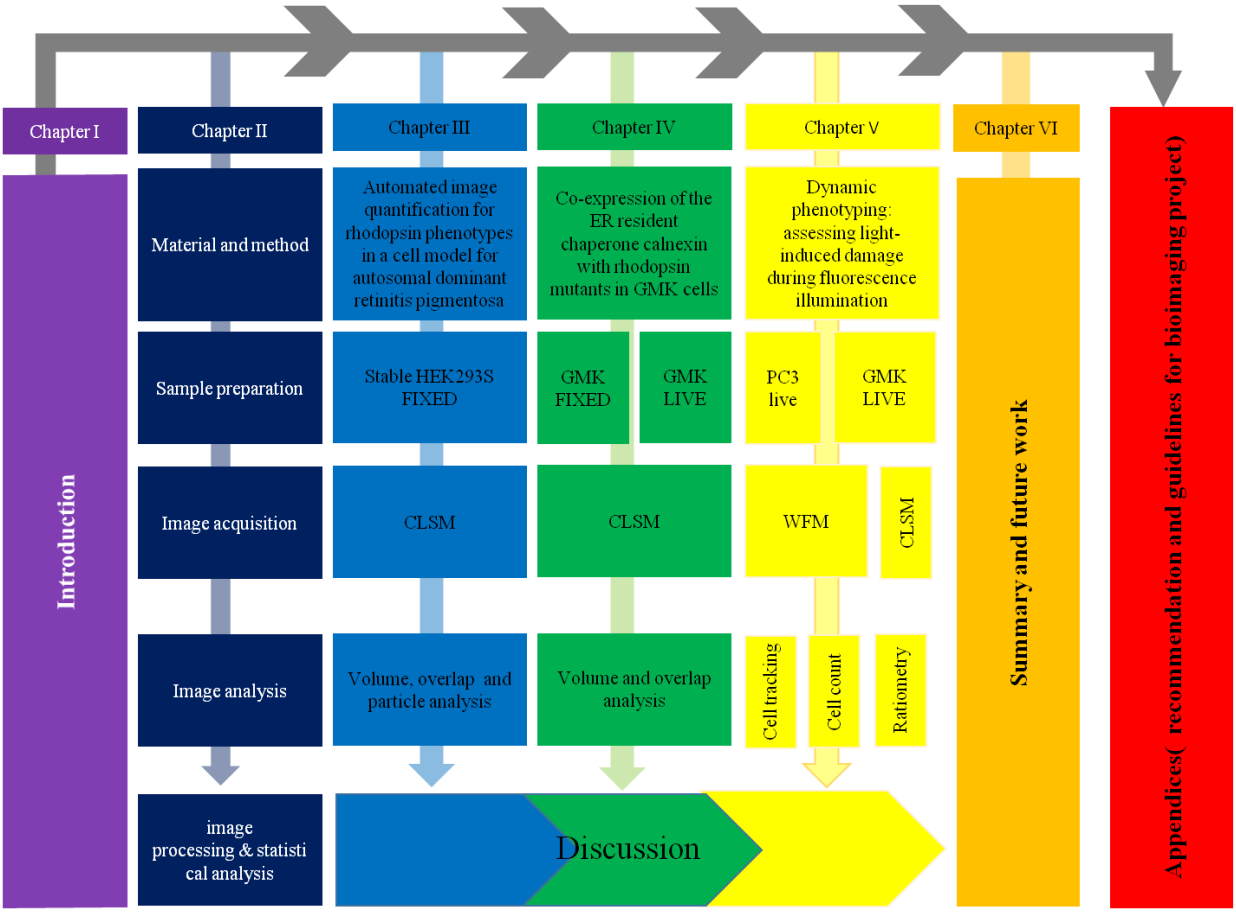

Project aims

The overall aims of this project was to use quantitative image analysis for the assessment and quantification of phenotypic changes in cellular homeostasis, dynamic and subcellular components within given cell lines through:

- In Chapter III: To utilise an automated quantification on a stably transfected HEK293S cell line expressing wild type and mutant rhodopsin in order to determine the distribution of rhodopsin phenotypic variations within and among the cellular models for autosomal dominant retinitis pigmentosa using 3D digital microscopy.
- In Chapter IV: To investigate the interaction, localisation and volumes of rhodopsin and calnexin in the GMK cell line co-transfected with rhodopsin-GFP phenotypes and calnexin-mCherry.
- In Chapter V: To assess damage induced by light at the cellular level by monitoring cell motility and mitotic delay in both GMK and PC3 cell lines. In addition, to investigate the increase in intracellular hydrogen peroxide as a product of ROS generation using HyPer biosensor.

Chapter I: Introduction

I.1 Overview of vision

I.1.1 The Human eye

The human eye is a highly efficient organ with the ability to refract light and produce a focused image (Figure I-1) that promotes a series of neural responses giving us the ability to see (Hogan *et al.*, 1971). Its strong integration into the neural circuitry, where it can occupy as much as 30 % of brain activity, exceptionally demonstrates its vital importance as the dominant sensory organ for the human being (Rao *et al.*, 2006). The human eye is made up of three layers, including three transparent structures. The outermost layer is composed of the cornea and sclera. The cornea is the transparent front part of the eye that covers the iris, pupil, and anterior chamber. The sclera also known as the white of the eye is an opaque, protective, outer layer of the eye containing collagen and elastic fibres. The median layer is divided into three structures: iris, ciliary body and the choroid. The iris is the coloured part of the eye, and it controls the light levels that pass to the eye. The ciliary body produces aqueous humour; this clear fluid fills the front of the eye. The final segment of the middle layer is the choroid, which this is the main source of blood in the eye. The innermost layer is the retina, which gets its circulation from the vessels of the choroid as well as retinal vessels (Atchison and Smith, 2000).

I.1.2 Cellular organisation of the retina

The retina is one of the most important parts of the eye because it is the light sensitive part. The retina (Figure I-2) is capable of creating images of the visual world by transforming light into an electrical and chemical signal that triggers nerve impulses, via the optic nerve to the visual centres of the brain (Kolb, 2003).

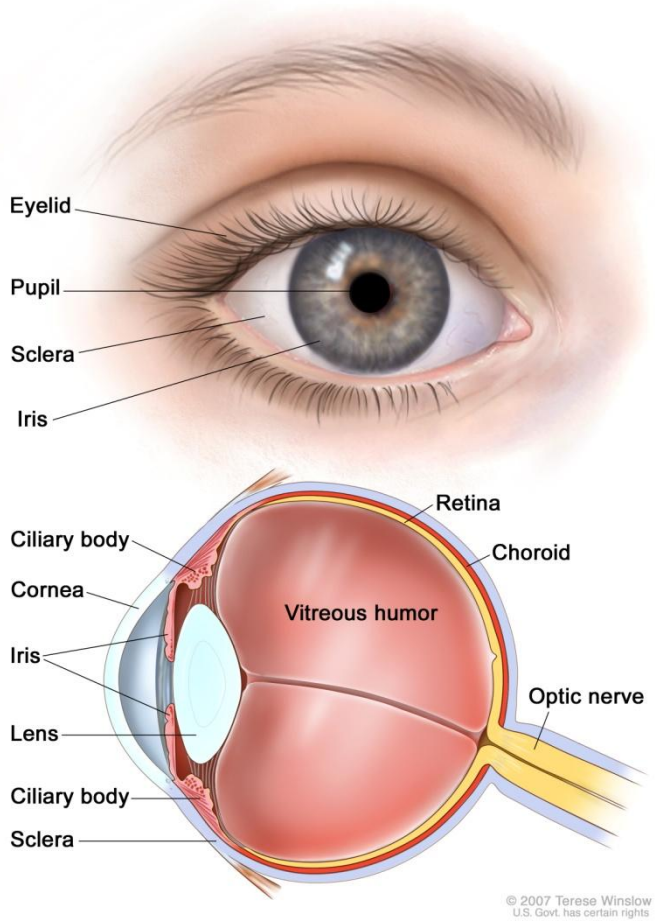

Figure I-1 Diagram of the human eye.

This diagram identifies the human eye's various segments. The dark circle in the centre is the pupil area surrounded by the structured iris diaphragm and the cornea. Image adapted from Winslow (2007).

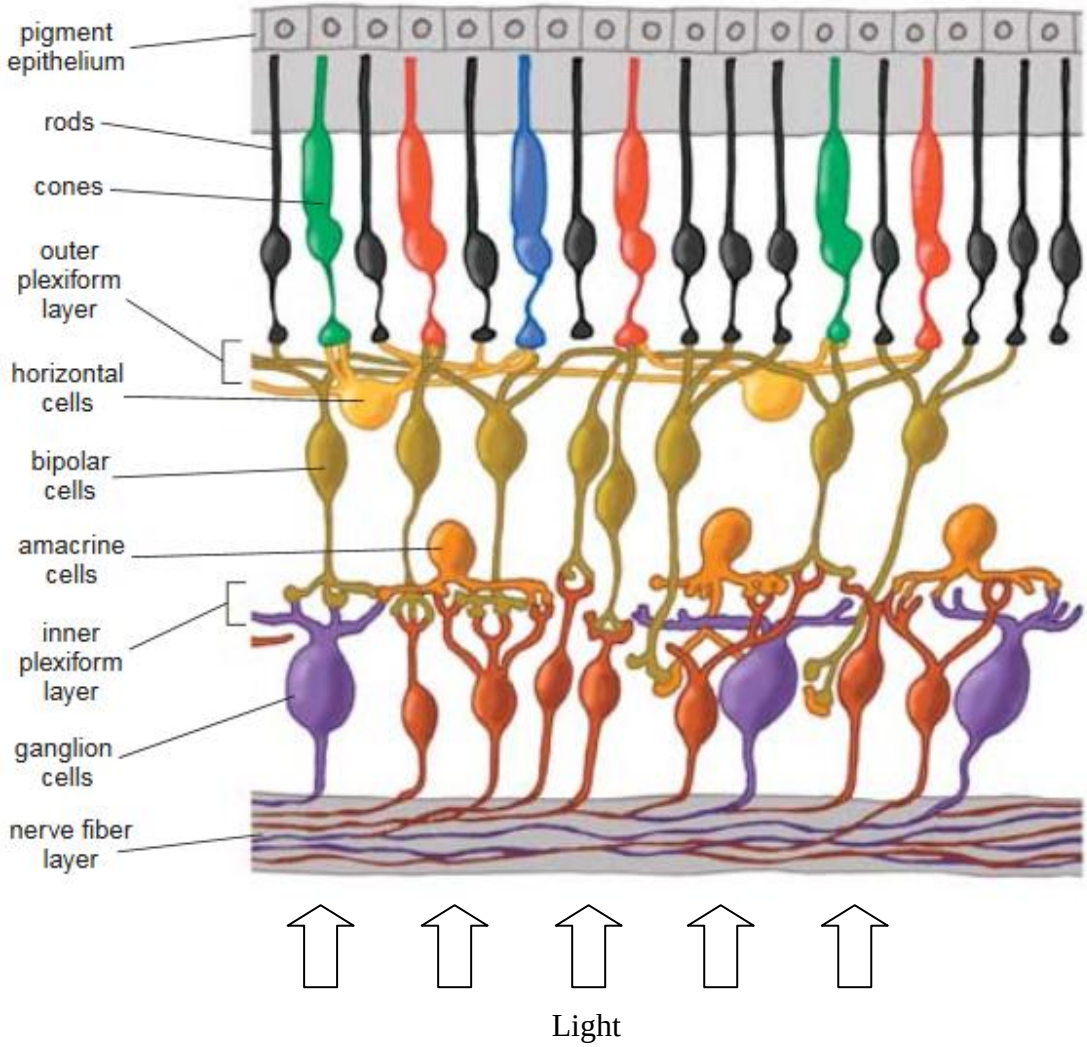

Figure I-2 Cross-section of the retinal layer.

The cross-section shows the types of retinal cells and how distinctly they are distributed in discrete layers. Photoreceptors (rods and cones) are at the top close to the pigment epithelium. Both amacrine cells and ganglion cells are near the surface of the retina. Image adapted from Kolb (2003).

The retina consists of three layers with packets of nerve cells arrayed in three rows and separated by two other layers containing synaptic connections. The photoreceptors are at the top of this set, close to the pigment epithelium. The bodies of horizontal cells and bipolar cells compose the inner nuclear layer. Amacrine cells lie close to ganglion cells near the surface of the retina. Axon-to-dendrite neural connections make up the plexiform layers separating rows of cell bodies (Kolb, 2003). In a simplified way, the retina can be considered as the brain outsourcing some of the image processing, so it can do its high-level interpretation – similar to the function of a good graphics card in modern computers.

I.1.3 Photoreceptors

Photoreceptors are photosensitive cells responsible for converting light into nerve signals then transmitting them to the brain through the optic nerve. Photoreceptors also send signals to other neurons by a change in their membrane potential when they absorb photons, in a process known as phototransduction. The human eye has two types of photoreceptor cells: rods and cones (Koenekoop, 2009). The rods number about 120 million, and are more sensitive to light than the cones. However, they are not sensitive to colour. The 6 to 7 million cones provide the eye's colour sensitivity (Hecht, 1987). Photopigment or coloured material fill the rods and cones and absorb particles of light that strike the retina and initiate the visual cycle (Koenekoop, 2009). In vertebrates, light cognizance is mediated by a group of G protein coupled receptors (GPCRs) called opsins. These opsins are bound to 11-cis-retinal, a chromophore (light-absorbing compound), derived from vitamin A (Johnson *et al.*, 2003).

I.1.4 G protein–coupled receptors

G protein–coupled receptors (GPCRs) are the largest family of cell surface proteins involved in biological membranes signalling (Filipek *et al.*, 2003). GPCRs are classically defined as the receptor, G-protein and downstream effector (Smrcka, 2008). For most GPCRs, the external signal is a small molecule that binds to the membrane-embedded receptor and causes it to undergo a conformational change. The conformational change on the intracellular surface of the receptor results in the binding and activation of several nucleotide-binding protein (G protein) molecules by a universal mechanism (Bhandawat *et al.*, 2005; Heck and Hofmann, 2001; Leskov *et al.*, 2000; Minke and Cook, 2002). Although GPCRs couple to G proteins, these receptors are also referred to as seven-transmembrane receptors, reflecting their seven membrane-embedded helices and additional signaling independent of G proteins (Lefkowitz, 2004; Pierce *et al.*, 2002). Rhodopsin belongs to the largest subfamily of GPCRs (family A) (Mirzadegan *et al.*, 2003). Vision starts with the absorption of photons, and the photon-triggered isomerization of the retinal from the 11-*cis* to the all-*trans* state, followed by conformational changes in the 7TM domain of rhodopsin to accommodate the binding of G proteins, leading to the downstream signal transduction (Chabre, 1985).

I.1.5 The visual cycle

Within the visual cycle, absorption of light converts 11-cis-retinal to all-trans-retinal (Figure I-3), and the conformational change initiates the visual transduction cascade. Once the chromophore has undergone photo-isomerisation, the visual pigment is said to be “bleached,” as shown in Figure I-4, and no longer able to absorb photons in the

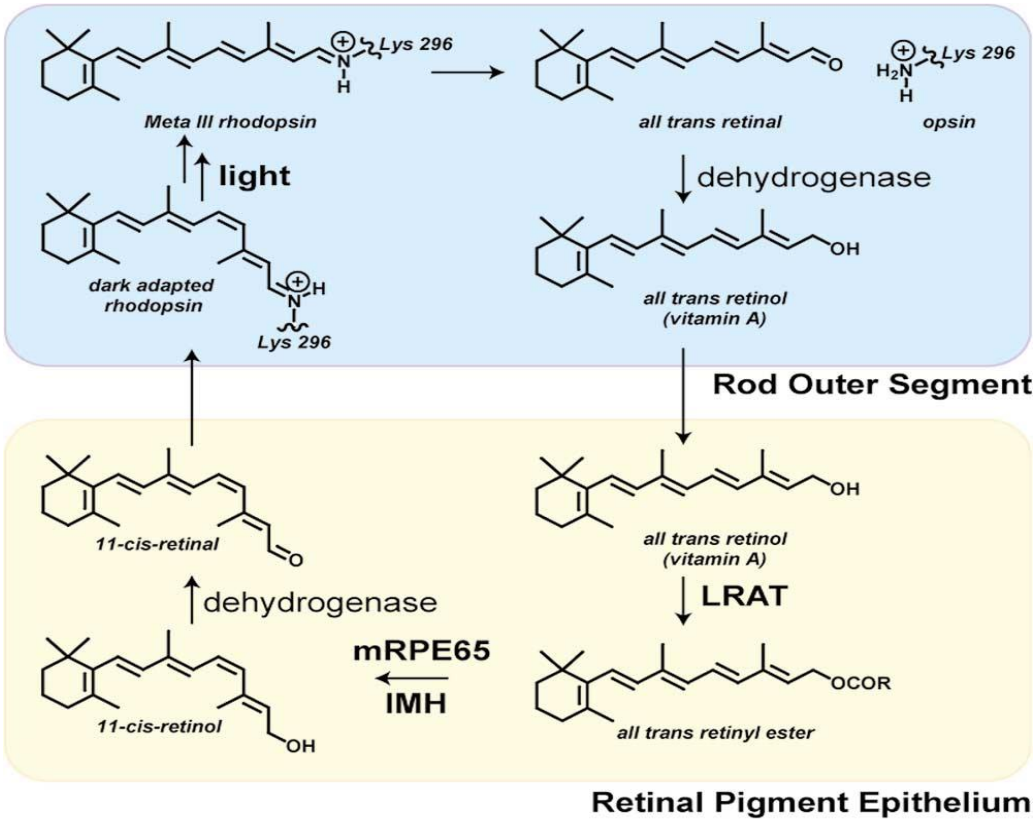

Figure I-3 Isomerisation of 11-cis-retinal to all-trans-retinal in the visual cycle.

In the rod outer segment, the chromophore 11-cis-retinal is covalently linked to opsin through it lysine amino acid residue by a Schiff–base bond and transformed to dark adapted rhodopsin, then to meta III rhodopsin after light exposure. All-trans-retinal reduces to all-trans-retinol. The all-trans-retinol enters the retinal pigment epithelium where it is esterified by lecithin retinol acyltransferase (LRAT). The all-trans retinyl ester is converted to 11-cis-retinol with the assistance of mRPE 65. 11-cis-retinol dehydrogenase converts to 11-cis-retinal. Image adapted from Xue *et al.* (2004).

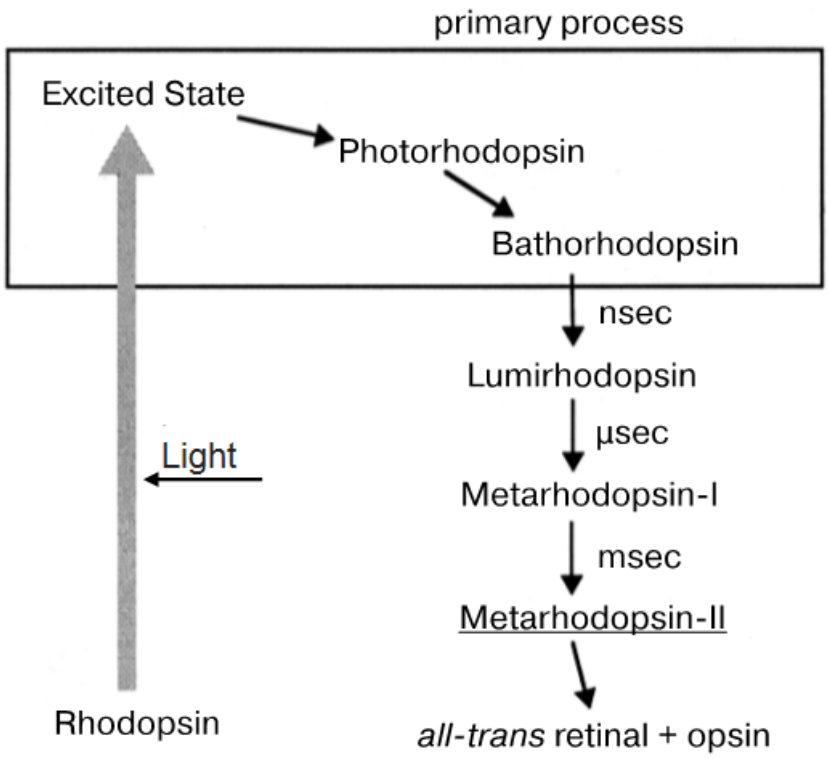

Figure I-4 Photobleaching process of bovine rhodopsin.

After photon absorption, by the chromophore 11-cis-retinal, fast isomerisation of the chromophore leads to the formation of a series of intermediate states of rhodopsin. Photorhodopsin, and bathorhodopsin in the primary process and finally metarhodopsin-II the active form of rhodopsin. Image adapted from Kandori *et al.* (2001).

"visual" region of the spectrum (Kandori *et al.*, 2001).The regeneration of the visual pigment to its previous dark state occurs by a series of biochemical reactions referred to as the visual cycle (Kolb, 2003). In the visual cycle activated opsin becomes reusable again in the visual scheme by the conversion of all-trans-retinal back to the 11-*cis* form, this visual cycle occurs mainly within the Retinal pigment epithelium (RPE). Within the RPE cells, the all-trans-retinol is bound to cellular retinol binding-protein and sent to lecithin retinol acyltransferase (LRAT) for esterification. The energy needed to isomerize the all-trans-retinol to 11- cis-retinol is generate by sub-sequent hydrolysis of the ester bond by isomerohydrolase RPE65 (Redmond *et al.*, 1998). Finally, it is oxidized to 11-cis-retinal before traveling back to the rod outer segment where it can again be conjugated to an opsin to form a new, functional visual pigment (rhodopsin). Mutation to any of the genes that code any protein or enzyme associated with the visual cycle or the phototransduction cascade can lead to different types of retinal degenerations (Phelan and Bok, 2000).

I.2 Rhodopsin

Rhodopsin is the visual pigment protein in the vertebrates rod cell found in the retina, and is responsible for vision under dim light conditions (Hargrave, 2001). Nathans and Hogness (1984) isolated and sequenced the gene encoding human rhodopsin. It is a member of the G-protein coupled receptors (GPCRs) consisting of an opsin 348 amino acids, and a chromophore. The N-terminus of rhodopsin is located at the extracellular rod cell membrane, whereas the C-terminus is in the intracellular part.

This protein spans the membrane bilayer seven times, resulting in a seven-transmembrane-*helix* receptor (Sakmar and Huber, 2009). In 1986, Dixon and his colleagues first determined the primary sequence of a member of the rhodopsin

superfamily, the β-adrenergic receptor. Figure I-5, shows a model of the secondary structure of bovine rhodopsin. 50 % of rhodopsin amino-acid residues are highly conserved between the rhodopsin family members in all GPCRs atom (Terakita, 2005). Each rhodopsin binds to a chromophore:11-cis-retinal (Figure I-6a). The crystal structure of bovine rhodopsin is illustrated in Figure I-6b. The Lys296-residue also known as K296 is the chromophore attachment site (Figure I-6c), where it binds retinal through a Schiff-base linkage, by the formation of a double bond between the nitrogen atom of the K296 amino group with the retinal carbon atom (Terakita, 2005). The K296 residue is important for light absorption and it can be used to determine whether or not a newly found rhodopsin-type GPCR is really an opsin (Li *et al.*, 1996). Instructions for making rhodopsin are coded on the RHO gene. Its cytogenetic location is on the long (q) arm of chromosome 3, between positions 21 and 24 (Genetics, 2012). There is a strong link between mutations on the rhodopsin gene and a group of hereditary retinal degenerative diseases collectively known as Retinitis Pigmentosa (RP) (Kisselev, 2005).

I.2.1 Retinitis Pigmentosa

The medical term *Retinitis Pigmentosa* (RP) was first used by Donders in 1857 to describe the pattern of pigmentation seen in the peripheral retina of a proportion of blind patients (McKie *et al.*, 2001). It is a genetic disorder that is characterised by photoreceptor cell death and gradual loss of vision (Phelan and Bok, 2000; Rattner *et al.*, 1999). This disease is distinguished, by retinal pigment deposits visible on fundus examination as shown in Figure I-7 (Openshaw *et al.*, 2008). RP is estimated to affect one in 3000–5000 individuals worldwide (Kisselev, 2005).

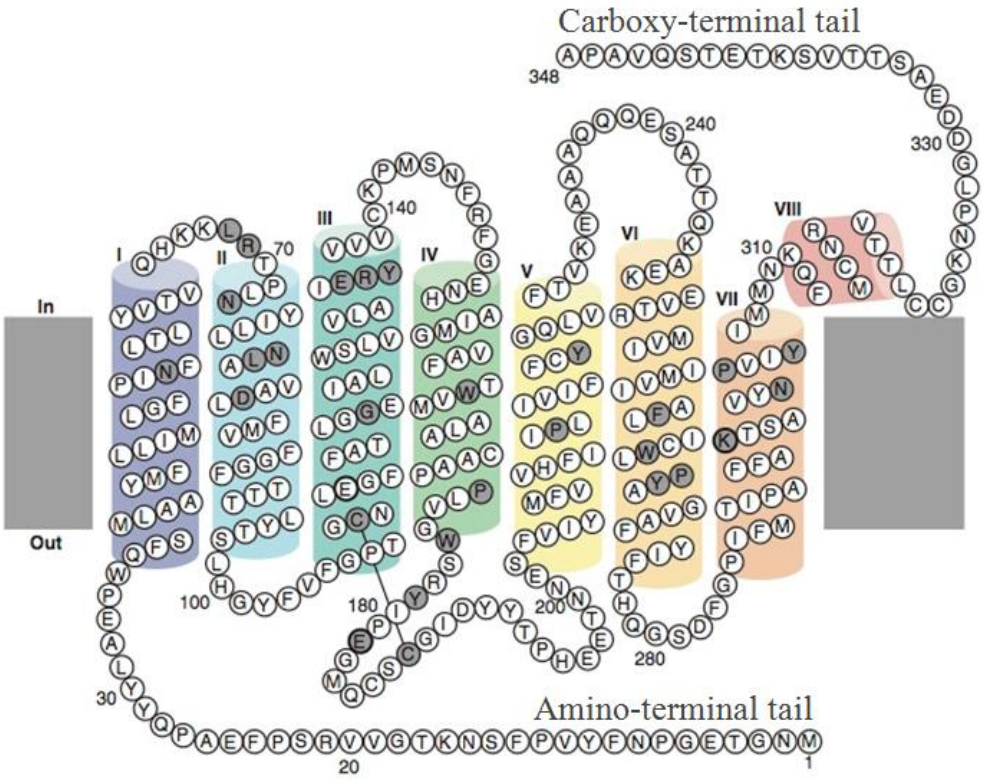

Figure I-5 Secondary structure of bovine rhodopsin.

A secondary structure diagram of bovine rhodopsin. The amino-acid residues that are highly conserved in the whole opsin family are shown with a gray background. The retinal-binding site (K296) is marked with bold circles. Amino acid residues are depicted in single-letter code. The amino-terminal tail and extracellular domain is toward the bottom, and the carboxy-terminal tail and cytoplasmic domain is toward the top. Image adapted from Terakita (2005).

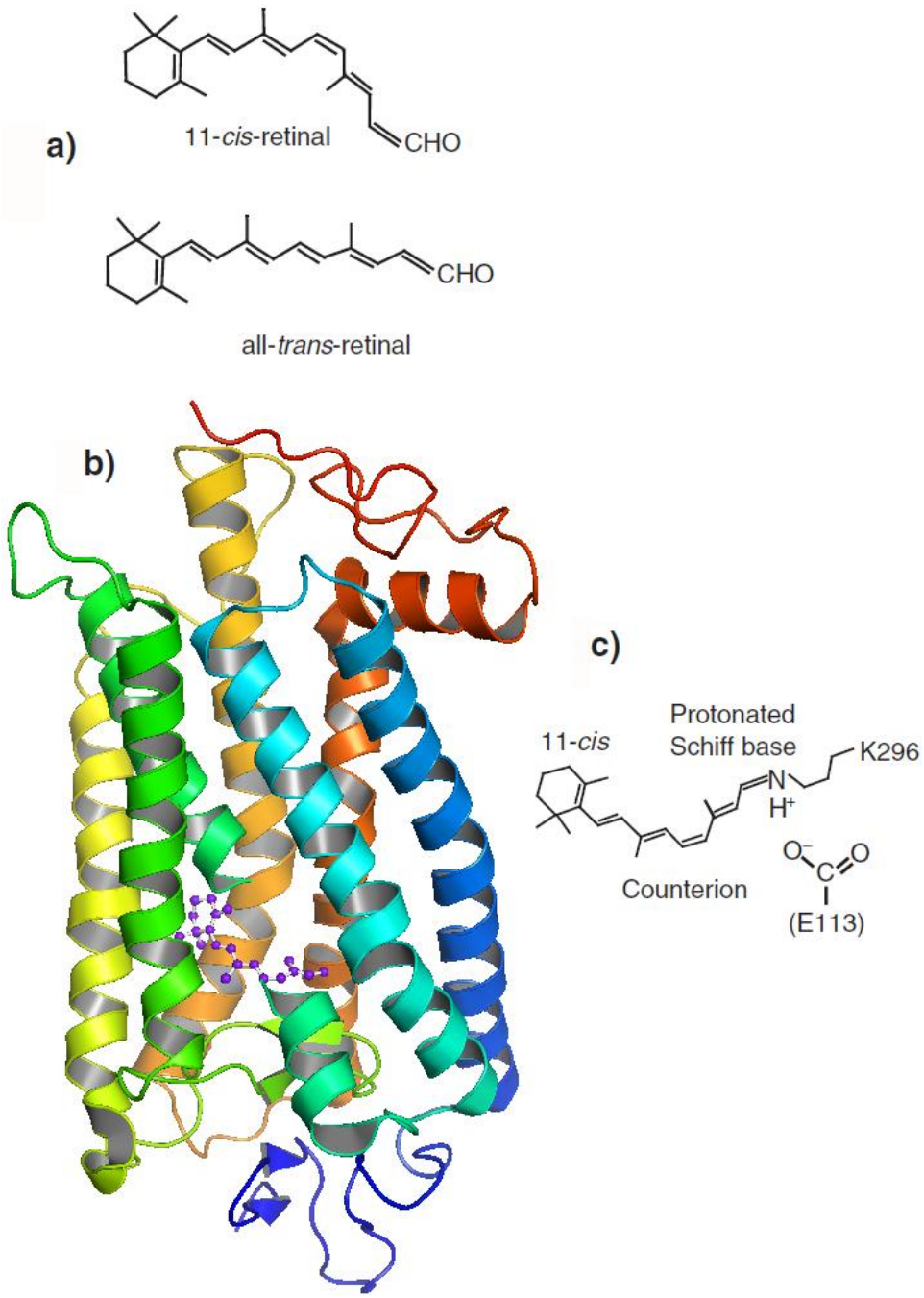

Figure I-6 Retinal structures and the crystal structure of bovine rhodopsin.

a) 11-cis and all-trans retinal chemical structures. b) Crystal structures of bovine rhodopsin done by PyMOL, PDB-entry: 1u19 (Palczewski *et al.*, 2000), the ringed area representing chromophore 11-cis-retinal, K296. c) Shows the structure of the Schiff base linkage formed by retinal within opsin.

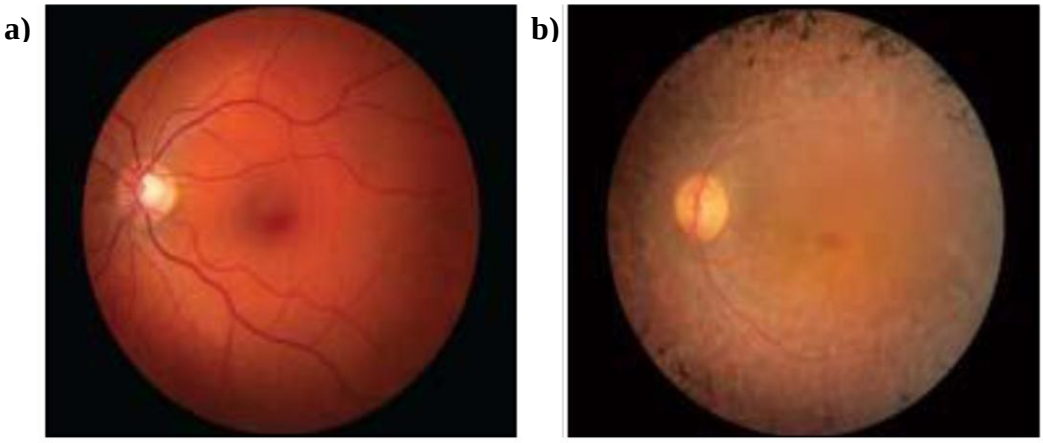

Figure I-7 Fundus photography for healthy eye and eye affected with RP.

a) Photography for a normal eye. b) Photography for the eye of a patient diagnosed with RP. The RP fundus shows spicule-shaped bone and clearly visible retinal pigment. Image adapted from Openshaw *et al.* (2008)

The inheritance patterns of RP can be through: autosomal-recessive (about 50-60% of cases), autosomal-dominant (about 30-40%), or X-linked (5-15%) (Hartong *et al.*, 2006). Amongst rhodopsin mutations over 150 mutations have been identified as being linked to autosomal dominant retinitis pigmentosa (ADRP) (Garriga and Manyosa, 2002); all are listed on the Retinal Information Network online (RetNet, 2012). These reported mutations appear to be responsible for modifications in all rhodopsin domains: extracellular, membrane-embedded, and at cytoplasmic level.

I.2.2 Classification of rhodopsin mutations in ADRP

Mutant opsins have been classified according to their expression and biochemical properties into: two (Sung *et al.*, 1991b) or three classifications (Kaushal and Khorana, 1994; Krebs *et al.*, 2010). According to the Sung *et al.* (1991b) classification, class I mutants exhibited no defect in trafficking; they could transfer to the cytoplasmic membrane and bind 11-*cis*-retinaldehyde to form active rhodopsin. Meanwhile, class II mutants varied in severity according to their biochemical defects. In class IIa mutations, rhodopsin failed to exit the endoplasmic reticulum (ER) or to reconstitute with 11-cis-retinal, while in class IIb mutants the proton accumulated in both the ER and plasma membrane. All class I mutants were in the C-terminal region, whilst almost all the class IIa mutants were in the extracellular region of the N-terminus domain, and all the class IIb mutants were in the transmembrane domains, (Sung *et al.*, 1993). Kaushal and Khorana (1994) classification focussed on the different phenotypes at rhodopsin intradiscal domain. The type I phenotype resembled the wild type, showing a correct folding and successful binding of 1l-*cis* retinal with the chromophore. Type II mutants were misfolded and retained in the ER and failed to

bind 11-cisretinal. Type III mutants were also misfolded and showed a differing ability of the chromophore to binds with 1l-cisretinal (Kaushal and Khorana, 1994; Krebs *et al.*, 2010) .

I.2.3 Rhodopsin point mutations at position 23 in the N- terminus region

P23H Rho is a short term for a single base-substitution mutation of codon 23 of the rhodopsin gene in which proline is changed to histidine (Pro23His) resulting in the misfolding of rhodopsin (Berson *et al.*, 1991), among more than 80 different Rho mutations associated with ADRP (Gal *et al.*, 1997), this point mutation was the first to be identified (Dryja *et al.*, 1990). P23H is classified as a class III mutations and it is the most frequently reported mutation in ADRP cases, it is accounts for approximately 12% of North American ADRP patients (Berson *et al.*, 1991; Krebs *et al.*, 2010). P23H misfolded rhodopsin partially reconstitutes with 11-*cis* retinal, does not proceed to the Golgi apparatus, is retained in the ER leading to ER stress, and activates the unfolded protein response (UPR) (Kaushal and Khorana, 1994; Sung *et al.*, 1991a). Proline-23 by leucine (P23L) or by alanine (P23A) substitutions are also associated with ADRP (Oh *et al.*, 2000; Sung *et al.*, 1993).

I.2.4 Cellular trafficking and quality control of mutant rhodopsin

Rhodopsin is a secretory protein synthesised in the rough ER. Upon synthesis, rhodopsin translocates into the ER for the folding processes. Properly folded proteins are transported to the Golgi apparatus, and subsequently to the outer segment which is believed to be the site for rhodopsin-mediated phototransduction (Tsai *et al.*, 2002).

Maintaining cellular protein homeostasis is critical for a cell's viability; the presence of mutant proteins will increase the demand for protein quality control (Hebert and Molinari, 2007). P23H mutant rhodopsin, is a highly hydrophobic polytopic membrane protein that is unable to fold in the endoplasmic reticulum (Rajan *et al.*, 2001). UDP-glucose:glycoprotein glucosyltransferase1 (UGGT1) is the quality control sensor of the ER, which recognizes the formation of misfolded proteins, and alters their glycosylation stage (Kroeger *et al.,* 2012). Glycoprotein modification is effected on the nascent polypeptide by the attachment of Glc3Man9GlcNAc2-core glycan to its chain. This monoglycosylated N-glycan becomes a substrate for ER-resident lectins, calreticulin and calnexin. Calnexin bind to the *N*-linked oligosaccharides of P23H mutant rhodopsin, ensuring protein folding by stabilizing folding sequences, preventing aggregation of unfolded proteins, and facilitating disulfide-bond formation (Oliver *et al.*, 1999). This cycle continues until the native conformation of the protein is achieved. When mutant rhodopsin fails to pass ER quality control, it will be targeted for disposal by endoplasmic reticulum-associated degradation (ERAD). ER degradation is enhanced by the ∝-mannosidase-like protein EDEM1, by the extracting of misfolded glycoproteins from the calnexin cycle (Kroeger et al., 2012). EDEM1 was initially described as a type II membrane protein located in the ER membrane by its uncleaved signal sequence, which was suggested to be necessary for the formation of a functional complex with calnexin (Oda *et al.*, 2003). EDEM's proteins are major targets of the ER-stress- induced Ire1/Xbp1 pathway (Hirao *et al.*, 2006; Olivari *et al.*, 2005; Yoshida *et al.*, 2003). This pathway enhances the mammalian cell's capacity for ER-associated degradation (ERAD) in response to the elevation of the misfolded polypeptides (Hebert and Molinari, 2007). In 2009, Kosmaoglou et al., reported a dual role for EDEM1 in the processing of

rhodopsin in the ERAD, as EDEM1 recognises mutant rhodopsin in the ER lumen and targets it for ERAD (Kosmaoglou *et al.*, 2009). Moreover, ERdj5 is the mammalian protein disulfide isomerase and a cochaperone of EDEM1. ERdj5 recognizes misfolded proteins and reduces disulfide bonds by reductase activity, which is important to facilitate protein dislocation from the ER to the cytoplasm (Ushioda *et al.*, 2008).

Figure I-8, shows a model of P23H rhodopsin clearance in photoreceptors by ERAD mechanism (Kroeger *et al.*, 2012). In transfected cells, mutant rhodopsin fails to translocate to the plasma membrane and accumulates within the ER and Golgi. These mutant proteins remain within the cell and fail to form the visual pigment with 11-cis-retinal. These mutations result in an incompetent protein that cannot translocate to the plasma membrane or to the outer segment in photoreceptors (Saliba *et al.*, 2002). Furthermore, Saliba and co-workers reported that P23H mutant rhodopsin does not accumulate in the Golgi; instead, it forms aggregates that have many of the characteristic features of an aggresome leading to the dispersal of the Golgi apparatus. The degradation of mutant opsin is dependent on the proteasome machinery. Proteasome inhibition does not lead to an increase in aggresome formation but increases the retention of the protein within the ER. In 2002, Illing and colleagues studied P23H rhodopsin aggregates and their interaction with the ubiquitin proteasome system. They found out that P23H rhodopsin aggregates in transfected cells and forms high molecular weight oligomeric particles in the cytoplasmic area. Fluorescence resonance energy transfer (FRET) experiments confirmed that P23H aggregates in the cytoplasm even at low expression levels (Illing *et al.*, 2002).

Their results confirmed the role of the P23H mutation in destabilising rhodopsin and causing its degradation by the ubiquitin proteasome system.

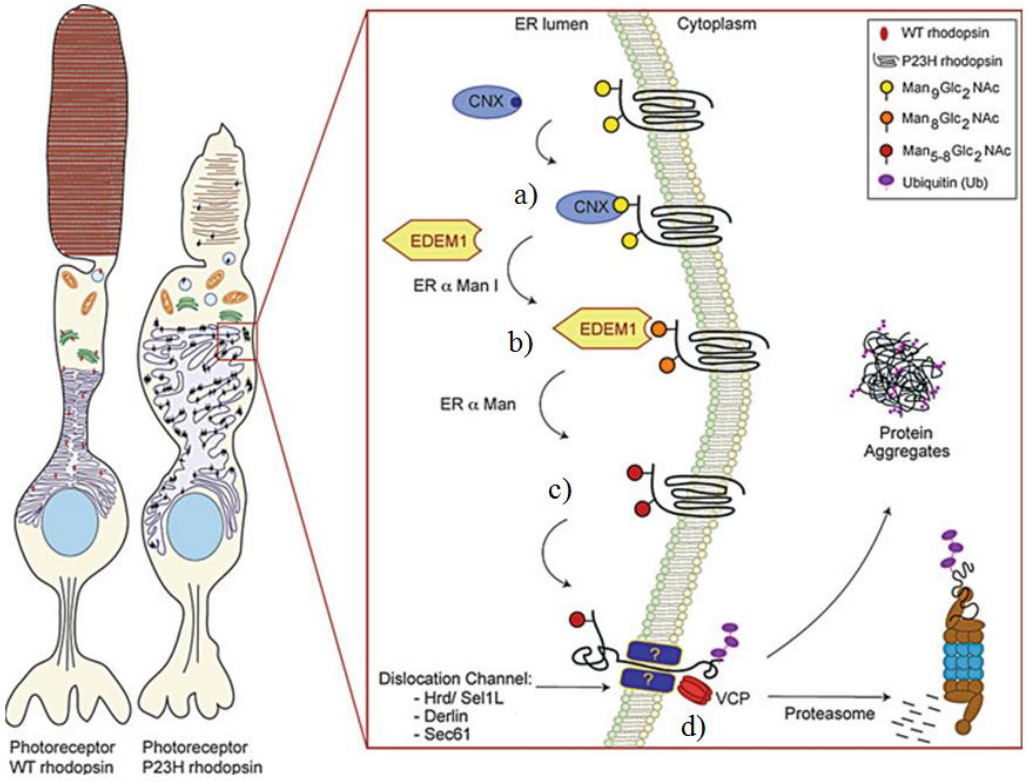

Figure I-8 Model of P23H rhodopsin ERAD.

a) Misfolded P23H rhodopsin interaction with calnexin (CNX). b) P23H Rho is trapped in the quality control, then recognized by EDEM1. c) Demannosylation of P23H Rho by EDEM1. d) P23H extracted into the cytosol for degradation by the proteasome or, to form aggregates. Image adapted from (Illing *et al.*, 2002; Kroeger *et al.* (2012)).

They furthermore demonstrated the increased tendency of transfected HEK cells to self-associate into high molecular weight aggregates, as a robust gain of function, with a direct link to pathogenesis caused by a class II ADRP mutant rhodopsin. It is essential to discriminate between aggregates, which are non- native protein oligomers, and inclusion bodies, which are distinct cellular regions that aggregated proteins trapped inside. Whenever a protein is partly or incorrectly folded, aggregation for this protein is necessary in order to avoid cellular stress (Hebert and Molinari, 2007). Protein aggregates tend to be insoluble and metabolically stable under physiological conditions. There is a strong link between this accumulation and neuronal degeneration diseases (Kopito, 2000). In 1999, Tran and Miller conclude that cytoplasmic inclusion bodies are strong pathognomonic indictors for cellular degeneration in most neurodegenerative diseases. The oligomeric forms of rhodopsin aggregates are non-native structures (Downer and Cone, 1985), whereas wild-type is monomeric (Kopito, 2000). Rajan et al. (2001) suggested that, if protein aggregation is independent of inclusion body formation, then the distribution of coexpressed proteins in nocodazole dispersed foci should reveal the extent of protein coaggregation. Nocodazole is a drug that disrupts or alters microtubule structure and causes fragmentation and dispersion of Golgi throughout the cytoplasm (Rogalski *et al.*, 1984). Rajan et al. (2001) test this prediction by coexpressing P23H-YFP and CFP-ΔF508 in HEK293 cells and further treated the cells with nocodazole in the presence of N-acetyl-Leu- Leu-norleucinal. They found that P23H dispersed foci were nearly always distinct from foci of ΔF508. That confirmed that P23H protein and ΔF508 do not coaggregate with one another. In 1999 García-Mata et al., published a paper in which they described the characterisation and dynamics of aggresome formation of misfolded protein within specialized cells. Their results

suggest that pathology in cells containing aggregated proteins is due to functional unavailability in this defected protein, rather than aggresome inhibition of the vital cellular functions (García-Mata et al., 1999).

I.2.5 Animal model of ADRP

Several of transgenic animal models were used to study and investigate the development of retinal degeneration arising from the P23H mutation. Olsson *et al.* (1992) extracted genomic DNA from clinical patients and constructed multiple transgenic mouse lines expressing either the wild-type or the P23H allele of the human rhodopsin gene. These mutant transgenes were expressed on the wild-type genetic backgrounds of the endogenous mouse rhodopsin gene. Rod photoreceptors were shown to be extremely sensitive to a slight rhodopsin over-expression, which leads to retinal degeneration.

Machida *et al.* (2000) studied the correlation between retinal functional changes and structural changes in P23H rhodopsin transgenic rats. Their animal model showed accelerated degeneration in rod outer segment and cell loss in the outer nuclear layer with age, findings which were consistent with clinical findings amongst P23H patients. Recovery after bleaching and the normal phototransduction sensitivity in this rat model are different from that experienced in human P23H disease. Moreover, severity of retinal degeneration in this model made it inadequate to be an experimentally useful model of ADRP.

Other studies by Gorbatyuk *et al.* (2012) and Gorbatyuk *et al.* (2010) involves the attempt to rescue the visual function of retinal in P23H ADRP animal models by gene delivery of BiP/Grp78. They used an Adeno-associated virus (AAV) to overexpress

the BiP protein in P23H rhodopsin photoreceptors. A significant improvement in electroretinogram amplitudes and survival of photoreceptors in treated eyes were reported. However, this rescue was not associated with increases in the level of properly reconstituted rhodopsin but rather with suppression of the unfolded protein response.

Sakami *et al.* (2014) used P23H opsin knock-in mice in order to highlight the novel step in retinal rod disc morphogenesis. They recorded the transretinal electroretinogram for the mice retina and found that P23H mutant Rho can trigger phototransduction but the rods of P23H opsin homozygous mice are ~17000-fold less sensitive to light than wild type mice's rods and produce abnormally fast photo-responses. Their research findings add more insights into P23H mutant opsin's effect on ADRP development.

I.2.6 HEK293 cell line as a study model for ADRP

Human Embryonic Kidney 293 cells, also often referred to as HEK293, are a specific cell line originally derived from human embryonic kidney cells grown in tissue culture (Graham et al., 1977). HEK cell line has been used as an expression tool for recombinant proteins since it was first produced over 25 years ago. HEK cell biochemical machinery is capable of carrying out most of the posttranslational folding and processing required raising functional, mature protein from both mammalian and non-mammalian nucleic acids. The use of this cell line is becoming increasingly preferable as a transient expression system, as well as having been used in stably transfected forms experiments. Moreover, the HEK cell line is quick and easy to

reproduce and maintain, with high performance in transfection and efficient protein production (Thomas and Smart, 2005).

In order to understand the pathogenesis of rhodopsin mutants involved in ADRP, Sung et al expressed heterologous wild-type rhodopsin and ADRP-linked rhodopsin mutants in HEK293 cells (Sung *et al.*, 1993; Sung *et al.*, 1991b). They tracked the fate of rhodopsin mutants using immunofluorescence and Western blotting techniques. They reported that a large number of rhodopsin mutants involved in ADRP possessed a defect in trafficking to the plasma membrane, and were retained in the ER (Sung *et al.*, 1993; Sung *et al.*, 1991b).

Moreover, in 2003, Noorwez et al., used vitamin A therapy on HEK293 cell line. They reported that, 11-*cis*-7-ring retinal may be a useful therapeutic agent for the rescue of P23H-opsin and the prevention of retinal degeneration. Furthermore, they describe a pharmacological chaperone, 11-*cis*-7-ring retinal, which attained success *in vivo* to quantitatively enhance the folding of P23H-opsin. As rescued opsin forms pigment, it acquires mature glycosylation, and is transported to the cell surface.

In 2002, Brueggemann and Sullivan used HEK-293S expressing opsins to measure rhodopsin activation by the early receptor current (ERC), a conformation-associated charge motion. They bleached the cells and then loaded them with 11-cis-retinal. Interestingly they recorded a recovery in the ERC signals within minutes and recurrently over a period of hours by simple dark adaptation, this having been achieved without adding chromophore to the cells. Their result supports the usefulness of HEK cells as a model because their findings are evidence for the presence of intrinsic retinoid processing machinery in wild- type HEK293S cells similar to what take place in the mammalian eye.

In their study, Illing et al. (2002) concluded that, when expressed in HEK293, class II mutant rhodopsins in contrast to wild type are unable to fold correctly within the endoplasmic reticulum, fail to acquire complex oligosaccharides indicative of transit through the Golgi apparatus and are severely defective or unable to produce functional photopigment on reconstitution with 11-cis-retinal. Also class II mutants fail to accumulate to high levels in transfected cells, implying that they are subject to enhanced intracellular degradation.

Moreover, Reeves et al., (2002) developed a tetracycline-inducible system for constructing stable HEK293S cell lines, cells which give high-level expression of wild type opsin and mutants only in response to the addition of tetracycline. This stable cell line provides consistent cellular expression of opsin protein and is highly reliable for studying the mechanisms of human cell death in ADRP that caused by rhodopsin mutations.

The tetracycline-inducible cell lines were also used by Opefi *et al.* (2013). They expressed rhodopsin mutations in the N-terminal cap in order to rescue misfolded rhodopsin by both 11-cis-retinal pharmacological chaperone and disulfide bond-mediation. They concluded that N-terminal cap has multiple roles in rhodopsin folding, stability and signal transduction.

I.3 The importance of visual assessment in research and the early development of microscopy

Advancement in biology was always coupled with the scientists' visual assessment of an object of interest. In the past, understanding the nature of life was limited to what the human eyes could see, beyond that there was room for any number of assumptions and experiments. It is fair to say that all science and ideas about the nature of life

started with the Ancient Greeks. They believed in the existence of a simpler world that behold the everyday world we experience. The Greeks established many theories to explain each phenomenon they encountered, yet there was very little advancement in understanding the true nature of organisms until the late 18th century (Hall, 1969).

The evolution of the cell theory is a living example for how the development of visual assessment tools can reshape the face of knowledge. The Introduction of the microscope facilitated the study of cells and open the door for a new visible world to be discovered. In 1665, Robert Hooke, an English microscopist, described cells. He used a microscope to examine and describe chambers in cork and first called them cells (Wolpert, 1995). The significance of Hooke's discovery was not valued until after the first description of living single cells by Anton van Leeuwenhoek in 1670. Despite all these early investigations, the development of cell theory remained delayed due to the inadequacy of microscopes together with techniques for preparing the tissues. The great breakthrough in cell theory was coined by both Schleiden (1838) and Schwann (1839); all organisms are composed of one or more cells and the cell is the structural unit of life for all organisms. Approximately 20 years later, Virchow put the finishing touch to cell theory when he determined that cells only ever come from other pre-existing cells (Wolpert, 1995).

I.4 Digital microscopy: the eyes of modern cell biology

Since the invention of the first multi-lens microscopes about 400 years ago, microscopy has experienced a peak in the past 40 years, accompanied by the revolution in molecular biology, chemistry, materials science and electronics (Dunn *et al.*, 2011). In particular, the development of fluorescence microscopy has allowed a breakthrough in the study of fixed or living cells. Interpretation of the signal emitted

by excited biological fluorophores, such as fluorescent antibodies or proteins, facilitates the understanding of cell structure, function and dynamics. Furthermore, the development of digital technology and of computational tools for image analysis enables scientists to exploit micrographs to their full potential (Kherlopian *et al.*, 2008).

I.4.1 Image acquisition

The relationship between the photons coming from the sample, and the electronic signal they produce in a digital photodetector, is linear (Fink *et al.*, 1998; Stuurman and Swedlow, 2012). With the advent of new optics, filters, illumination sources, sensitive digital cameras, fluorescence microscopy has taken a big leap forward – especially since computers now allow for reproducible image processing. With a rapidly increasing demand for image quantification, literature on the subject has grown exponentially (Fink *et al.*, 1998; Stuurman and Swedlow, 2012).

I.4.1.1 Advantages of fluorescence microscopy

Contrast is an important factor that enables the human eyes to comprehend the details of objects in micrographs. Various innovative methods to enhance the distinctness of microscopy images have been designed. By far the most popular technique now is fluorescence microscopy (Dobrucki, 2013). Fluorescence microscopy requires the use of fluorophores, which absorb light in a specific wavelength range, and emit it at a longer wavelength. Currently, a very large number of different fluorophores and dyes with absorption from the UV to the near-infrared region are available. The industry of fluorescently labelled antibodies and probes facilitates an enormous number of

biological applications of fluorescence microscopy. Those antibodies, probes and dyes are known for their specificity, high contrast, sensitivity and selectivity (Combs, 2010). Development of fluorescent proteins ignited a revolution in microscopy and contributed to the development of new microscopic techniques and enabled the recent enormous growth of cell biology. Osamu Shimomura, a Japanese scientist, and two American scientists, Martin Chalfie and Robert Y. Tsien, were awarded a Nobel Prize for Chemistry in 2008 for the discovery and development of green fluorescent protein (GFP) in biological research (Kauffman and Adloff, 2009). Multiple information about structure and the spatial distribution of a molecule of interest is preserved in a fluorescence microscopic image. It facilitates our ability to quantitatively study the structure and function of intact cells in fixed or live biological systems (Dobrucki, 2013). Comparing the subcellular distributions of two fluorescently labelled molecules is one of the most common routines in fluorescence microscopy. This comparison helps us to understand the function of the protein of interest, when this protein colocalises with a tag or a marker of a particular organelle. An understanding of a protein's intracellular transport system can be gained also when the protein of interest is found to colocalise with a marker on a particular pathway (Dunn *et al.*, 2011; Obara *et al.*, 2013).

I.4.1.2 Biophysical principles of fluorescence

The emission of a fluorescence signal is a beautiful manifestation of a fluorophore's excitation by some light source. This photophysical phenomenon was first illustrated in the form of a diagram in 1930 by Aleksander Jabłoński (Lakowicz, 1999). Jabłoński's diagram features the energy levels within a molecule where valence

electrons could be excited as shown in Figure I-9. When a fluorescent molecule absorbs a photon of the appropriate wavelength, an electron is excited to a higher energy state and almost immediately falls back to its initial ground state. S0 is the ground state and represents the energy of a molecule that is not being excited by light. S_1 and S_2 are excited singlet states in which an outer electron is boosted into a different orbital. S_2 contains more energy than S_1 and S_1 more energy than the ground state, S_0. The triplet states is where an outer electron, boosted to a new orbital, has also undergone a subsequent reversal in spin so former pair of electrons is now parallel. In the process of energy collapse the molecule can release the absorbed energy as a fluorescent photon. Since some energy is lost in the process, the emitted fluorescent photon typically exhibits a lower frequency of vibration and a longer wavelength than the excitatory photon that was absorbed (Cranfill *et al.*, 2016; Lichtman and Conchello, 2005).

I.4.1.3 Different image acquisition techniques

Modern biological image acquisition techniques allow cell biologists to comprehend various cellular topography, to visualise the substructures of cells and to monitor a molecule's dynamics. With many microscopic systems available from various manufacturers they have become very easy to operate. Widefiled and confocal microscopy are some of the most widely used biological imaging systems which can be found in any bioimaging facility worldwide (Combs, 2010).

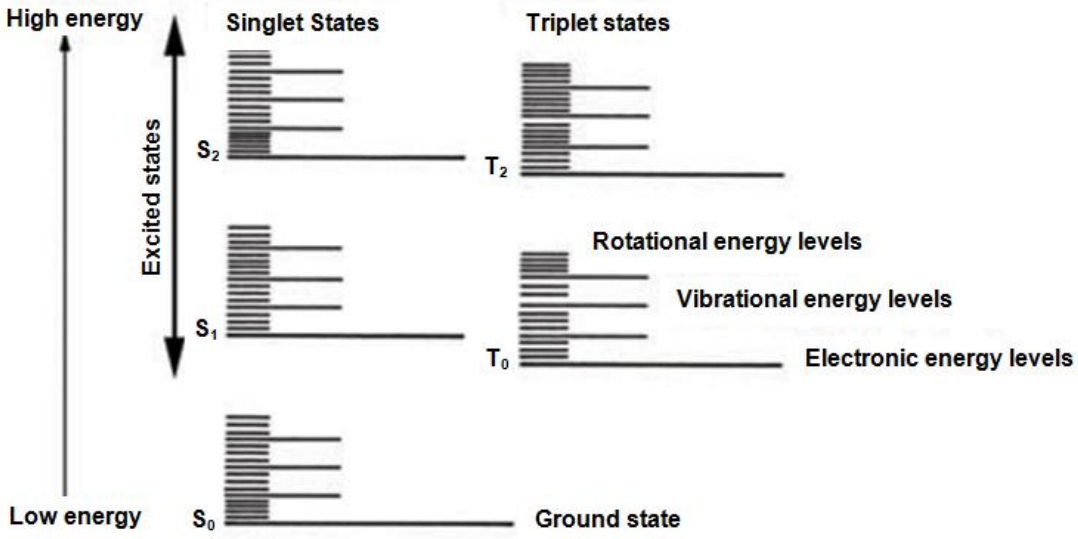

Figure I-9 Jabłoński's diagram displaying the basic principle of fluorescence.

Image adapted from Lichtman and Conchello (2005).

I.4.1.3.1 Widefield fluorescence microscopy

In the basic form of widefield fluorescence microscopy (WFM), the source of light is usually xenon or mercury lamp, giving out pure white light. Optical excitation and emission filters are then used in order to select the required wavelength of light that passes through the objective to the sample of interest. This involves exciting the fluorophore(s) in the sample of interest. The resulting light emitted, of longer wavelength, is detected through the microscope eyepieces or by a camera followed by computer digitization (Coling and Kachar, 2001). The main advantages of WFM are that it is the least expensive technique, and it delivers good XY dimension resolution (Combs, 2010). Fluorescence deconvolution microscopes homogeneously illuminate the whole specimen and grab the entire image simultaneously on a charge-coupled device (CCD) camera. In the case of WFM 3D imaging, the 3D stacks are processed using iterative algorithms that assign out of focus signal back to the fluorescent object it came from in the correct focal plane. In this way, deconvolution can yield high-resolution WFM 3D information from images (Gerlich and Ellenberg, 2003).

I.4.1.3.2 Confocal Microscopy

The confocal microscope, also known as the confocal laser scanning microscope (CLSM) remains a significant piece of equipment in most imaging laboratories. Most modern CLSM systems offer a variety of advantages and are equipped with software to execute complex 3D (z-stack) and 4D (z-stack over time) imaging. CLSM often includes software to facilitate data acquisition such as spectral deconvolution, fluorescence recovery after photobleaching (FRAP), and fluorescence resonance energy transfer (FRET) (Pawley, 1995). In contrast to WFM, CLSM excites the

fluorophore by moving a focused laser beam line by line over the specimen and then recording each image pixel sequentially on a point detector, the photomultiplier tube. All out of focus light will be rejected before it reaches the detector and confocal stacks thus yielding 3D images with high axial resolution (Gerlich and Ellenberg, 2003).

I.4.2 Image quantification

Quantification provides an important new dimension to the scientific process, as expressed in the famous quote by Lord Kelvin: " In physical science a first essential step in the direction of learning any subject is to find principles of numerical reckoning and methods for practicably measuring some quality connected with it, when you can measure what you are speaking about, and express it in numbers, you know something about it; but when you cannot express it in numbers, your knowledge is of a meagre and unsatisfactory kind ” (von Bartheld and Wouters, 2015).

Technical advances in cell biology typically happen first at the qualitative level, followed after various delays by the exploration into and development of quantitative methods for comparing differing results (von Bartheld and Wouters, 2015). Image quantification is a term which stand for quantifying substances within cells (Chieco et al., 2013). Qualitative imaging can only deliver snapshots of events and states without providing the tools for interpretation. Quantification is key to bringing the necessary objectivity to the understanding of rules and causal associations between apparent events (von Bartheld and Wouters, 2015).

Turning qualitative data into quantitative values has become one of the fundamental approaches in today’s imaging technologies. It opens the way toward a sophisticated

view of cell biology on the quantitative level and is an integral facet of biomedicine (Chansawang *et al.*, 2016; Eils and Athale, 2003). Formerly, acquisition of two dimensions (2D) images was the common approach when studying the interaction between two proteins of interest in fixed or live cell (Gordon *et al.*, 2007). However, protein quantification should be captured in three dimensional (3D) images. Moreover, complex dynamic processes are ideally studied in three spatial dimensions over time (4D) images (Eils and Athale, 2003; Gerlich and Ellenberg, 2003). Retrieval of quantitative data from microscopic images has become easy but the main challenges is whether the quantitative data are true reflections of the microscopic objects being analysed (Chieco et al., 2013). The quantification of fluorescently labeled molecules in subcellular compartments is an important step in the analysis of many biological processes in cells. In order to achieve successful image quantification, various points need to be taken into account (Chieco et al., 2013; Rizk et al., 2014). According to Obara et al. (2013), it is important to use optimally stained samples for reliable image acquisition and quantification. Furthermore, images should be acquired with the correct parameters for each experiment, and saturated pixels in the acquired images should be avoided. Also all images should be acquired following Nyquist–Shannon's reconstruction theorem, which states that the smallest structure in an image, as determined by the microscope's resolution, should be represented by at least two pixels (Nyquist, 1928; Shannon, 1949).

The abundance, heterogeneity, dimensionality, and complexity of the data produced in modern imaging experiments dismiss manual image management, processing, and analysis. Therefore, computerized techniques for the execution of these tasks have become of fundamental importance for any further progress in cell biology (Meijering, 2012). The first examples of the automated processing of two-dimensional

(2D) images was in the 1960s, with the purpose of differential counting of leukocytes based on simple colorimetric and morphological measurements (Preston, 1976). In the mid-1970s, commercial systems for performing routine clinical tests hit the market. They contained several computer circuits to synchronise the tasks of examining the image of the previous cell, while obtaining the image of the present cell, and at the same time locating the next cell in the specimen (Meijering, 2010). In the 1980s, the advent of confocal microscope systems opened the door to three-dimensional (3D) cell image analysis. But it was not until the 1990s, when computers systems became powerful enough to deal adequately with complex 2D and 3D data (Gurcan *et al.*, 2009). Automation allows for the processing of large volumes of information, making possible analyses like those conducted in high content screening (Zhou and Wong, 2006). Additionally, the bias of the visual analysis is prevented, since the applied criterion is always the same. Automatic image analysis is faster than any manual method of analysis. However, automation in microscopy image analysis is not absolute, because it depends on the variability of the automated settings in producing images (Diaz Zamboni *et al.*, 2015).

An essential step in image analysis, which is prior to quantification, is image segmentation. Specifically, because cellular morphology is an important phenotypic characteristic indicative of the physiological state of a cell, and since the cell count is frequently required for subsequent analysis of intracellular processes. The field of cell segmentation has received increasing attention in past years (Bengtsson et al., 2004). Image analysis usually includes a segmentation step to differentiate between areas of interest such as intensity and the background, with the underlying assumption is that cells have significantly different intensities than the background (Adler and Parmryd, 2014). Image segmentation methods deliver an initial approximation of the structure

of interest based on it morphological features such as size, shape, colour, etc., facilitating the discrimination of smaller areas visually imperceptible, and later quantifying of the object of interest (Hernández-Morera et al., 2016). Cell analysis via automated image segmentation is mostly a difficult problem due to the large variability such as; different microscopes, stains, cell types, cell densities and data complicity (Meijering, 2012). The first and the most fundamental approach to cell segmentation is intensity thresholding (Adler and Parmryd, 2014). The second is segmenting the image based on feature detection, which is an intensity derived feature that can be easily detected using linear image filtering (Meijering, 2012).

Intensity thresholding consists of labelling a pixel as foreground if it is above a threshold value, and as background if it is below. The threshold value may be the same for all pixels, or it may be a function T(x, y) of the pixel location, called a threshold surface. Several thresholds maybe used to obtain multi-labeled segmentation. For robustness, thresholds can be computed using image features, e.g. using global statistics (histogram-based threshold) or local statistics (space-based threshold) (Sezgin, 2004). Otsu's method is a histogram-based threshold methods popular in quantifying substances within cells, it consists in maximising the scatter between the background and foreground pixels (Noboyuki, 1979).

I.5 Computational phenotype quantification in mammalian cells

Phenotype analysis is a rising approach in biomedical research, encouraged by our rapidly growing knowledge about the human genome (Neumann *et al.*, 2010). High-throughput phenotyping analysis of single-cell quantification can reveal information concealed in population averages (Gordon *et al.*, 2007). Moreover, conducting a large scale screening of cellular phenotypes, at whole-cell or sub-cellular levels, is

important for resolving gene functions, for the outlining of cellular pathways, for drug discovery and even cancer diagnosis (Peng, 2008).

The term "phenotype" was first introduced by the Danish botanist Wilhelm Johannsen in 1909. Although the concepts of heredity were expressed by Mendel decades earlier, the distinction between "gene", "genotype" and "phenotype" are well described by Wilhelm Johannsen. The distinction is between the hereditary placements of organisms (their genotypes) and the ways in which those placements manifest themselves in the physical characteristics of those organisms their phenotypes (Peirson, 2013). However, phenotypes mirror genetic influences other than the intended genetic manipulations, as well as experiential and environmental influences including infectious agents. Potential impacts of extra-experimental variables must be considered when interpreting phenotype data (Brayton, 2011).

Cellular phenotypes, such as cell morphology, the intensity or subcellular spatial distribution of labelled protein markers, are important biological properties of individual cells. (Laksameethanasan *et al.*, 2013). Cellular structures often have amorphous shapes, differ from cell to cell and undergo dynamic changes, all factors that make quantitative structural measurements extremely difficult or impossible (Gerlich and Ellenberg, 2003). Subcellular distribution is an important feature of a protein because location is well related to the protein function. Fluorescently tagging the protein of interest is the most common method used to identify a protein's subcellular location by visually analysing the microscopic images of this protein (Hu *et al.*, 2010). A previous report had shown that automatic image analysis can outperform visual examination, providing higher sensitivity to subtle differences (Murphy *et al.*, 2003), although protein subcellular localization is the most important determinant of a protein's task within the cell. However, this important protein

attribute is often described in a qualitative way, therefore its applications in quantitative protein analyses are limited (Loo *et al.*, 2014).

Precise cell image quantification remains a real challenge in biology since cells seeded on a conventional petri dish adopt different shapes and hence intracellular architectures (Waters, 2009). Proteins from major subcellular locations can be differentiated from each other with over 90% precision (Huang and Murphy, 2004). In order to achieve successful phenotypic quantification, high-throughput automated recognition of protein subcellular distributions is required along with robust image features (Huang and Murphy, 2004).

Automated digital fluorescence microscopes provides us with the chance to collect the large numbers of fluorescent images for various proteins that are required in order to quantify cellular phenotype (Hu *et al.*, 2010). Methods for comparing protein and nucleotide sequences (and structures) are well established and can be used directly from database entries, although comparing protein locations from database entries is not yet possible (Murphy *et al.*, 2002). Murphy *et al.* (2002) reported that protein subcellular locations can be determined automatically using fluorescence microscope images based on numeric descriptors. Furthermore, Murphy and his group improved the reliability in classifying 2D images. They applied a features less sensitive 2D images to the image spatial and intensity resolution then they added new skeleton features (Murphy *et al.*, 2002).

Confocal 3D fluorescence imaging provides opportunities to further improve the accuracy of automated phenotype classification and quantification. More information is contained in 3D images than in 2D versions. As a result, location arrangements that may be difficult or impossible to distinguish in 2D images may possibly be identified based on the information encoded in the additional dimension (Murphy, 2010).

Finally, in most cases, time series images had better reflect protein behaviour in living cells. They provide comprehensible biologically important data since many proteins change their location over time in order to carry out their functions (Hu *et al.*, 2010).

I.6 When seeing is not believing: Artefacts in bioimaging

I.6.1 User bias in visual image interpretation

The simplicity with which humans can see things in images is very deceptive, pure visual analysis of fluorescently labelled microscopic images is very prone to subjective bias, since the judgment of an observer can be easily influenced by the presence of background information, or apparent absence of other image artefacts which can't be detected due to the limitation of the human vision (Diaz Zamboni et al., 2015). Human vision has a built-in directional bias that favours the vertical, followed by the horizontal, and a strong preference for symmetry (Russ, 2004). As shown in Figure I-10a, that can bias the observer's judgment. It also influences our the ability to detect gradients or clustering. Detecting gradients is often important in image analysis via visual assessment, however, they are not always easy to spot with human eyes. The structure of the human eye is much more sensitive toward different colours than toward different shades of grey. This shortcoming will add more user bias during visual image interpretation which should be taken into consideration (Haidekker, 2011). The problem is that there can be so many different kinds of gradient. Moreover, features may differ in size, orientation, shape, colour, density, number, or any arrangement of these factors. Figure I-10b shows only a few of the

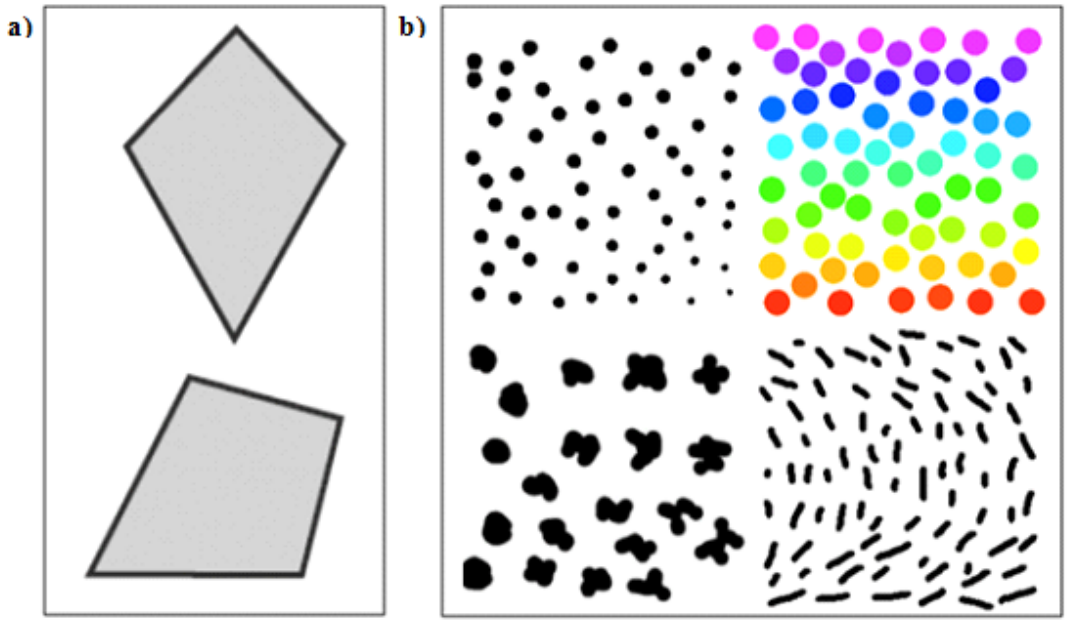

Figure I-10 Example of human vision built-in directional and gradients bias.

a) The two shapes are not perceived to be identical. The “kite shape” on the left has dominant vertical axis of symmetry. The irregular four-sided polygon on the left has a horizontal base. b) Examples of different gradients size, colour, shape, and orientation. Images adapted from Russ (2004).

possibilities. The gradient may be linear, although not necessarily horizontal or vertical, but it can also be radial. In many cases, when the features have sizes and contrast that should be visible, the presence of variations in the background intensity (or colour) can prevent the visual system from detecting them.

In Figure I-11, the text has a local contrast of about 4% but is superimposed on a ramp that varies from white to black. Application of an image processing operation reveals the message. The "Unsharp Mask" routine subtracts a blurred (smoothed) copy of the image from the original, suppressing large scale variations in order to show local details (Russ, 2004). The need to find order in images is a human habit, but this inherent ability is risky. Sometimes we imagine a symmetry or order that is not there, and sometimes the presence of complexity hides the real underlying structure. Complicated gradients are likely to escape recognition unless we know previously what to look for. The result is that many real spatial arrangements may be overlooked, in two dimensions and with an even worse outcome when analysing three-dimensional spatial arrangements because all cellular and intracellular processes occur in three-dimensions (Russ, 2004). Interpretation of the information concealed within a microphage is a critical task which requires a well-trained observer (Gerlich and Ellenberg, 2003). An important aspect of bioimaging is being able to identify what you are viewing under the microscope and to distinguish the fact from the artefact (Chandler and Roberson, 2009).

I.6.2 Light-induced cell damage: The limits of live imaging

Light-induced damage to biological samples during time-lapse fluorescence imaging is known to occur but receives too little attention by researchers.The main limitations of live fluorescence techniques arise from the instability of the fluorescent dyes as

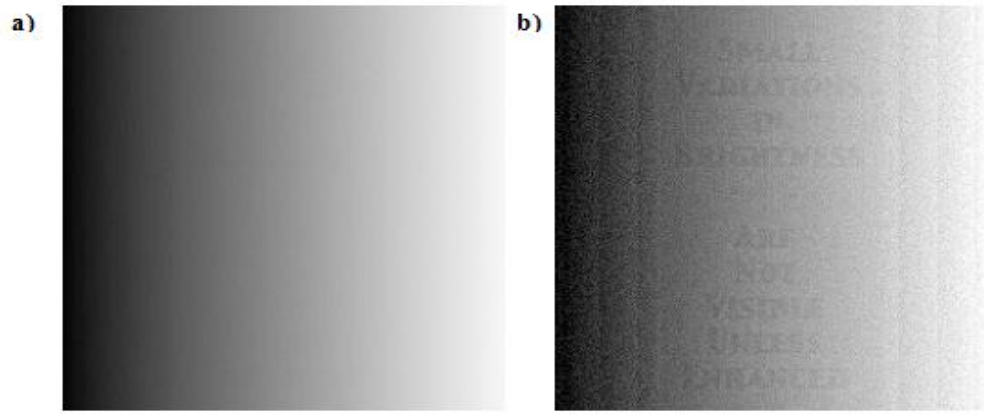

Figure I-11 Intensity differences superimposed on a varying background are visually undetectable.

a) Original image. b) The original image after processing with an “Unsharp Mask” filter to suppress the gradual changes and reveal the detail (text). Images adapted from Russ and Woods (1995).

they may photobleach. Photobleaching occurs as the result of accumulated chemical damage to fluorescent molecules from the excited electrons. This can limit the time over which a sample can be detected by fluorescence microscopy (Combs, 2010). Fluorophore photobleaching may lead to the production of phototoxic substances that will greatly compromise the investigated cellular system in the case of real-time bioimaging (Bernas *et al.*, 2004).

CLSM is far from an optimal tool for *in vivo* imaging not only do the incoming and outgoing cones of excitation create premature bleaching and damage outside the focal plane, at the focal plane itself an actinic spot of light is created that leaves destruction in its wake as it sweeps through the specimen (Cranfill *et al.*, 2016). Despite the disproportionate effects of accelerated photobleaching on laser-scanning approaches, confocal imaging is superior for many studies of intact tissue because of its 3D signal discrimination, and many long-term confocal imaging studies have been successful with fluorescence proteins. The damaging effect of confocal will always strongly depend on sample, plants for example are able to take it and exhibit normal behaviour, at least in short-term experiments, despite the high intensity of CLSM (Exposito-Rodriguez *et al.*, 2013).

It is important to indicate that photobleaching is specific to fluorescence microscopy and is a consequence of the loss of fluorescent signal that occurs when fluorophores are excited into a state leading to an irreversible loss of signal (Diaspro *et al.*, 2006). Phototoxicity, on the other hand, is a correlated phenomenon in as much as it may be provoked by photobleaching of fluorophores, but not necessarily, as it may also occur in the absence of fluorophores (Tinevez *et al.*, 2012).

I.6.2.1 Phototoxicity in *in vivo* light microscopy

A comprehensive understanding of cellular dynamics is difficult to get hold of from only analysing the images acquired from fixed cells (Frigault *et al.*, 2009). New microscopes and image-processing software are now making it possible to rapidly record two or three-dimensional images over time. This time-lapse imaging allows explicit quantitative analysis and has become a key tool for understanding the complex organization of biological discipline in live samples (Gerlich and Ellenberg, 2001). live imaging microscopy provides us with the ability to revisit individual cells over time, to collect light emissions over a long times and to acquire cell images with high resolution (Gordon *et al.*, 2007). These techniques are known to be harmful to live specimens and hence to jeopardise the reliability of the obtained information and to lead to deceptive conclusions. A plethora of studies has been reported on the effects of light on biological tissues, which correlate with varying illumination settings (Debarre *et al.*, 2014; McDonald *et al.*, 2012; Roehlecke *et al.*, 2009).

The key requirements for an ideal imaging data set are interdependent. Sample health, images contrast (signal-to-noise ratio), temporal and spatial resolution. This can be illustrated as the diamond of frustration (Figure I-12). The frustration terms come from the impossibility to optimize all of these factors at the same time; improving one will compromise another. Apart from sample health, improving one technical side of imaging will negatively affect others. For example, improving spatial resolution will decrease photon counts per pixel.

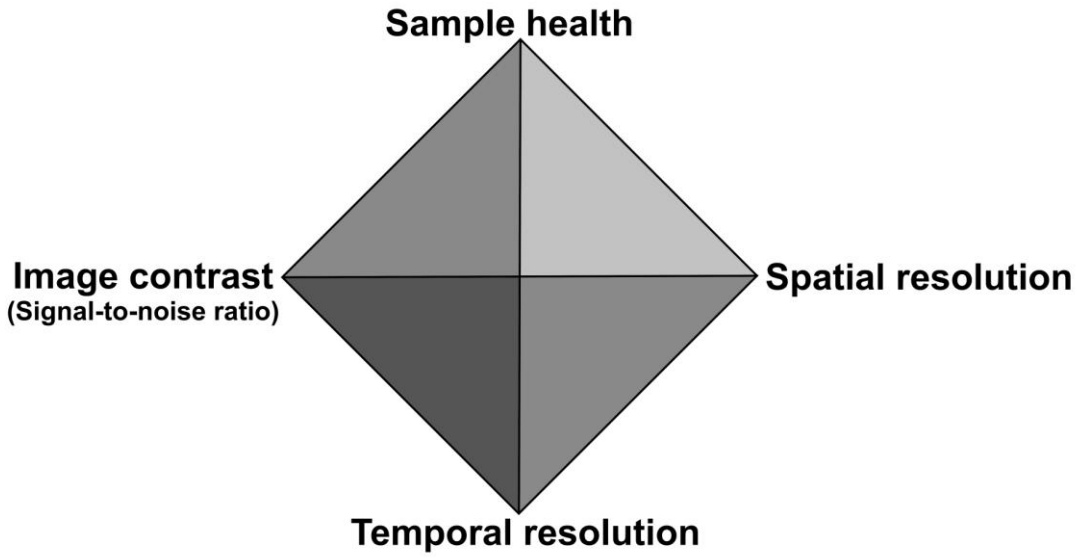

Figure I-12 Diamond of frustration.

The four requirements for the ideal imaging data set (sample health, images contrast, temporal and spatial resolution). All these factors are co-dependent, resulting in tradeoffs between them.

I.6.1 Phototoxicity: causes and effects

Most tissues and cells are never exposed to light, in their normal life cycle. However, exposing living samples to light is a common routine in fluorescence-based imaging (Tinevez *et al.*, 2012). Fluorescence-based imaging is typically visualised by using WFM or CLSM with cellular production of H_2O_2 in cultured mouse,

monkey, and human cells (Hockberger *et al.*, 1999). This photooxidative damage occurs through the well-known phenomenon of light-induced reactive oxygen species (ROS) production (Bartosz, 1997; Frigault *et al.*, 2009; Wright *et al.*, 2002). ROS is a term which simply refers to chemically reactive molecules that are derived from oxygen and can be free radicals such as: superoxide O2•−) or hydroxyl radical OH•, or non-radicals such as hydrogen peroxide H_2O_2 (Bolisetty and Jaimes, 2013).

The role of ROS in phototoxicity has been demonstrated in animal and plant cells (Dobrucki, 2001). ROS production may be manifested in physiological changes by directly damage to key cellular molecules such as proteins, lipids, and nucleic acids, and/or by triggering changes through the disturbance of the redox homeostasis (Dixit and Cyr, 2003). Light emitting diode (LED) illumination can be used as a substitute for illumination in fluorescence microscopy as it supplies the right excitation wavelength for each fluorophore (Tinevez *et al.*, 2012). Moreover, Nishigaki *et al.* (2006) reported that an LED-based pulsed illumination system has advantages over conventional illumination systems for fluorescence imaging of live cells.

I.6.1.1 Cumulative insults

A considerable amount of literature has been published on addressing the effect of light irradiation on live cell culture. In their previous study, both De Vos *et al.* (2009)

and Hoebe *et al.* (2008) measure photobleaching as the time-dependent decay of fluorescent intensity coming from a known amount of fluorophore. They extrapolate their conclusions to be relevant to grasping the consequence of phototoxicity in live biological systems. However, in 2012, Tinevez and his co-worker reported that while phototoxicity and photobleaching processes may, in many instances, be tightly coupled, they are nonetheless definitely separate phenomena.

In their experiments, Zdolsek *et al.* (1990) counted the percentage of dead cells appearing over a few days after illumination by a mercury lamp in an epifluorescence microscope. They reported that the cellular death is linked to the oxidative damage resulting in destabilization of the lysosomal membrane.

Moreover, König *et al.* (1999) measured cellular response to near-infrared laser pulses in multiphoton microscopes. Moreover, Tinevez *et al.* (2012) reported that the analysis of dead or dying cells as a measure of phototoxicity, discounts the fact that phototoxicity may cause much more subtle effects that started way before that endpoint.

Saetzler *et al.* (1997) reported that a high incident light dose can provoke uncontrolled leukocyte activation and adhesion in venules and arterioles, which is a critical point when studying inflammatory response. The number of activated leukocytes was calculated for a given period of time and analysed as a function of the incident light dose. Furthermore, in neuron calcium imaging, it was observed that the dynamic range of Ca^{2+} pulses was damaged by a strong illumination power (Koester *et al.*, 1999; Saetzler *et al.*, 1997).

A more sophisticated approach to quantify phototoxicity was taken by Dixit and Cyr (2003) and Dixit *et al.* (2006). They found thresholds of 0.79 J/cm^2 and 1.866 J/cm^2, depending on wavelength, in wild type tobacco cells expressing GFP. Interestingly,

no mitotic arrest was observed below the threshold. They proposed a concrete guidelines for noninvasive imaging using WFM. Their guidelines are based on studies of mitosis in plant cells subjected to varying illumination conditions; however, their general applicability to different organisms is not known.

In most cases, higher light intensity leads to more severe photodamage in mammalian, however type of microscope, illumination mode, wavelength, the cell type, cycle and age all greatly affect the effect of illumination on a live sample. Knight *et al.* (2003) reported an increase in the levels of Ca^{2+} and cell death for chondrocytes caused by cellular imaging based on CLSM. Furthermore, Manders *et al.* (2003) found that the cell-cycle progression of HeLa cells was affected by the same imaging technique. Visible light can cause epithelial cell dysfunction through the action of ROS on the mitochondrial DNA, this may contribute to tumorigenesis and cellular age-related pathologies (Godley *et al.*, 2005). Dobrucki *et al.* (2007) studied fluorescence recovery after photobleaching. They reported that light scattered by illuminated cells can induce phototoxic effects on neighbouring cells that are not illuminated.

Another study on the ARPE cells confirmed that ultraviolet B (UVB) radiation (280–315nm), induced a decreased phagocytotic activity of the ARPE cells when the energy level of UVB radiation is from 0.2 to 0.4 J/cm^2 (Youn *et al.*, 2010). In addition, (Wagner *et al.*, 2010) calculated the number of cells able to form a colony after irradiation by epifluorescence microscope. All the latter studies, regard cell rounding, nuclear fragmentation, and/or cell blebbing as an indicator of cell death. However, the incident light dose was not reported.

McDonald *et al.* (2012) measured calcium transients as very sensitive indicators of stress in single smooth muscle cells. They reported that intracellular Ca^{2+} can be

increased globally in smooth muscle cells by using blue light (LED with 488 nm peak emission).

Ultimately, live fluorescence microscopy "will always be a tradeoff" (E. Betzig, personal communication with P. Laissue). No microscopy modality is immune to causing phototoxicity, so there is no single perfect technique. The key however is to ensure that the observed process in any given sample is not significantly, or at least as little as possible, influenced by the light used during observation. In live imaging, we should avoid the lure of the 'pretty picture'. A good live image may require neither high contrast nor high spatiotemporal resolution, but needs to show that sample health was not, or only insignificantly, compromised by light exposure. This may produce grainy images with low contrast and moderate spatiotemporal resolution – which is perfectly acceptable and may even be encouraged, as long as the information so derived is sufficient to draw robust conclusions from the observed process.

Chapter II: Materials and Methods

Note: Materials and Methods described below are those commonly used throughout the project. Procedures that were adapted to the use of a specific cell line, and are thus not as general, are described in corresponding 'Materials and Methods' sections of individual 'Results' chapters.

II.1 Materials

II.1.1 General laboratory materials and reagent

Standard chemicals and reagents were ordered from Sigma Aldrich (UK); Dimethyl Sulphoxide (DMSO), formaldehyde 16 %, Tween-20, bovine serum albumin (BSA), Triton-X 100, super optimal broth (SOC-10X) medium, Hydrogen peroxide solution 30%, glycerol, Tris Base, Acetic Acid, EDTA, ampicillin, kanamycin, G418, tryptone, yeast extract, agar and tetracycline. Other chemicals such as Sodium chloride, acetone, ethanol, methanol and Virkon were from Fisons (UK). DMEM (Dulbecco's modified Eagle's medium), DMEM/F12, FBS (fetal bovine serum), RPMI 1640 (Roswell Park Memorial Institute), trypsin, L-glutamine, penicillin-streptomycin were purchased from SLS (UK). PBS (phosphate buffered saline 10x) was purchased from Fisher Scientific (UK). FluoroBrite™ DMEM, SYBR-Safe, 6x DNA loading dye, GeneRuler 1 kb DNA Ladder and TrypLE™ were purchased from Thermo Fisher Scientific (UK). Immersion oil type LDF was purchased from Cargille Labs (USA). VECTASHIELD DAPI HardSet mounting Medium was purchased from Vectorlabs (UK).

II.1.2 Antibodies used in this study

Primary antibody: Anti-Calnexin rabbit monoclonal antibody (Abcam ab92573, UK).

Secondary antibody: Rhodamine conjugated goat anti-rabbit IgG-R (Santa Cruz Biotechnology sc-2091, UK)

II.1.3 Plasmids used in this study

The plasmids used in this study, together with their bacterial resistances and sources are listed in Table II-1.

II.1.4 Cell lines used in this study

The mammalian cell lines used in this study are listed in Table II-2

II.1.5 Media and buffer preparation

All media were prepared in nanopure water and either autoclaved or filter-sterilised prior to use. When pouring plates, bench area was kept sterile by working near a flame or bunsen burner.

II.1.5.1 Preparation of LB medium

To prepare 500 mL of LB medium; 5 g NaCl, 5 g Tryptone, 2.5 g Yeast Extract were added into a 500 mL glass bottle; dH_2O was added to complete 500 mL. The previous mixture was autoclaved and allowed to cool at room temperature.

Table II-1 Plasmids used in this study

Plasmid	Bacterial resistance	Source	Organization
pMT4-WT-Rhodopsin-GFP pMT4-P23A-Rhodopsin-GFP pMT4-P23H-Rhodopsin-GFP pMT4-P23L-Rhodopsin-GFP	Ampicillin	Dr. Philip Reeves	School of Biological Sciences, University of Essex
mCherry-Calnexin-N-14	Kanamycin	Michael Davidson	Addgene # 55005
pC1-HyPer-3		Vsevolod Belousov	Addgene # 42131

Table II-2 Cell lines used in this study with culture media and solutions

Cell Lines	Description	Media **	Source	Organization
HEK293S tetR*	Tetracycline inducible stable human embryonic kidney cell	DMEM/F 12	Dr. Philip Reeves	School of Biological Sciences, University of Essex
GMK	Green monkey kidney cell	DMEM	Dr. Glyn Stanway	
PC3-GFP	Human prostate cancer cell	RPMI 1640	Dr. Greg Brooke	

* HEK293S tetR grown only under the selection of G418 500µg/ml
** Media were supplemented with FBS (10% v/v), 100 µg/ml penicillin-streptomycin and 2 mM L-glutamine.

II.1.5.2 Preparation of 1x TAE buffer

Initially, 50 x TAE buffer (Tris- Acetic Acid -EDTA), was prepared by adding 242 g Tris Base, 57.1 ml Acetic Acid, 37.2 g EDTA, to 1 L dH_2O. 1 x TAE was prepared by diluting 20 ml of stock to 980 ml of dH_2O_2.

II.1.5.3 Preparation of LB agar selection plates

To prepare 500 mL of LB agar: 5 g NaCl, 5 g Tryptone, 2.5 g Yeast Extract, 7.5 g Agar were measured out into a 1L glass bottle, dH_2O was added to bring it up to 500 mL. The previous mixture was autoclaved for 20 minutes after which it was allowed to cool to 55°C. An appropriate amount of desired antibiotic was added (final concentration of: 100 µg/ml for Ampicillin or 50 µg/ml for Kanamycin) to the solution. About 20 mL of the previous LB agar was added per 10 cm polystyrene Petri dish.

II.2 Methods

II.2.1 Bacterial transformation

Bacterial transformation was achieved using NEB 10-beta competent *E.coli* (C3019,New England BioLabs, MA, USA). According to the protocol supplied with the cells, cells were thawed on ice and 50 µl of cells was mixed and transferred into a transformation tube. Then 5 µl of the desirable plasmid construct was added into the transformation tube, the mixture was incubated on ice for 30 min, heat-shocked at 42 °C for 30 s, then returned immediately to ice for 5min. 950 µl of room temperature SOC medium was added into the mixture, which was then placed at 37°C for 60 min. After performing several 10-fold serial dilutions (1:10, 1:100, and 1:1000) in SOC,

100 µl of each dilution were spread onto the pre-warmed LB agar selection plates containing the plasmid's designated selection antibiotic (100 µg/ml for Ampicillin, 50 µg/ml for Kanamycin). The plates were incubated at 37°C for 24 hours.

From each plate, 2 colonies were picked to check for correct insertion of the plasmid. By using sterile pipette tips, each single colony was inoculated into 5 ml LB medium with the plasmid's appropriate selected antibiotic (Table II-1). The culture was allowed to grow overnight at 37°C while shaking at 250 rpm in a KS 400 ic control incubator shaker (IKA, Staufen, Germany). In cryo tubes (Thermo fisher, UK), 500 µl taken from the overnight culture was mixed with 500 µl of 80% glycerol and stored at -80°C as glycerol stock. This stock was to be used for large scale plasmid DNA preparation and also for long-term storage of plasmids. In order to validate the plasmid within the culture from the isolated colonies, the remaining culture was used for isolation of plasmid DNA.

II.2.2 Small scale preparation of plasmid DNA

The isolation of the plasmid DNA from cultures was performed using a QIAGEN QIAprep® spin miniprep kit (Cat.no.27104, Germany) according to the manufacturer's instructions. 4.5 ml bacterial overnight culture was centrifuged (MultiFuge 3 S-R, Germany) at 10,000 rpm for 3 min at room temperature, and then the cells were resuspended in 250 µl P1 buffer and transferred into Eppendorf tubes. After adding 250 µl P2 buffer, tubes were mixed thoroughly, then the same process was repeated with 350 µl N3 buffer. Tubes were centrifuged (Eppendorf centrifuge 5417R, Germany) at 13,000 rpm for 10 min, and the supernatant was transferred into QIAprep spin column for 45s centrifuging in a table top centrifuge (ScanSpeed mini).

After adding 500 µl buffer PB, they were centrifuged as before, also after adding 750 µl buffer PE. Finally, any residual washing buffer was removed by 1 min centrifuging, and plasmids DNA was eluted by adding 50 µl buffer EB which was measured by Nano drop ((NanoDrop Technologies, USA). Samples of DNA then validated ether by restriction enzyme digestion or by observing by means of fluorescence microscopy whether or not the plasmid cellular transfection give the correct cellular localization.

II.2.3 Restriction digestion

Restriction digests of plasmid DNA (up to 10 µg) were completed using the appropriate buffer, and 20-50 units of appropriate enzyme with time and temperature as recommended by the manufacturers as shown in Table II-3. The resulting digest was confirmed by agarose electrophoresis.

II.2.4 DNA gel electrophoresis

All DNA samples prepared from restriction digestion were mixed with 1/5 vol of DNA loading dye and then loaded into wells of 1% agarose gel (agarose melted in 1 x TAE buffer (Material,II.1.5.2)), which had been pre-stained with SYBR-Safe (0.1 µl of stock solution per ml of agarose gel). A 1 kbp DNA ladder was applied as a size standard. The gel electrophoresis (Fisher Scientific, UK) was run at 100 V (EC250-90 power supply, Thermo, USA) for 60 min. UV visualization of the DNA bands was carried out via InGenius^3 gel documentation systems (Syngene, USA). The colonies of

Table II-3 Restriction enzymes used in this study

Plasmids	Enzyme*/ Cat number	Incubation Temp	Buffer with concentration ** / Cat number
pMT4-WT-Rhodopsin-GFP	EcorI /R0101 NotI /R0189	37°C	O buffer (1x) / BO5
pMT4-P23A-Rhodopsin-GFP			
pMT4-P23H-Rhodopsin-GFP			
pMT4-P23L-Rhodopsin-GFP			
mCherry-Calnexin-N-14	xHO1/R0146 Age1/R0552 Not1/R0189	37°C	R buffer (1x) / BR5

Suppliers: *New England Biolabs, UK / **Thermofisher, UK

validated DNA sample were then used for the preparation of large scale plasmid DNA.

II.2.5 Large scale preparation of plasmid DNA

QIAGEN HiSpeed® Plasmid Midi kit (Cat.no.12643, Germany) was used in DNA preparation according to the kit instructions. Bacteria was recovered from the -80°C glycerol stock (section II.2.1), by opening the cryo tube and scraping some of the frozen bacteria off of the top with a toothpick or pipette tip . Bacteria were streaked onto an LB agar plate containing the appropriate antibiotic. The plates were incubated at 37°C for 24 hours. A single colony was picked by sterile pipette tip. The colony was inoculated into 10 ml LB medium with the appropriate antibiotic. The culture was allowed to grow for 6 hrs at 37°C while being shaken at 250 rpm in a KS 400 ic control incubator shaker (IKA, Staufen, Germany). 200 µl of antibiotic was added to 200 ml LB and the 6 hrs growth mixture was transferred to the 200 ml LB and incubated overnight at 37 ^{o}C on the shaker at 250 rpm. The growth culture was then centrifuged for 15 min at 4 ^{o}C centrifuge at 6089.52 x g. The bacterial pellet was then resuspended in 6 ml P1. 6 ml of P2 was added and mixed by inverting 4-6 times then incubated for 5 min at RT. The pellet was then lysate in 6 ml of P3. The lysate was poured into a prepared QIafilter Cartridge and incubated at RT for 10 min. During the incubation time, the HiSpeed Midi Tip was equilibrated by 4 ml QBT buffer. The cell lysate was then filtered into the equilibrated filter by gravity flow. The QIAGEN-tip was then washed with 20 ml QC. The filter tip was then placed on a clean bottle and the DNA was eluted with 5 ml QF. Next the DNA was precipitated by adding 3.5 ml isopropanol and incubated for 5 min at RT. A 20 ml syringe was prepared by

removing the plunger and attaching the QIAprecipitator to the outlet nozzle. The eluate mixture was then transferred into the syringe and the plunger was inserted with a constant pressure to filter the DNA. The QIAprecipitator was removed and the plunger pulled out before the QIAprecipitator was re-attached and 2 ml of 70 % ethanol added in order to wash the DNA. The membrane was then dried by pressing air through the QIAprecipitator using constant pressure, a step repeated 3 times. A 5 ml syringe was prepared, the QIAprecipitator was attached to the outlet nozzle and 1 ml of buffer TE was added. The DNA was eluted in the collection tube using constant pressure. The QIAprecipitator was removed and the plunger was pulled out then, the QIAprecipitator was reattached and the eluate was transferred to the 5 ml syringe and eluted for a second time in the same collection tube. The DNA was then aliquoted into 5 tubes, each a 1.5 ml tube with a volume of 200 µl. DNA yield was quantified with Nanodrop® (NanoDrop Technologies, USA). DNA samples were stored at –20°C. The plasmid DNA was diluted to a final concentration of 1 µg/µL.

II.2.6 Growth and maintenance of cell lines in tissue culture

All culture work was carried out using standard aseptic techniques, unless otherwise specified. Growth medium, trypsin and 1 x PBS were always heated to 37°C before being applied to cell cultures, unless otherwise specified.

All cell lines in this study (see Table II-2) were adherent and were grown inside SANYO CO2 incubator (MCO-18AIC, China) at 37 °C, 5 % CO_2 in 75 cm^2 flasks (Thermo fisher, UK), unless otherwise specified. Cells were passaged at 70-80% confluence at every 3 to 4 days.

II.2.6.1 Thawing of cells

Cells were recovered from liquid nitrogen storage and thawed for 2 min at 37°C in a water bath, then immediately removed from the vial using a sterile pipette and diluted in 10 ml of the appropriate fresh growth medium (Table II-2).

II.2.6.2 Cell passaging

When a cell culture density reached greater than 80% confluency, cells were sub-cultured. The media was aspirated and the cells were washed in 1 x PBS. To detach the cells from the flask, the cells were then incubated with 1 ml of trypsin or TrypLE™ at 37°C for 3 to 5 minutes. 9 ml of pre-warmed media were then added to inactivate the trypsin. Cell clumps were disrupted with gentle pipetting or flask shaking. From then the cells were either frozen, distributed into fresh flasks for sub-culturing or were counted and aliquoted for experimental procedures.

II.2.6.3 Cell counting

Cells were counted with a haemocytometer (Sigma, UK) with a 0.1 mm sample depth and light microscope (Olympus, UK).

II.2.6.4 Cell freezing

For frozen storage, 90% confluence cells were harvested by trypsinisation (section II.2.6.2). After trypsin inactivation, cells were transferred to a centrifuge tube and centrifuged by Megafuge8 (Thermo Scintific, USA) at 1000 rpm for 3 min at room temperature. Cell pellets were resuspended at a density of approximately 3 x 10^6 cells per ml in 90% complete medium and 10% DMSO in a cryo tube or vials. Vials were

frozen at -20°C for 12 to 24 hours before permanent storage in the gas phase of a liquid nitrogen vessel (at -180°C). Cells were recovered by rapid thawing at 37°C as mention in section II.2.6.1.

II.2.6.5 Transient transfection of the adherent cells

One day before transfection 3 x 10^4 cells were seeded on round 13 mm glass cover slip (VWR,USA) in 1 ml antibiotic free medium supplemented with 10 % FBS in a 24-well plate. Transfection of the cells was performed using TurboFect Transfection Reagent (Thermo Scientific, Lithuania) according to the manufacturer's manual. 1 µg DNA was mixed with 2 µl TurboFect and 100 µl serum-free, antibiotic- free media and incubated for 15 min at room temperature. This mixture was then added to cells. Cells were incubated for 24-48 hrs after transfection. Empty vector contains GFP (see Appendix A) and empty mCherry vector (see Appendix B) were used as controls.

II.2.7 Cell fixation for immunofluorescent staining

Growth medium was removed, cells on the coverslips were fixed with 3.7 % cold formaldehyde for 15 minutes, permeabilised for 15 minutes with 100 % ice-cold methanol at -20 °C following the Sequential fixation protocol (Schnell *et al.*, 2012). This protocol was evaluated by comparing the signal to noise ratio of samples; one was done according to the classical fixation protocol (Formaldehyde fixation without methanol), and the other by methanol sequential fixation (see Appendix C). Blocking was done for 1 hour with 10% BSA. The fixed cells were then probed for 1 hour with 1:1000 dilution of the primary antibody in 5% BSA. Excess primary antibody was removed by washing three times with 1% BSA, 0.1% Tween 20. The cells were

subsequently probed for 1 hour with a 1:1000 dilution of secondary antibody in 5% BSA, 0.2% Tween 20. Excess secondary antibody was removed by washing three times with 0.1% Tween 20 and the glass cover slips were mounted onto glass slides in (Vectashield) hard setting DAPI mounting media. A negative control sample was done following the exact previous procedures except the cells were not incubated with the primary antibody (see Appendix D).

II.2.8 Sample mounting for live imaging

Techniques for this differed slightly according to the cell line used. Details are found in the respective methods sections in chapter IV and V.

II.2.9 Microscopy and image acquisition

Two microscopes were used in this study as listed in Table II-4. Image acquisition parameters are modified in response to the microscope in use and/or to the sample of interest. Particular cases are described in the corresponding 'Materials and Methods' sections of individual 'Results' chapters.

II.2.10 Bioimaging software

Various software packages dedicated either to statistical analysis or bioimaging were used in this study and are listed in Table II-5.

Table II-4 Microscopes used in this study

Microscope	Model	Light sources
Confocal laser scanning microscope (CLSM)	Nikon A1-Si	Laser; Violet Diode Laser 400-405 nm* Argon-Ion Laser 457-514 nm* Sapphire Laser 561 nm** Red Diode Laser, 642nm*
Wide-field Fluorescence microscope (WFM)	Nikon Eclipse Ti-E	CoolLED pE excitation system*** Intensilight Halogen lamp

Manufacturers: *Melles Griot, USA / ** Coherent, USA *** CoolLED, UK

Table II-5 List of software used is this study

Software	Used for
NIS-Elements AR 4.13.01 (Build 916) (Nikon, Japan)	Image acquisition and visualisation
NIS-Elements AR 3.21.03 (Build 705) (Nikon, Japan)	Image visualisation, pre-processing, processing and analysis
MATLAB version R2010b with Image Processing Toolbox (Math-Works Inc., Natick, Massachusetts)	Image quantification and blob detection
FIJI open source (Schnell et al., 2012).	Image visualisation, processing and analysis
CellTracker (Piccinini et al., 2016)	Tracking and quantifying cellular movement
SPSS 19 (IBM, USA)	Graphing and statistical analysis
GraphPad Prism 7 (GraphPad, USA)	Graphing and statistical analysis
PyMOL v 1.8 (Schrodinger, 2015)	Molecular visualization system
AutoQuant X v 2.2.1 (Media Cybernetics, USA)	Image deconvolution
BOColocalisation3D_GUI (Obara *et al.*, 2013)	3D blob-like feature detection

II.2.11 Bioimaging project workflow

The flow chart in Figure II-1 illustrates the main routine for image quantification used in this study. Sample preparation includes all the experimental approaches prior to the image acquisition session. After collecting images by microscopy an image processing step is required. However before image processing, all datasets should be checked for cellular integrity and signal strength. Cells that appear damaged, have poor contrast or move during image acquisition considered not sufficient for robust quantification and need to be excluded from image quantification and analysed qualitatively. Background subtraction, noise reduction, isolation of single cells from cellular clusters and segmentation are all included in the image preprocessing step. Analysis is important for selecting the appropriate quantification parameter for each dataset. Image quantification (protein volume extraction, cell speed, cell proliferation, ratiometry, etc) can be achieved via MATLAB, NIS-Elements or CellTracker. Rigorous pruning after image quantification is also crucial, as the method is affected by outliers. If measured values of a subcellular structure in a particular dataset are markedly different from the other values in the same cohort, the original dataset and the binary stack associated with the subcellular structure in question should be checked; exclude dataset if the extraordinary values are due to a poor sample or questionable image processing.The extracted nominal and numerical data were imported to SPSS 19 and/or GraphPad Prism7. Significant tests and graphs were generated, results and conclusions formulated accordingly. If any of the images failed to be quantified, they would be considered insufficient for robust quantification and would be analysed qualitatively. Alternatively sample preparation can be repeat.

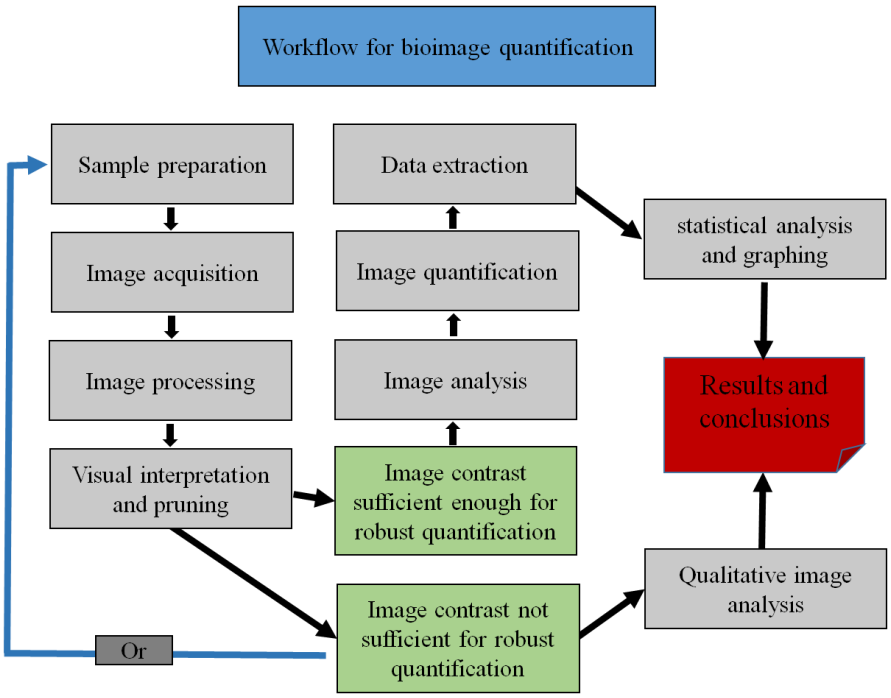

Figure II-1 Workflow chart illustrates the main routine for image quantification.

II.2.12 Image quantification algorithm

The proposed approach uses MATLAB software version R2014b with Image Processing Toolbox. All steps are based on analysis in 3D. We used combination of simple techniques (Gaussian filtering, Otsu thresholding, morphological filters), that can be easily reproduced. An 'agnostic' approach with no prior knowledge of structure required. Images were segmented using the Otsu method for local threshold (Noboyuki, 1979), by statistical examination of the intensity values of the local neighbourhood of each pixel. In our case, the mean of the local intensity distribution was used according to the following image segmentation algorithm.

$$B(x,y) = \begin{cases} 0 & \text{if} \quad I(x,y) < T(x,y) \\ 1 & \text{otherwise} \end{cases}$$

In the algorithm, I is an input image, B is a binarised image, and (x; y) is a pixel location of the image. T is an array of the mean values calculated at the local neighbourhood of each pixel within a window of a size s x s. With the thresholding each colour channel image was separates into foreground (region of interest) and background (noise). This allows binary images to be generated. The resulting binary image stacks are then used to determine the volume of the objects of interest in each colour channel (Obara *et al.*, 2013).

Chapter III: Automated image quantification for Rhodopsin phenotypes in a cell model for Autosomal Dominant Retinitis Pigmentosa

III.1 Introduction

Retinitis Pigmentosa (RP) is a neurodegenerative disorder defined by photoreceptor cell death and gradual loss of vision (Phelan and Bok, 2000; Rattner et al., 1999). It is characterised by retinal pigment deposits visible on fundus examination (Hamel, 2006), and estimated to affect one in 3000–5000 individuals worldwide (Kisselev, 2005). RP can be inherited in an autosomal dominant manner (Gal et al., 1997). One in four patients with such Autosomal Dominant Retinitis Pigmentosa (ADRP) will have mutations in the opsin gene. The product of the opsin gene is a glycoprotein which, together with the pigment 11-cis-retinal, forms rhodopsin. Rhodopsin is responsible for vision under dim light condition (Sakmar and Huber, 2009). Over 150 different opsin mutations are linked to ADRP (Garriga and Manyosa, 2002). Proline substitution by histidine at position-23 (P23H) was the first identified rhodopsin mutation (Dryja et al., 1990), it accounts for approximately 12% of North American ADRP patients. P23H mutant opsin shows inefficient regeneration with 11-*cis*-retinal and does not traffic normally to the outer segment of the rod cell. It aggregates in the endoplasmic reticulum, leading to ER stress and activating the unfolded protein response (UPR) (Kaushal and Khorana, 1994; Sung *et al.*, 1991a). P23A is a rare mutation in the rhodopsin gene. Patients with the P23A mutation show mild ADRP (Oh *et al.*, 2000). Another mutation associated with ADRP is P23L (Sung *et al.*, 1993).

Maintaining cellular protein homeostasis is critical for a cell's viability, the presence of mutant proteins will increase the demand for protein quality control (Hebert and Molinari, 2007). Mutant rhodopsin disrupts protein homeostasis in photoreceptor cells during retinal degeneration, accumulation of this misfolded proteins triggers cellular stress responses (Kroeger et al., 2012). Endoplasmic reticulum (ER) contains a large

number of resident molecular chaperones that support protein maturation and orchestrate the quality control system that retains misfolded proteins and targets them for degradation (Hebert and Molinari, 2007). Calnexin (CNX) is a lectin-like chaperone, reported to be important for quality control of glycoproteins (Schrag et al., 2001). Mutant rhodopsin has been reported to show an increased association with CNX for a better chance of correct folding (Saliba et al., 2002), although the exact nature of rhodopsin interaction with CNX is not fully known (Noorwez et al., 2009). Many researchers have investigated the severity of rhodopsin mutations and how they manifest in animal and/or cellular models together with the possible ways of counteracting these mutations by pharmacological means or by gene delivery (Gorbatyuk et al., 2012; Krebs et al., 2010; Mendes and Cheetham, 2008; Noorwez et al., 2003; Noorwez et al., 2009; Noorwez et al., 2008; Opefi et al., 2013). In this chapter, instead of analysing these mutations by performing the common biochemical experiments, we have taken an entirely different approach. Our objective was to examine an automated image analysis algorithm to quantify and determine the distribution of rhodopsin phenotypic variations within and among the cellular models for autosomal dominant retinitis pigmentosa using 3D digital microscopy.

III.2 Experimental procedures and statistical analysis

III.2.1 Sample preparation

Inducible HEK293S tetR stable cell lines expressing wild-type, P23A and P23H were grown at a concentration of 1:1 in DMEM/f12 with heat-treated (55 °C, 30 min) FBS (10% v/v), 100 µg/ml penicillin-streptomycin and 2 mM L-glutamine, with an atmosphere of 5% CO_2 at 37°C to an approximate confluence of 70%. One day before

antibody staining, the cells from cell cultures were seeded on glass cover slips in 24 well-plates, grown in DMEM containing glucose, supplemented with L-glutamine and penicillin-streptomycin (50 µg/ml), then kept for 5 hours at 37°C in a humidified 5% CO_2 atmosphere. After 5 hours the cells were induced by tetracycline (2µg/ml), and then incubated overnight at 37°C in a humidified 5% CO_2. After 24 hours, induced cells were fixed with 3.7 % cold formaldehyde for 15 minutes, and permeabilised for 15 minutes with 100 % ice-cold methanol at -20 °C following the Sequential fixation protocol (Schnell *et al.*, 2012). Moreover, blocking was done for 1 hour with 10% BSA. The fixed cells were then probed for 1 hour with CNX rabbit mAb (Abcam ab92573, 1:1000 dilution) in 5% BSA. Excess primary antibody was removed by washing three times with 1% BSA, 0.1% Tween 20. The cells were subsequently probed for 1 hour with a 1:1000 dilution of Rhodamine conjugated goat anti-rabbit IgG-R (Santa Cruz sc-2091) in 5% BSA, 0.2% Tween 20. Excess secondary antibody was removed by washing three times with 0.1% Tween 20 and the cover slips were mounted onto glass slides in (Vectashield) hard setting DAPI mounting media. Glass slides were kept inside the fridge overnight prior to image acquisition.

Images for P23L rhodopsin mutation were courtesy of Dr. Philip Reeves, University of Essex. Those cells were maintained in the same cell culture condition and also subjected to the same immune staining steps as mention above. Unfortunately, for reasons uncertain, the signal-to-noise ratio of the majority of images was poor; the small number of images with sufficient contrast (n=15) was used for visual inspection, while the remainder were used as negative controls for image processing procedures.

The pharmacological rescue of P23H and P23L mutations was done by the group of Dr. Philip Reeves, University of Essex (Opefi *et al.*, 2013). After the induction by

tetracycline cells expressing P23H and P23L mutation was additionally treated with 0.2µl 100 mM 11- *cis* retinal in DMSO and then incubated and fixed using the same conditions described in Materials & Methods (Opefi *et al.*, 2013).

III.2.2 Image acquisition

A Nikon A1si confocal microscope was used with a plan-apochromatic VC 1.4 N.A. 60x magnifying oil-immersion objective. The software used for image acquisition was NIS-Elements AR 4.13.01(Build 916). Images were acquired in four channels, using one-way sequential line scans. DAPI was excited at 400 nm, and its emission collected at 450/50 nm with laser power 6.6 AU. GFP was excited at 488 nm, its emission collected at 525/50 nm with laser power 4.8 AU. Rhodamine signal was excited at 561 nm and collected at 595/50 nm with laser power 9.7 AU. Scan speed was ¼ frames/s (galvano scanner). The pinhole size was 34.5 µm, approximating 1.2 times the Airy disk size of the 1.4 N.A. objective at 525 nm and 1.00 x zoom. Scanner zoom was centered on the optical axis and set to a lateral magnification of 60 nm/pixel. Axial step size was 105 nm, with 80-100 image planes per z-stack. Identical settings were used for all acquired datasets, following the Nyquist–Shannon's reconstruction theorem (Nyquist, 1928; Shannon, 1949) with a pixel size of 60 nm.

III.2.3 Image pre-processing and automated image quantification algorithm

Commercial software (Nikon NIS-Elements; 64bit 3.21.03, Build 705) was used for image pre-processing as mentioned in the methods section II.2.11. The acquired channels were assigned using the following names; blue (DAPI) channel representing

the nucleus ‘nucleus-DAPI’, the green (EGFP) channel representing ‘rhodopsin-GFP’ and the red channel of the monoclonal antibody (mAb) representing CNX-mAb.

Finally, automated quantification of single cells was achieved to determine the volume of each channel in µm³ (section II.2.12).

III.2.4 Aggresome detection algorithm

Inclusion bodies (aggresomes) within the cellular structure were detected and counted via the 3D blob-like feature detection algorithm introduced by Obara and co-workers (Obara et al., 2008). This object-based algorithm is run as a graphical user interface (BOColocalisation3D_GUI) on MATLAB software (Obara et al., 2013). Visual inspection was also carried out afterwards to detect counts arising from local maxima within the membrane. As aggresomes are cytoplasmic, these were excluded then aggresome numbers were counted accordingly.

III.2.5 Statistical analysis

After automated quantification, all numerical data that represents the volume in µm³ of the different cellular components were imported into SPSS software for statistical analysis. Detection of data outliers was done simultaneously with the visual inspection of the cells. A nonparametric test for independent samples (Kruskal-Wallis) was used to compare the means of different data. Furthermore, Dunn’s nonparametric pairwise multiple comparisons test was used to test the significance between different phenotypes. In all cases, a p-value of ≤ 0.05 was considered to be significant. Astrike symbols were used to indicate statistical significance (* $p \leq 0.05$).

All graphing was performed using the graphing and statistical software GraphPad Prism 7. Box plots represent 25–75 percentiles and whiskers were assigned using the Tukey method (Tukey, 1977). Values on some of the graphs were plotted on a logarithmic scale in order for the data to spread out clearly. Pie charts were used to illustrate the percentages of the cellular component within each phenotype.

III.3 Results

III.3.1 Sample size

Total of 504 fixed cells were included in both visual interpretation and statistical analysis (Wild-type (WT) n= 143, P23A n= 96, P23H n=188, P23Hresc n=47, P23L n=15 and P23Lresc n=15). Moreover, 10 random cells from each phenotype were selected for aggresome count and inspection.

III.3.2 Visual interpretation of rhodopsin-GFP expression and localisation with the endoplasmic marker

Figure III-1 shows inducible stable HEK293S cell lines expressing different rhodopsin-GFP phenotypes and immunostained against CNX. In WT cells, the rhodopsin-GFP signal localised mainly to the plasma membrane. There was poor overlap with CNX-mAb as shown in Figure III-1b. Some of P23A rhodopsin-GFP localized to the plasma membrane, whereas, some of it overlapped with CNX-mAb (Figure III-1c). Numbers of inclusion bodies or aggresomes were spotted in the cytoplasm in all mutations, with minute in WT.

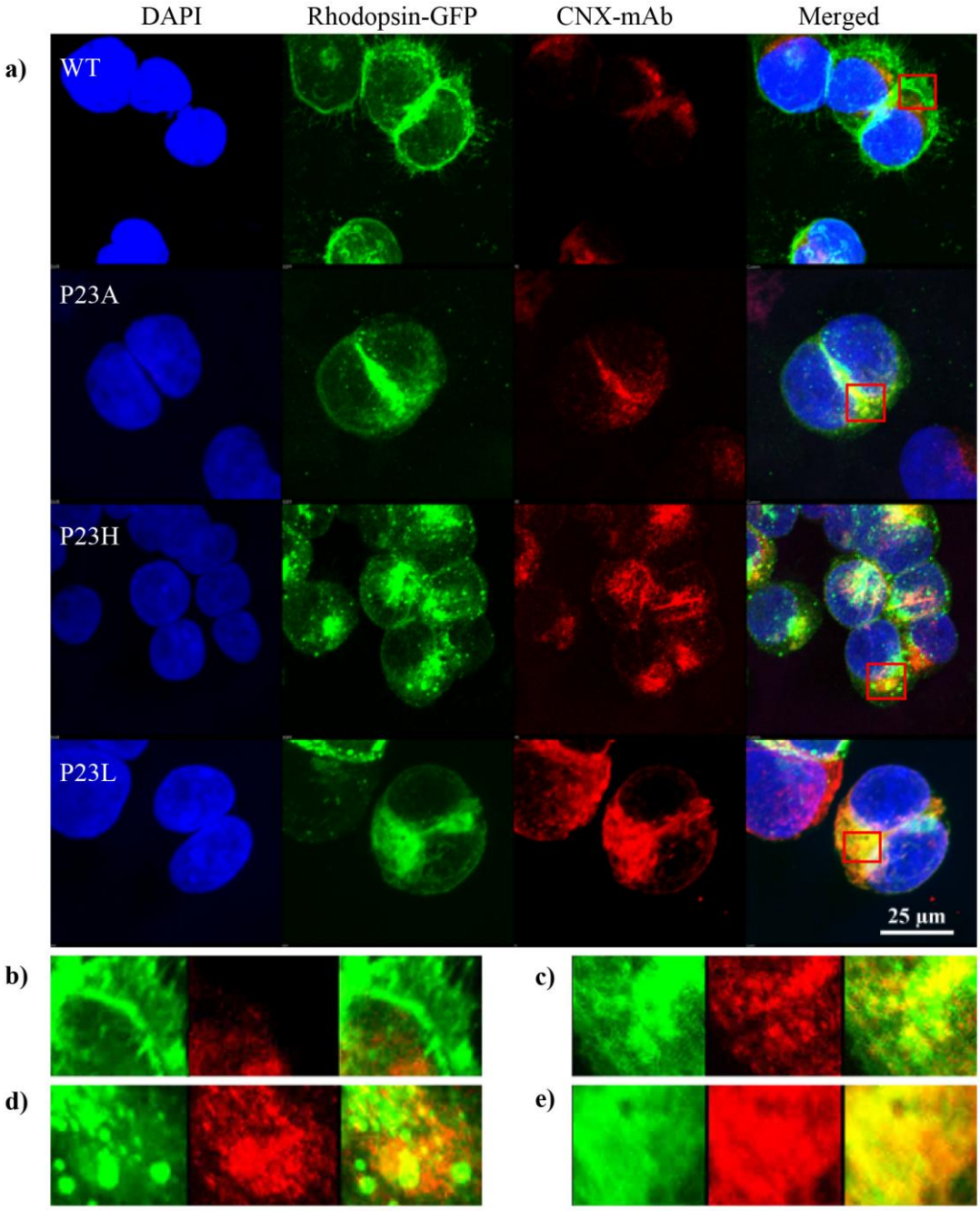

Figure III-1 Maximum intensity projection showing the localisation of rhodopsin-GFP and CNX-mAb in stable HEK293S cells expressing different rhodopsin-GFP phenotypes.

The cells are immunofluorescently labeled with CNX and DAPI-stained nuclei. There is poor plasma membrane localisation and aggresome formation of rhodopsin-GFP in P23A, P23H and P23L. Closeups (50x) of the regions highlighted by the red squares are then illustrated at the bottom. The overlap of rhodopsin-GFP with CNX-mAb is demonstrated on the images. b) WT shows less overlap with CNX-mAb. On the contrary, there is high colocalisation of c) P23A, d) P23H and e) P23L with CNX-mAb.

P23H and P23L mutant cells showed cytoplasmic clumps of rhodopsin-GFP which were retained within the cytosol as shown in Figure III-1 (d) and (e) respectively. Furthermore, they showed poor plasma membrane localisation with higher overlap with CNX-mAb.

Visual interpretation of all P23L and P23L-resc images revealed a poor signal-to-noise ratio in most cases. The datasets with sufficient contrast were used for qualitative assessment, but the low numbers did not allow for robust quantification. P23L rhodopsin datasets with poor contrast were thus used as a negative control for image processing.

III.3.3 Visual interpretation of mutant rhodopsin-GFP expression and localisation with CNX after pharmacological rescue

Figure III-2a shows inducible stable HEK293S cell lines expressing different rhodopsin-GFP phenotypes and immunostained against CNXusing a monoclonal antibody. P23H-resc and P23L-resc were rescued pharmacologically with 11- *cis* retinal. P23H-resc rhodopsin-GFP extended to the cellular membrane and showed fewer cytoplasmic clumps in contrast to P23H (Figure III-2b and c), which makes it more like WT. Meanwhile, P23L-resc appears concentrated within the cytoplasm area. The distribution of rhodopsin-GFP in P23L-resc is more like that seen in the non-rescued P23L mutant (Figure III-2.d and e).

III.3.1 Aggresomes count in the cellular model

Protein aggregates (aggresomes) were detected with BOColocalisation3D_GUI and confirmed by visual inspection. The allocation of these aggresomes within each

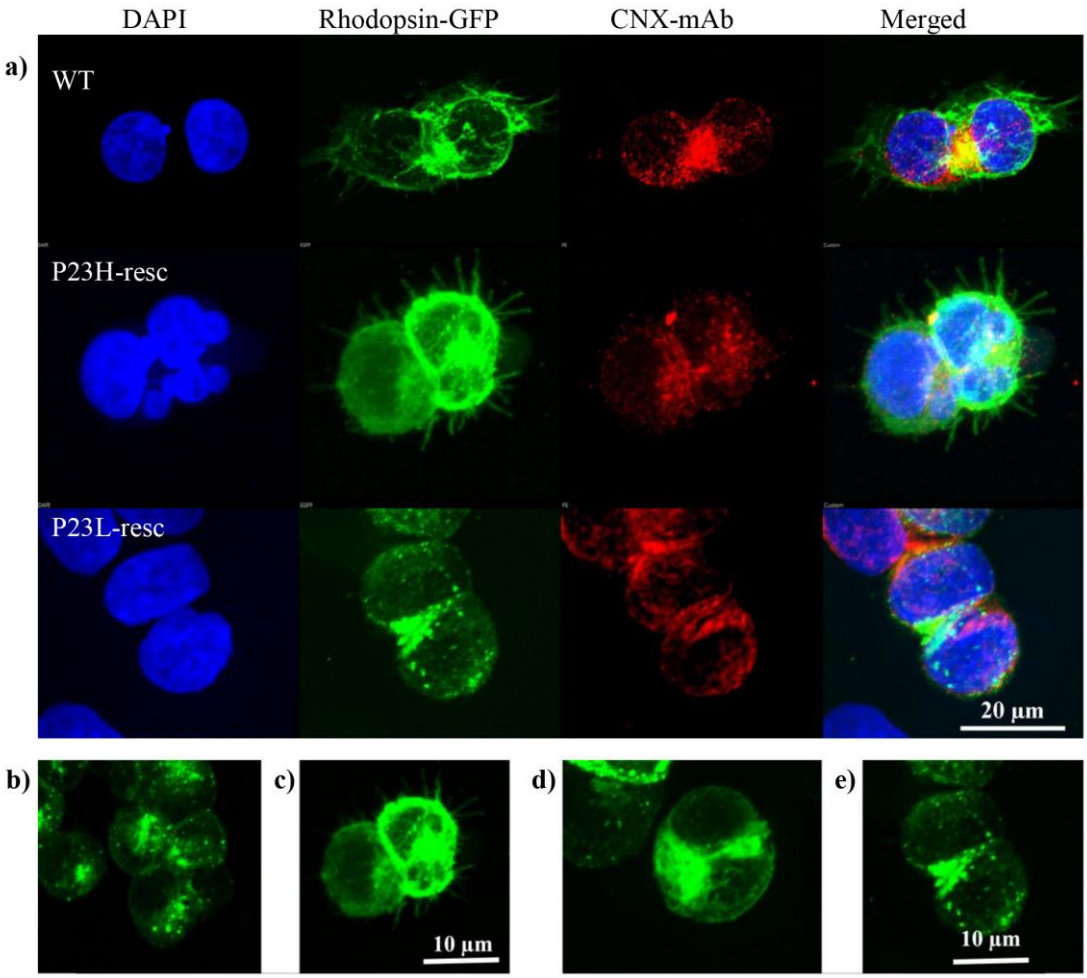

Figure III-2 Maximum intensity projection showing the colocalisation of rhodopsin-GFP and CNX-mAb in stable HEK293S cells

Cells are expressing different rhodopsin phenotypes: WT, P23H and P23L after pharmacological rescue with 11- *cis* retinal (P23H-resc, P23L-resc). The cells are immunofluorescently labeled with CNX and DAPI-stained nuclei. b). P23H shows poor plasma membrane localisation and aggresome formation of rhodopsin-GFP. c). P23H-resc rhodopsin-GFP extended to the cellular membrane and shows less cytoplasmic clumps which makes it more like WT. d) P23L. e) Rhodopsin in P23L-resc is concentrated within the cytoplasm area and its distribution is more like the non rescued P23L mutant.

phenotype is demonstrated in Figure III-3. While the previous approach identifies aggresomes in mutants reliably, it overestimates the number of aggresomes in WT by including local maxima of signal intensity in the plasma membrane. Visual inspection was carried out to exclude these counts. As a result, P23A, P23H and P23H-resc were found to show a higher accumulation of protein aggregates in the cytosol, whereas in WT the accumulation is lower. The distribution of aggresomes numbers for each phenotype is illustrated in the box and whiskers plot in Figure III-4. The highest medians value for aggresome counts was observed in P23H-resc followed by P23H, P23A and WT were 75, 67, 44 and 36, respectively. We found statistically significant differences between the total aggresome numbers for WT and both P23H and P23H-resc with $p<0.05$. In contrast, no statistical significance was found between WT and P23A.

III.3.2 Nucleus volume distribution

The box and whiskers plot in Figure III-5 represents the distribution of nucleus-DAPI volume across phenotypes. The highest medians for nucleus volume observed in P23H followed by P23A and WT were 971 μm^3, 927 μm^3, and 758 μm^3 respectively. We found a statistically significant difference between WT and P23A and P23H mutants with $p<0.05$ for nucleus-DAPI volume.

III.3.1 Quantification of rhodopsin-GFP phenotype

The box and whiskers plot in Figure III-6 represents the distribution of rhodopsin-GFP volume. The highest median for rhodopsin-GFP volume observed in WT was 44 μm^3, followed by P23A 36 μm^3 and P23H mutant 21 μm^3.

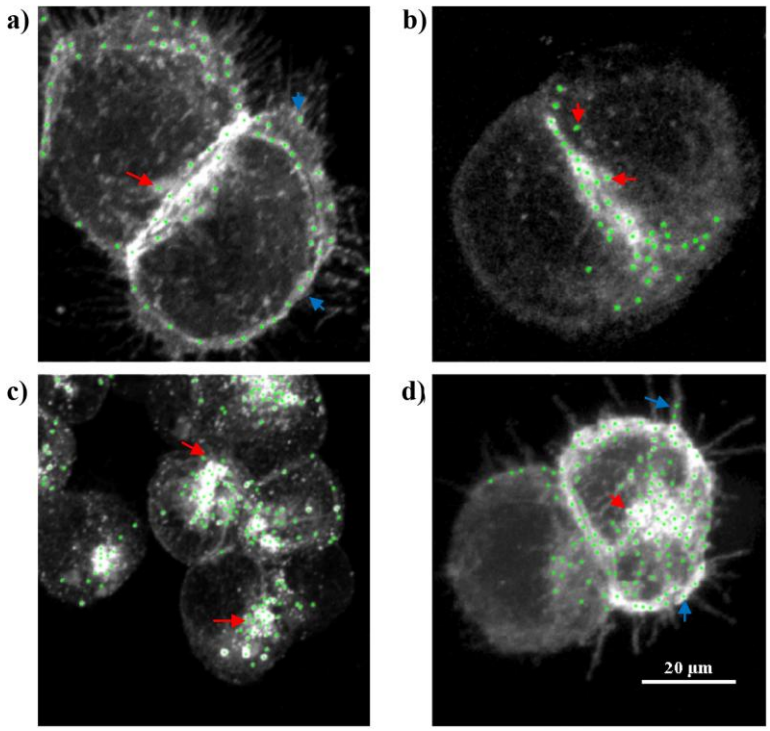

Figure III-3 Detection of rhodopsin-GFP protein aggregates on stable HEK293S cells using BOColocalisation3D_GUI.

a) WT. b) P23A. c) P23H. d) P23H-resc. The number of aggresomes was correctly detected within the cytoplasm region (red arrows). Whereas, some sections within the plasma membrane where the rhodopsin is translocated were incorrectly detected as aggresomes (blue arrows).

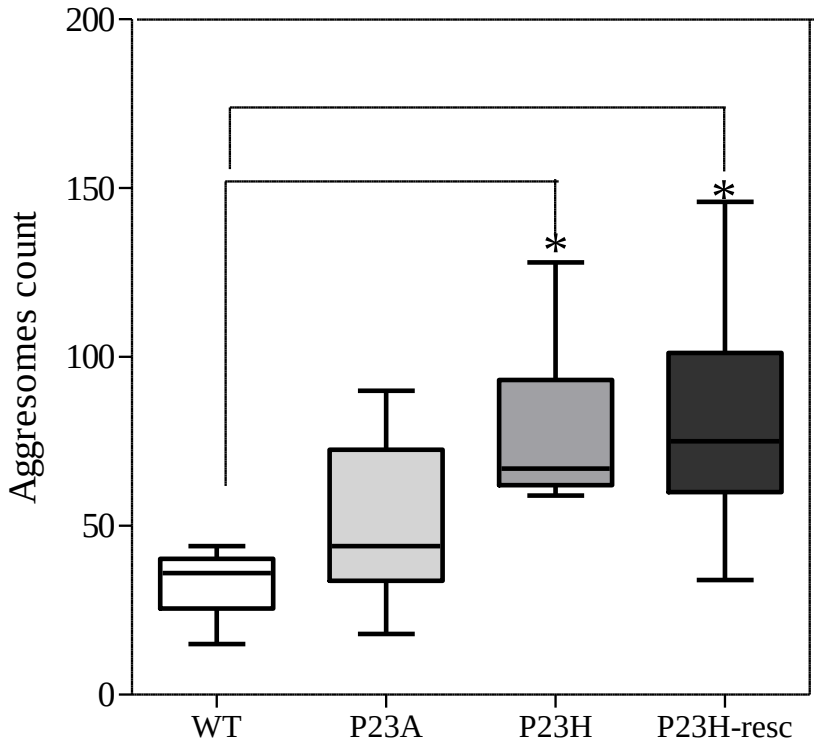

Figure III-4 Aggresome count in stable HEK293S cells.

The boxes in the plot represent the middle half of the distribution of the number of aggresomes, stretching from the 25th percentile to the 75th percentile. The bold line across the box represents the median (75, 67, 44, and 36) for P23H-resc, P23H, P23A and WT respectively. The lengths of the lines above and below the box define the maximum and minimum numbers of aggresomes, asterisks (*) denote $p < 0.05$ in comparison to WT**.**

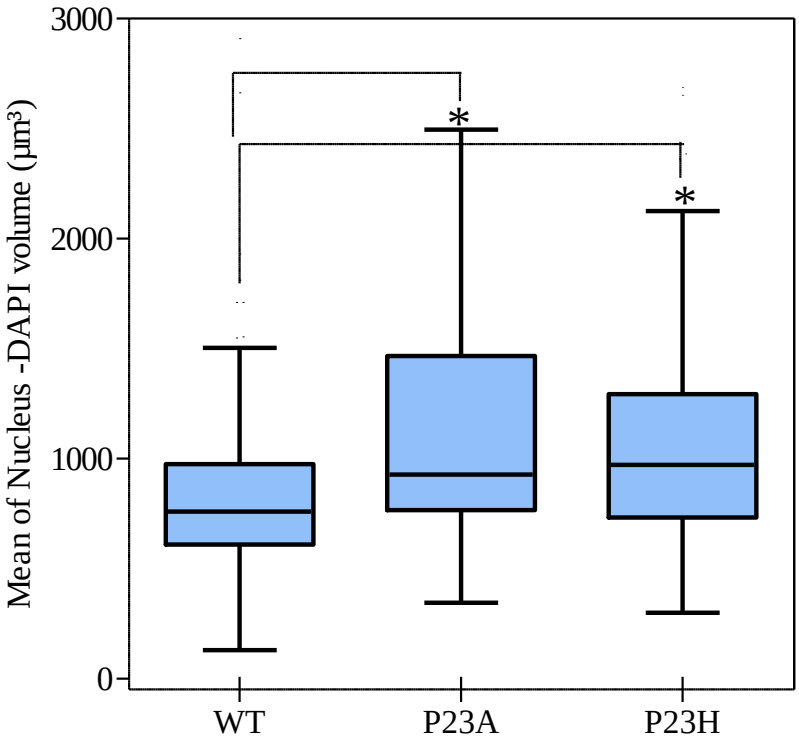

Figure III-5 Nucleus volume distribution in stable HEK293S cells.

The boxes in the plot represent the middle half of the distribution of the volume of nucleus-DAPI, stretching from the 25th percentile to the 75th percentile. The bold line across the box represents the median (971 µm³, 927 µm³, and 758 µm³) for P23H, P23A and WT respectively. The lengths of the lines above and below the box define the maximum and minimum nucleus-DAPI volume in µm³. Asterisks (*) denote $p < 0.05$ in comparison to WT.

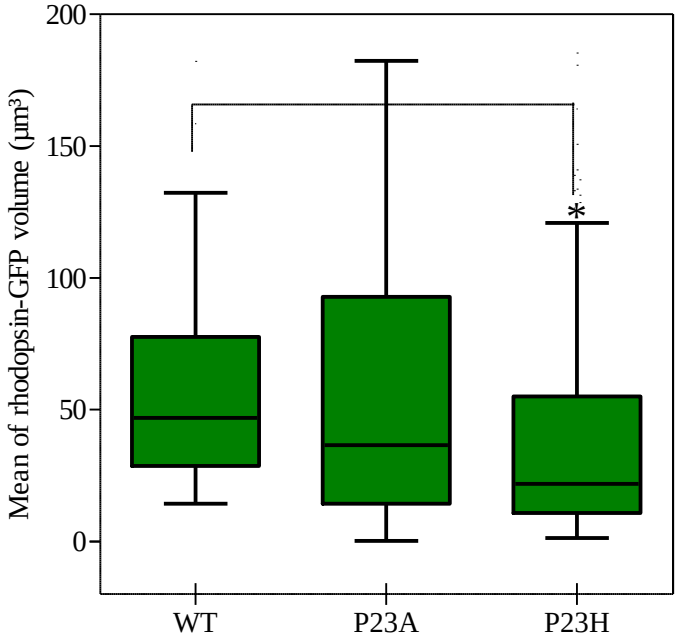

Figure III-6 Quantification of rhodopsin-GFP in stable HEK293S cells.

The boxes in the plot represent the middle half of the distribution of rhodopsin-GFP volume, stretching from the 25th percentile to the 75th percentile. The bold line across the box represents the median (44 µm³, 36 µm³ and 21 µm³) for WT, P23A and P23H respectively. The lengths of the lines above and below the box define the maximum and minimum rhodopsin-GFP volume in µm³. Asterisk (*) denotes $p < 0.05$ in comparison to WT.

Furthermore, we found a statistically significant difference in rhodopsin-GFP between WT and P23H $p<0.05$. In contrast, no statistical significance was recorded between WT and P23A.

III.3.2 CNX-mAb volumetry

The distribution of CNX-mAb volume is illustrated in the box and whiskers plot in Figure III-7. The highest median for CNX-mAb volume observed in P23H was 27 μm^3, followed by P23A 26 μm^3 and WT 23 μm^3. No statistical significance was recorded between WT and P23A, whereas the difference in CNX-mAb volume between WT and P23H mutant was statistically significant with a p-value of less than 0.05.

III.3.3 Overlap between rhodopsin-GFP and CNX-mAb

The box and whiskers plot in Figure III-8 represents the distribution of the overlap volume between rhodopsin-GFP and CNX-mAb. The highest median was observed in P23A (3 μm^3), followed by P23H (2 μm^3). WT rhodopsin-GFP showed an extremely low overlap volume (less than 1 μm^3). Furthermore, we found a statistical significant differences between WT and both P23A and P23H mutants for the overlap volume, $p<0.05$.

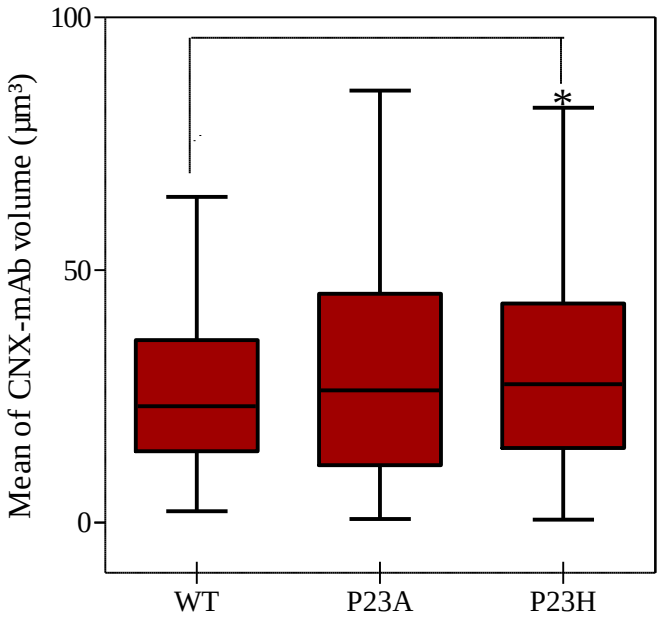

Figure III-7 Volumetry of CNX-mAb in stable HEK293S cells.

Box plots (25–75 percentile) and whiskers (Tukey method) showing comparisons of the distribution of CNX-mAb volume. The bold line across the box represents the median (23 µm³, 26 µm³ and 27 µm³) for WT, P23A and P23H respectively. Asterisk (*) denotes $p < 0.05$ in comparison to WT.

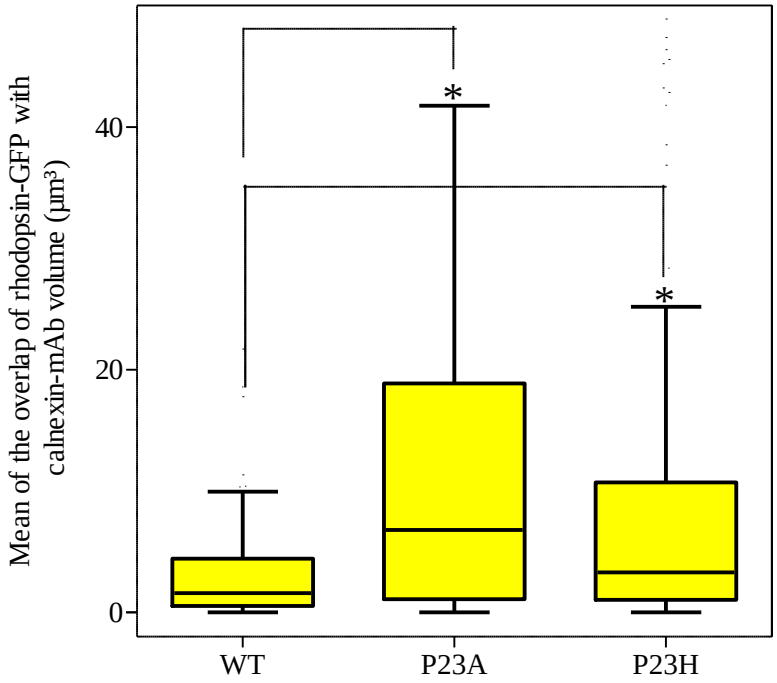

Figure III-8 Boxplots illustrating the overlap between rhodopsin-GFP and CNX-mAb in stable HEK293S cells.

Box plots (25–75 percentile) and whiskers (Tukey method), represent the middle half of the volume distribution for the overlap of rhodopsin-GFP with CNX-mAb. The bold line across the box represents the medianS (3 µm³, 2 µm³ and 1 µm³) for P23A, P23H and WT respectively. Asterisks (*) denote $p < 0.05$ in comparison to WT.

III.3.4 Quantification of rhodopsin and CNX in rescued ADRP mutations

Misfolding P23H was 'rescued' – i.e. correct folding was induced – by the addition of 11-*cis* retinal. We volumetrically determined the different components and compared rescued P23H to WT and P23H. Nuclear volumes (Figure III-9.a) were not significantly different between rescued mutant and both: WT and P23H. However, rhodopsin volume differences were statistically significant between P23H-resc and P23H. Moreover, the volumetry of CNX-mAb and it overlap within P23H-resc recorded to be also significantly different from P23H. In fact P23H-resc resembled the WT as there is no statistical significant recorded as shown in Figure III-9: (a,b, c and d).

III.3.5 Phenotypic characterization of the WT and ADRP mutations in the cellular model

ADRP mutations were characterized using their volume ratio as shown in the pie charts in Figure III-10. Each pie chart demonstrates the volume ratio of rhodopsin-GFP to CNX-mAb and their overlap in mutant ADRP in comparison to the WT. P23H was recorded to have: the lowest percentage of rhodopsin-GFP at 48% and with the highest percentage of CNX-mAb at 41%. The lowest overlap was recorded in WT and P23H rescue at 4% and 3% respectively. Distribution similarity between WT and P23H-resc can be detected from this platform. Moreover, P23A and P23H share relatively similar distribution.

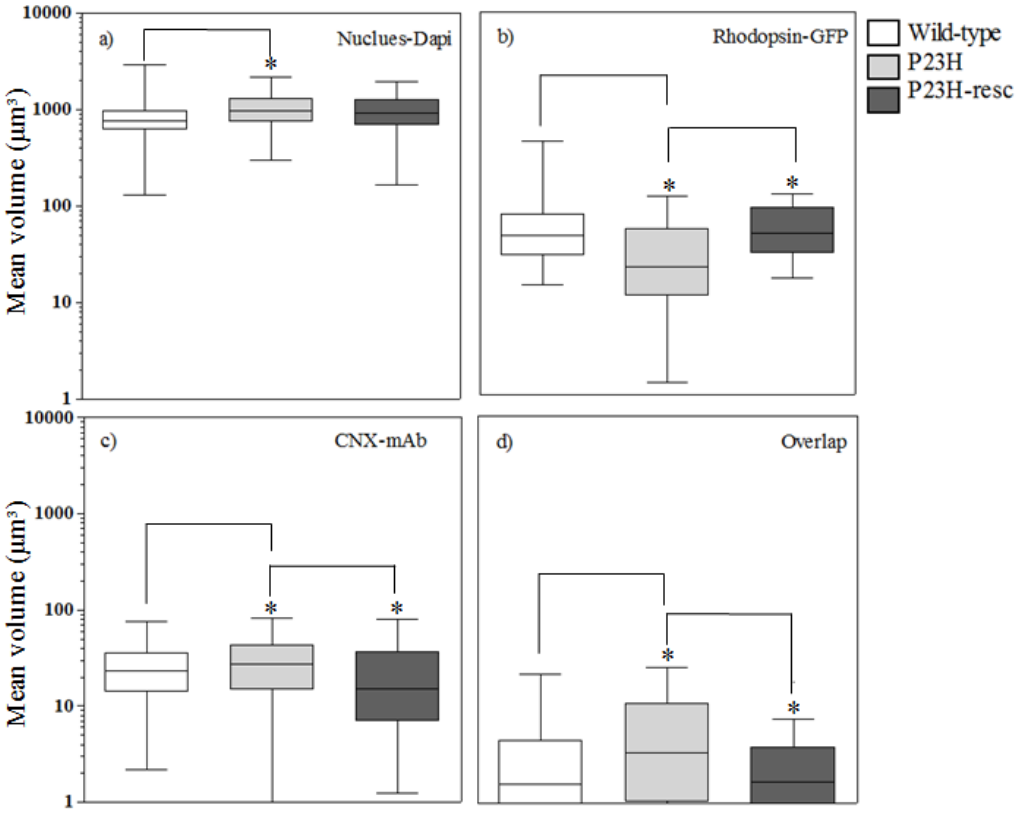

Figure III-9 Quantification of rhodopsin and CNX in rescued ADRP mutations in stable HEK293S cells.

Box plots (25–75 percentile) and whiskers (Tukey method) representing the distribution of the recorded cellular compartments over logarithmic scales. The bold line across the box represents the median for: a) Nucleus-DAPI (WT= 758 µm³, P23H= 971 µm³ and P23H-rec= 916 µm³), b) Rhodopsin-GFP (WT= 44 µm³, P23H= 21 µm³ and P23H-resc= 49 µm³), c) CNX-mAb WT= 23 µm³, P23H= 27 µm³ and P23H-resc= 15 µm³) and d) Overlap (WT= 1 µm³, P23H= 2 µm³ and P23H-resc= 1 µm³). Asterisks (*) denote statistical significance when the p-value is < 0.05 in comparison to WT and P23H.

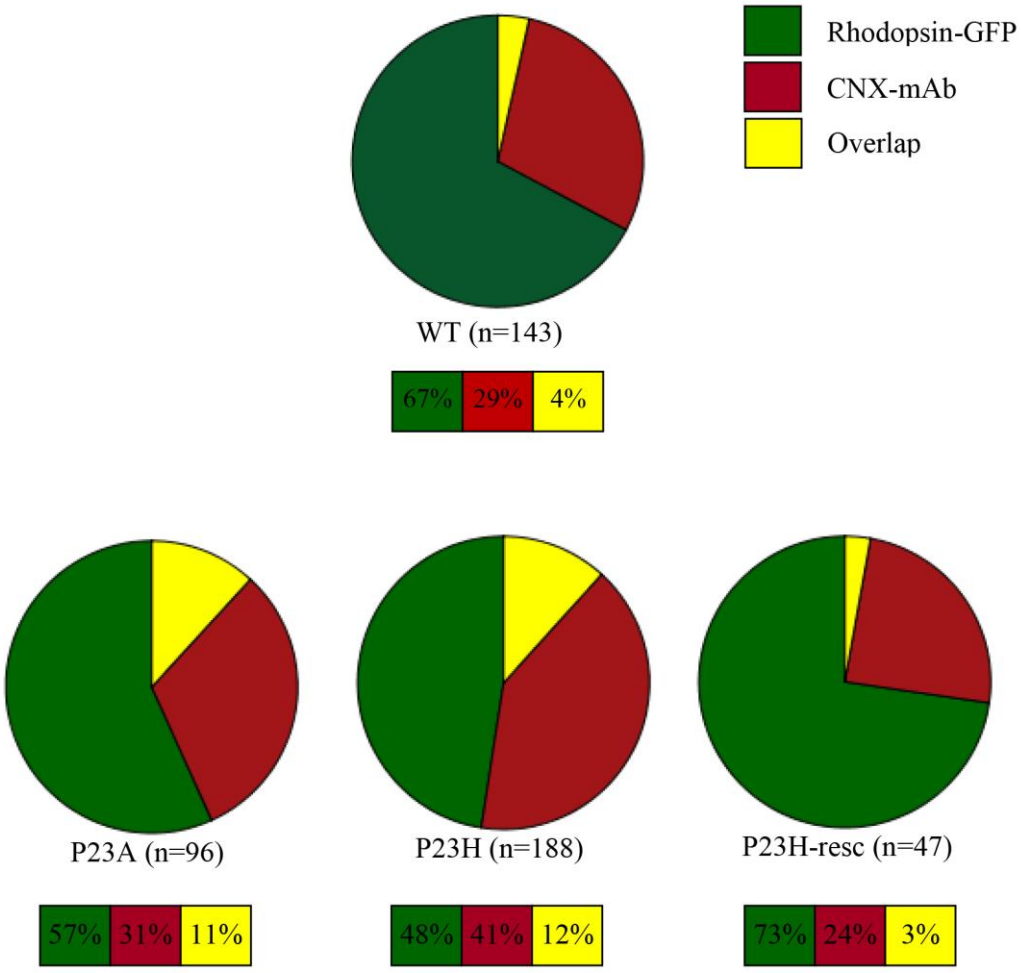

Figure III-10 Pie charts demonstrate volume percentages in ADRP cell model.

The slices depicted the percentage of rhodopsin-GFP, claneixn-mAb and their overlap in ADRP phenotypes in comparison to WT. P23H demonstrates the lowest percentage of rhodopsin-GFP at 48% and the highest percentage of CNX-mAb at 41%. The lowest overlap was recorded in WT and P23H rescue at 4%.

III.4 Discussion

III.4.1 Aggresomes formation and P23H rhodopsin mutation in ADRP

In transfected cells, class II rhodopsin mutations fail to translocate to the plasma membrane and accumulate within the cytoplasm in the ER and Golgi (Kaushal and Khorana, 1994; Sung *et al.*, 1993; Sung *et al.*, 1991b). By visual inspection we also reported an accumulation of rhodopsin mutants within the plasma membrane of the stable cell line. These accumulations suggest that rhodopsin-GFP proteins aggregate. With bioimaging alone, it is impossible to distinguish between inclusion bodies and aggresomes. However, such punctate particles in the cytoplasm have been previously classified as aggresomes (South, 2012), which is also in keeping with investigations on the nature of this particle (Saliba *et al.*, 2002). After both visual inspection and automated analysis of images, our results show an increase in the presence of aggresomes in P23H mutant cells. This supports what Illing *et al.* (2002) reported as they linked P23H mutation in ADRP with the formation of aggresomes in the cytoplasm of transfected cells. Moreover, we detect the presence of protein aggregation in the images of P23A mutant cell line. This defective protein is also like P23H, a product of mutation in the transmembrane, domain of rhodopsin, however the total number of the detected aggresomes in P23A are not significantly different from WT cells. This can be linked to the lack of severity of P23A in contrast to P23H (Oh *et al.*, 2000). While a feasible amount of rescued P23H rhodopsin was observed by visual inspection to be translocated to the plasma membrane, the presence of protein aggregate within the cytoplasm of P23H-resc is remarkably high. Suggested that the pharmacological rescue of those cell asset the folding and translocation of some of the mutant protein to the plasma membrane, however it did not resolve the question of the incidence of aggresome formation.

III.4.2 Rhodopsin-GFP levels in the stable transfected cell line

In our investigation we used a stable transfected cell line to facilitate the testing of our image quantification approach. The stable transfected cell line was reported to have a lower variation in rhodopsin expression and it provides a good study model for rhodopsin-GFP (Reeves *et al.,* 2002).

We reported a significantly higher rhodopsin volume in WT cells in comparison to P23H, a finding previously reported by Illing *et al.* (2002), and Opefi *et al.* (2013). Our record stated that the median volume of rhodopsin-GFP in P23H is about 23 μm^3 less than WT. Moreover, it was reported that, in stable transfected HEK293S cells, total opsin levels were ten-fold lower in P23H than in WT cells (Noorwez *et al.*, 2009). Although the methodology they used was Immunoprecipitation and western blot, the results we generated by image quantification didn't conflict with their finding.

Interestingly, P23A rhodopsin quantification recorded to be not significant compared to WT. Visual interpretation showed that P23A cells are like WT, expressing high levels of rhodopsin-GFP. Moreover, clinical data reported that P23A mutation is a less severe mutant than P23H (Oh *et al.,* 2000). Although at this point in our investigation we can't draw a direct correlation, other researchers have established a correlation between rhodopsin stability and the severity of retinitis pigmentosa (McKeone *et al.,* 2014), that suggested that the clinical severity of the mutation is linked to the level of rhodopsin production. Krebs *et al.* (2010) linked rhodopsin misfolding with the clinical severity of ADRP. They reported that P23A rhodopsin causes a moderate effect. Moreover, P23A was responded well to both

pharmacological chaperone rescue and cysteine pair treatment (Opefi *et al.*, 2013). That may explain why P23A mutant cells in our research were not defective in rhodopsin-GFP production.

III.4.1 Low image quality precludes robust quantification

Quantitative evaluation of image datasets is an essential method of obtaining quantitative data from fluorescent staining (Hamilton, 2009). Optimally stained samples subjected to the correct parameters for image acquisition are critical for reliable outcome. After implementing our standard workflow for image quantification (section II.2.11) on feasible and non-feasible images we reached the conclusion that not all acquired images can produce reliable quantitative results. In contrast to good quality images, the images of P23L and P23L-rescued showed insufficient contrast. The automated algorithm failed to quantify them. Compromised sample preparation or image acquisition parameters will produce bias and in many cases unreliable results.

III.4.2 Volumetry of CNX and its overlap with rhodopsin in ADRP model

CNX is a resident ER chaperone that safeguards the proper folding and quality control of newly synthesized glycoprotein (Hebert and Molinari, 2007). The importance of CNX is also reported in the maturation and stability of drosophila's Rh1 rhodopsin (Rosenbaum *et al.*, 2006). However, according to Kosmaoglou and Cheetham (2008) CNX does not have the same importance in mammalian rhodopsin maturation. Yet, there is no publication describing the exact nature of CNX

interaction with mutant rhodopsin. One report confirmed the localisation of P23H mutant with CNX in a transgenic mouse model (Frederick *et al.*, 2001). We investigated the significance of CNX volume comparing WT, P23A and P23H. Our attempt was the first to address cellular CNX volume using image quantification. We wanted to determine whether the expression of opsin affected CNX expression. However, we didn't find any significant difference in CNX-mAb volume between WT and P23A. In contrast, the difference between WT and P23H was statistically significant with the highest CNX-mAb volume in P23H. Interestingly, Noorwez *et al.* (2009) analyzed the levels of CNX in the cell lysates of a stable transfected cell line expressing WT and mutant rhodopsin, and reported that the cellular CNX levels did not show any considerable difference which could be related to rhodopsin expression. However they did find that 45-fold more CNX was associated with P23H than with WT. In our quantification, the detected overlap of CNX-mAb with rhodopsin-GFP in both P23A and P23H mutation was recorded to be significantly higher than WT. The overlap of mutant rhodopsin with the ER marker CNX indicates its functional ER import for mutant rhodopsin. This higher overlap can be related to CNX for its role in rhodopsin quality folding. In conclusion, the detected cellular level of detected CNX may be affected by the expression of rhodopsin. However, more investigation is needed to indicate if this dependency is linked to the different methodology used for CNX detection or if it is dependent on the cell line.

III.4.3 Volumetry of P23H mutants after pharmacological rescue with 11-*cis* retinal suggests restored folding of this mutant to resemble WT

Mutations within the N-terminal region, such as P23H, result in improper folding of opsin causing its failure to bind with its chromophore (Rattner *et al.*, 1999). In the case of pharmacological rescue for this mutation, adding 11-*cis*-retinal assists the folding of misfolded P23H leading to a 5-fold increase in rhodopsin levels (Noorwez *et al.*, 2009). After image quantification and evaluation of rescued P23H mutation. The rescued P23H mutant showed significantly higher volume of rhodopsin-GFP expression compared to the non-rescued P23H mutant. Although the exact mechanism of the rescued one is not explained by image analysis, we reasoned that the correct folding of rhodopsin is critically important for rhodopsin translocation into the cellular membrane as we observed in P23H rescued images. Moreover, Noorwez *et al.* (2009) and Opefi *et al.* (2013) reported that correct folding for P23H was achieved by 11-*cis*-retinal pharmacological rescue. Nevertheless, we believe that 11-*cis*-retinal provides rhodopsin with the right constitution to interact with CNX for better and complete folding. The lowest volume of CNX-mAb was registered with the rescued mutant with a significant difference between P23H mutant and the rescued one. That suggests that the cellular level of CNX may be affected by either the presence of 11-*cis*-retinal pharmacological rescue or by the correct folding of P23H mutant. Interestingly, when compared with the other literature, Noorwez *et al.* (2009) recorded a 3-fold reduction of CNX level when pharmacological rescue was added (Noorwez *et al.*, 2009).

Furthermore, the overlap of rhodopsin-GFP with CNX-mAb between P23H-resc and P23H was recorded to be significant but not between WT and P23H-resc. In

conclusion, by using our approach in image quantification we find that rescued mutant results are showing similarity to WT results. We can suggest that the presence of the pharmacological chaperone 11-*cis*-retinal improved the folding of the mutant rhodopsin and enhanced its translocation to the plasma membrane, as was proven before in (Noorwez *et al.*, 2009). In conclusion, the results of our image quantification do not contradict what has been reported in other literature.

III.4.4 Distribution of nucleus sizes

The nucleus is the largest organelle in most cells. In addition to housing the genetic information and serving as the site of DNA and RNA synthesis, transcription, and processing, it plays an important role in coordinating the intricate cellular architecture (Lee *et al.*, 2007). We wanted to evaluate the nuclear size distribution in different phenotypes as an 'internal control' for volumetric segmentation. Our hypothesis was that a sufficiently homogenous nucleus size could be used as a volumetric standard. This could then aid the detection of differences in segmentation that are due to image quality and not biologically meaningful volume changes, since differences in the signal-to-noise ratio can lead to the thresholding of different volumes, causing inaccuracies such as partial volume errors. However, variance between datasets acquired from the same batch of cells, the same phenotype, and using identical image acquisition parameters, was high, and statistically significant differences were found between phenotypes. In some cell types, nuclear size correlates with the ratio of RNA:DNA, expression of ribosomal genes,and general transcription rate. In addition, the nuclear size in budding yeast appears to be determined by cell volume and not by the amount of DNA (Levy and Heald, 2012). However, it was not possible to state if

the statistically significant differences are biologically relevant without extensive additional experimentation. We concluded that DAPI-stained nuclei cannot be used as a sensitive internal control for thresholding quality without further testing. However, assessment of nuclear volumes can be used to show up gross errors in calibration or thresholding, identify datasets with a low nuclear signal that may point to poor contrast in other channels, or reveal outliers such as giant cells which can then be excluded from analysis.

III.4.5Karyoplasmic ratio in HEK293S cells

Although the stable transfected HEK293S cell line had been considered a good model for studying ADRP, the morphology of this cell line is not satisfactory for highlighting the high production of rhodopsin-GFP expression. HEK293S in our study possesses a large nucleus size in comparison to the cytoplasmic area as shown in Figure III-11. This karyoplasmic ratio is maintained at a constant value within a specific cell type (Levy and Heald, 2012). Classic transplantation experiments support the cytoplasmic area is the location where mutant rhodopsin is retained. Taking this into or consideration, we will thus in the next chapter look at the possibilities of a transiently transfected cell line with a decent endomembrane area. This will also help us to detect rhodopsin mutant phenotypic manifestation within another cellular model.

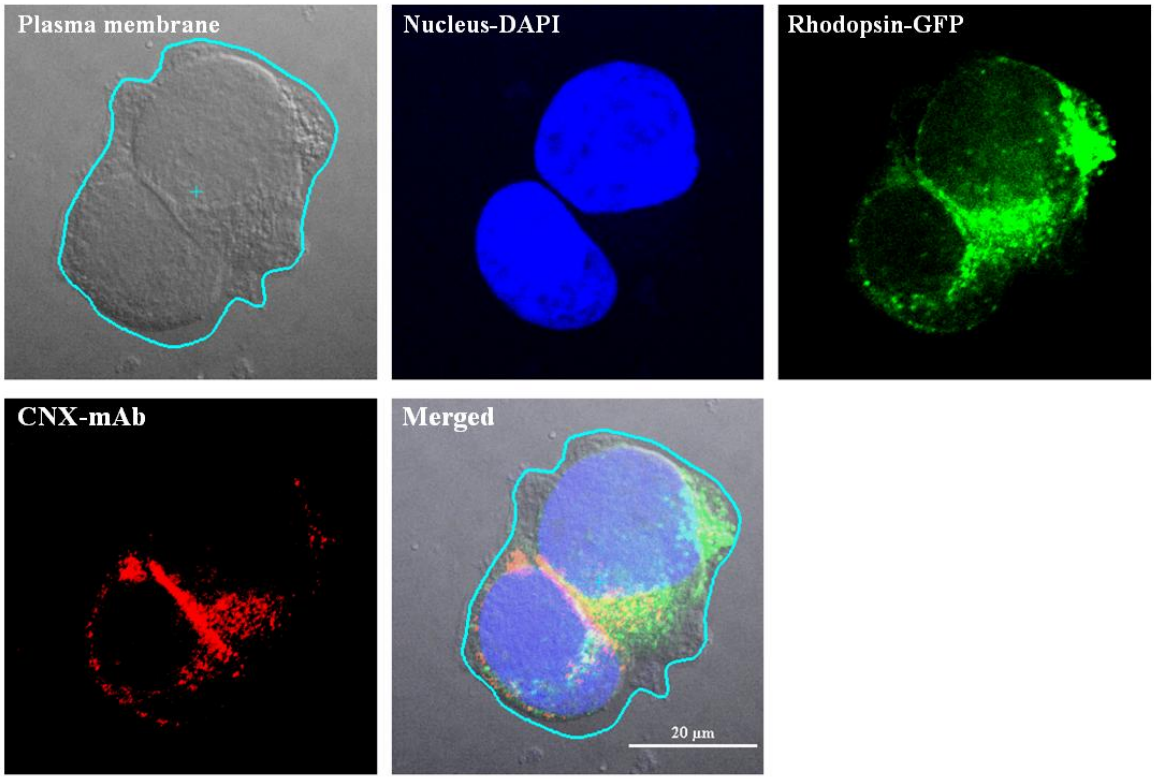

Figure III-11 Threshold segmentation of stable HEK293S cells.

The cells are expressing P23H rhodopsin-GFP and labelled with CNX-mAb. The representative images show the proportion of nucleus size in comparison to the cytoplAsmic area which is enclosed inside the cyan line (plasma membrane).

Chapter IV: Co-expression of the ER resident chaperone calnexin with rhodopsin mutants in GMK cells

IV.1 Introduction

Essential cellular operations are controlled by the endoplasmic Reticulum (ER). This highly specialized organelle which is the home for the synthesis and folding of secreted membrane-bound and some organelle-targeted proteins (Hebert and Molinari, 2007). The process of protein organization within the rough ER is facilitated by a series of molecular chaperones which play key roles in the assistance of protein folding and assembly, stabilization of unfolded proteins, unfolding of proteins for translocation across membranes, or for degradation (Guérin et al., 2008). The quality control mechanism for N-glycoproteins (such as rhodopsin) is through the calnexin-calreticulin cycle. The ER chaperone calnexin (CNX) plays a key role in the translocation of nascent polypeptides and in the folding and quality control of newly synthesized proteins. Structurally, CNX is an ER transmembrane protein, consisting of a big lumenal domain, a transmembrane domain (TM), and a short cytosolic tail as shown in Figure IV-1. The lumenal domain of CNX interacts with client proteins in a glycan-lectin manner or via protein–protein interactions (Guérin et al., 2008). CNX is responsible for the accurate folding of glycoproteins and for the retention of unfolded or misfolded glycoproteins in the ER, and additionally plays a key role in the degradation of misfolded proteins (Illing *et al.*, 2002). Rhodopsin is a G protein-coupled receptor that forms the visual photo pigment when coupled with 11-*cis*-retinal (Rattner et al., 1999). To deal with continuous rhodopsin production throughout life, the ER of photoreceptor cells must be robustly optimized towards folding rhodopsin as well as recognizing and removing any misfolded rhodopsin. However, in cell culture, many rhodopsin mutants misfold and aggregate to trigger ER stress and activate the unfolded protein response (Illing *et al.*, 2002; Lin *et al.*, 2007).

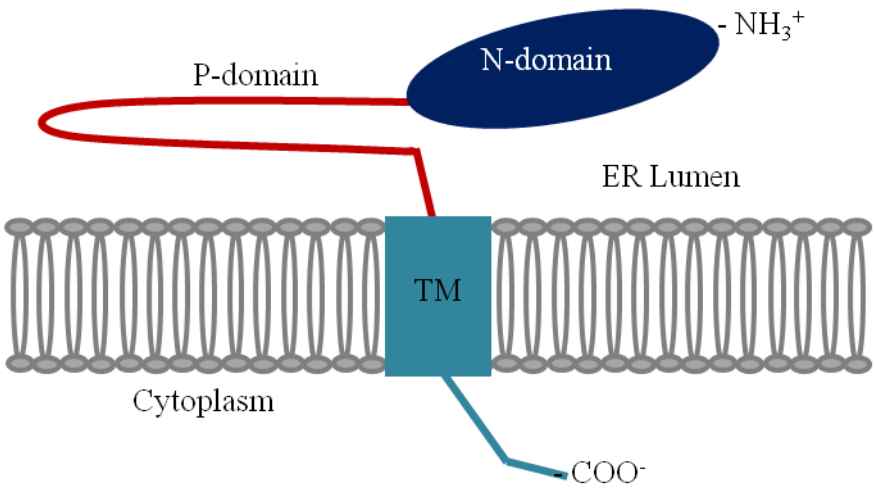

Figure IV-1 Schematic representation of calnexin (CNX) domains.

Calnexin is an ER transmembrane protein, with a large luminal domain, a transmembrane domain (TM), and a short cytosolic tail.

The role of UPR activation in photoreceptor cell death remains unclear (Chiang *et al.*, 2015). Moreover, Chiang *et al.* (2015) reported that the small amount of P23H rhodopsin that exits the ER and bypasses ERAD exerts a cytotoxic effect on photoreceptor cells.

Here we investigate the interaction and localisation of rhodopsin phenotypes using CNX in the GMK cells. In this study we used automated image quantification which we have validated in our previous chapter. However, instead of the antibody labelling of CNX in stable transfect cells, we transiently transfect rhodopsin-GFP (WT/P23A/P23H/P23L) and mCherry-CNX in the GMK cells due to their karyocytoplasmic ratio.

IV.2 Experimental procedures and statistical analysis

IV.2.1 GMK cells co-transfection, fixation and image acquisition

GMK cells were grown in DMEM supplemented with 10 % FBS, 1 % penicillin/streptomycin and 1 % l-glutamine. 24 hrs before co-transfection, a 80-90 monolayer confluence was reached. Cells were detached from the flask with trypsin. 3 x 10^4 cells were seeded on round 13 mm glass coverslips (VWR,USA) in 1 ml antibiotic free media supplemented with 10 % FBS in a 24-well plate. Cells were transfected using TurboFect (section II.2.6.5). 1 µg of the DNA of one of the rhodopsin phenotypes (one phenotype for each transfection) was mixed with 1 µg of mCherry-Calnexin-N-14 in 2 µl TurboFect and 100 µl serum-free, antibiotic- free medium and incubated for 15 min at room temperature. This mixture was then added to the cells. The cells were incubated for 24 hrs after co-transfection. The growth medium was removed, cells on the coverslips were fixed with 3.7 % cold

formaldehyde for 15 minutes, then washed three times with 1 % of cold PBS, the glass coverslips were mounted onto glass slides in (Vectashield) hard setting DAPI mounting media.

Images were acquired using a Nikon A1si confocal microscope with a plan-apochromatic VC1.4 N.A. 60 x magnifying oil-immersion objective lens. The software used for image acquisition was NIS-Elements AR 4.13.01 (Build 916). Images were acquired in four channels, using one-way sequential line scans. DAPI was excited at 400 nm and its emission collected at 450/50 nm. GFP was excited at 488 nm, its emission collected at 525/50 nm. mCherry signal was excited at 560 nm and collected at 595/50 nm. Scan speed was ¼ frames/s (galvano scanner). The pinhole size was 34.5 µm, approximating 1.2 times the Airy disk size of the 1.4 N.A. objective at 525 nm. Scanner zoom was centered on the optical axis and set to a lateral magnification of 60 nm/pixel, following the Nyquist–Shannon reconstruction theorem (Nyquist, 1928; Shannon, 1949). Axial step size was 105 nm, with 80-100 image planes per z-stack. Identical settings were used for all acquired datasets to allow for comparison.

IV.2.2 Image pre-processing and automated quantification

Nikon NIS-Elements; 64bit 3.21.03, Build 705 was used for image pre-processing as described in the Methods and Materials (section II.2.11). The acquired channels were assigned the following names; the blue (DAPI) channel representing the nucleus ‘nucleus-DAPI’, the green (EGFP) channel representing ‘rhodopsin-GFP’ and the mCherry red channel representing mCherry-CNX. Finally, a MATLAB routine for automated quantification of each single cell was achieved to determine the volume of

each channel in μm^3. Statistical analysis and graphing were performed based on the obtained quantification values.

IV.2.3 Time-lapse imaging for co-transfected GMK cells

GMK cells where grown in DMEM supplemented with 10 % FBS, 1 % penicillin/streptomycin and 1 % l-glutamine. 24 hrs before co-transfection, 80-90 monolayer confluence was reached. Cells were detached from the flask with TrypLE™. 2 x 10^4 cells were seeded on an ibidi u-Slide 8 wells chamber plate (80826, ibidi GmbH, Munich, Germany) and kept overnight inside the tissue culture unit incubator at 37 °C, 5 % CO_2. Cells then were co-transfected as mention previously in IV.2.1 and incubated for a further 24 hrs after co-transfection. In order to enhance the fluorescent signal during time-lapse imaging, old growth media with the transfection reagent residue was removed and replaced with an appropriate amount of FluoroBrite™ DMEM. Moreover, to preserve GMK cells' health during imaging, FluoroBrite™ DMEM was supplemented with 10 % FBS and 1 % l-glutamine.

Live cell imaging was performed at 37 ^oC in 5 % CO_2 electric top stage microscope incubator (Model: H301,OkoLab, Italy). Multi-location time-lapse images were taken by automated wide-field microscopy (Eclipse Ti; Nikon) using a 60× 1.49 NA oil objective lens. Two-dimensional time series frames were acquired with an Andor camera (Model: Luca-R DL-626, *Andor* Technology, UK) at the rate of one an hour throughout 24 hours. The software used for image acquisition was NIS-Elements AR 4.13.04 (Build 925).

Fluorescent signals were excited using the CoolLED pE excitation system (CoolLED, UK). Rhodopsin-GFP was illuminated at 470 nm wavelength and imaged with a FITC filter (Nikon, Japan). The red signal from mCherry-CNX was excited at 585 nm wavelength and imaged with a Semrock BrightLine m-Cherry b-nte-zero filter (Semrock, USA).

IV.2.4 Quantitative fluorescence intensity measurements

Nikon NIS-Elements; 64 bit 3.21.03, Build 705 was used for image pre-processing and analysis as mentioned in the Methods section II.2.11. The acquired channels were assigned the following names; the green (GFP) channel representing 'rhodopsin-GFP' and the (mCherry) red channel representing mCherry-CNX.

All datasets were deconvolved using AutoQuant X (version 2.2.1, Media Cybernetics, Inc., Bethesda, MD, USA) which is based on a combination of blind deconvolution (Ayers and Dainty, 1988; Holmes *et al.*, 2006) and maximum likelihood estimation (Holmes, 1988; Holmes *et al.*, 1995). Furthermore, quantitative fluorescence intensity changes were recorded with a time measurement tool which calculates automatically the average pixel intensities within the relevant fluorescent areas during specific time intervals. The obtained fluorescence intensity values were extracted for statistical analysis and graphing.

IV.2.5 Statistical analysis

Data generated by automated quantification and time measurements were imported to SPSS software for statistical analysis. Detection of data outliers was done simultaneously with the visual inspection of the cells. A nonparametric test for

independent samples (Kruskal-Wallis) was used to compare the means of different data. Furthermore, Dunn's nonparametric pairwise multiple comparisons test was used to test the significance between different phenotypes. In all cases, a p-value of $\leq$ 0.05 was considered to be significant. Star symbols were used to indicate statistical significance (* $p \leq 0.05$). All graphing was performed using the graphing and statistical software GraphPad Prism 7.

Box plots represent 25–75 percentiles and whiskers were assigned using the Tukey method. Average fluorescence intensity (a.u) was plotted against acquisition time (h) in a line-chart.

IV.3 Results

IV.3.1 Sample size

A total of 150 fixed cells were included in both visual interpretation and statistical analysis (WT) n= 45, P23A n= 38, P23H n=32, P23L n=35). For live imaging a total of 18 cells were selected (WT n= 5, P23A n= 3, P23H n=6, P23L n=4).

IV.3.2 Visual interpretation of rhodopsin-GFP expression and colocalisation with mCherry-CNX

Figure IV-2 shows GMK cell lines after co-transfection with mCherry-CNX and differing rhodopsin-GFP phenotypes. In WT cells, the rhodopsin-GFP signal extended to the plasma membrane with poor overlap with mCherry-CNX as shown in Figure IV-2.b. In the case of P23A, rhodopsin-GFP was detected on the plasma membrane, while some overlapped with CNX in the cytosol (Figure IV-2.c). Rhodopsin-GFP in both P23H and P23L is retained within the cytosol, showing higher overlap with

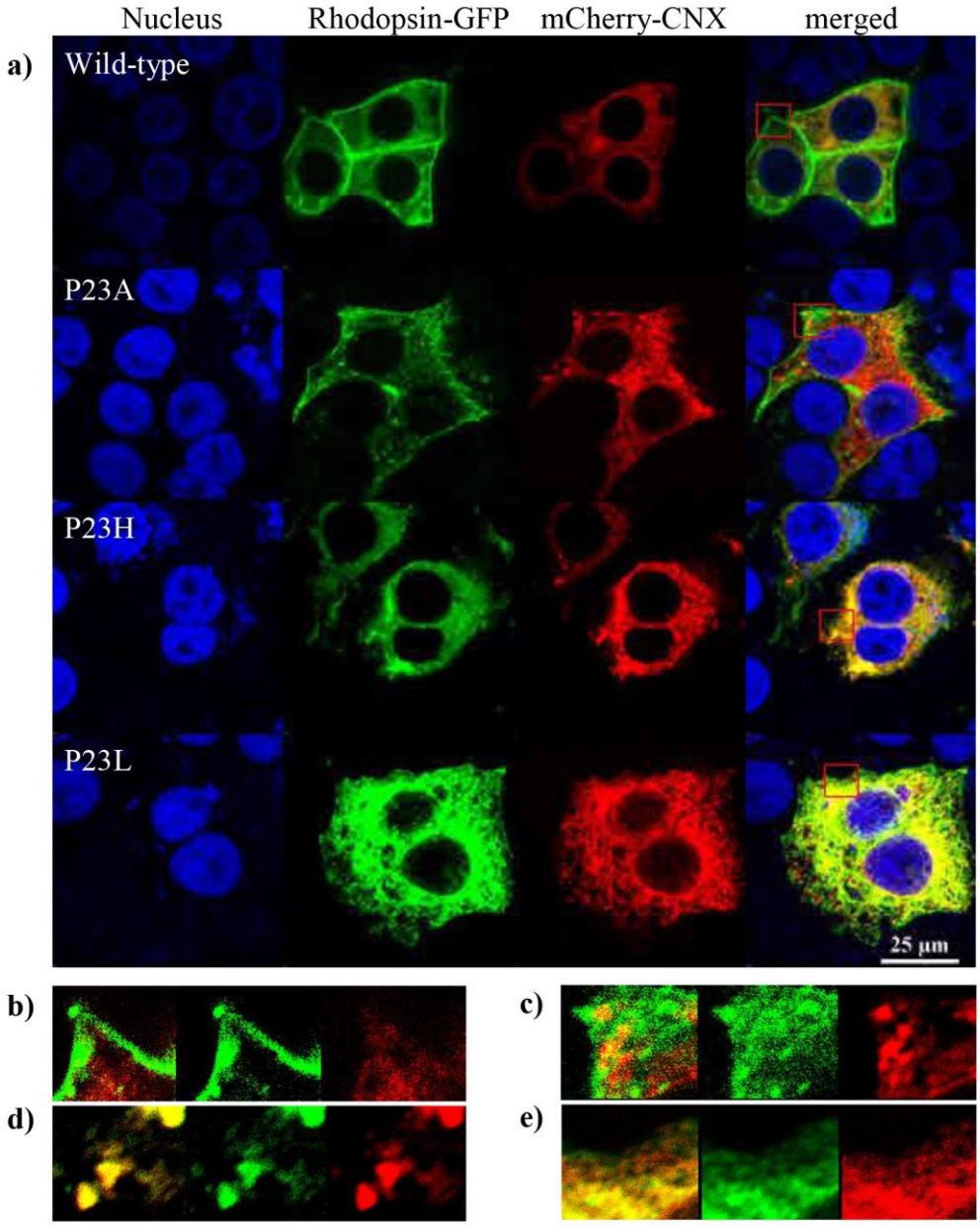

Figure IV-2 Maximum intensity projection showing the localisation of rhodopsin-GFP and mCherry-CNX in GMK cells.

a) Strong localisation of rhodopsin-GFP within the plasma membrane is recorded in WT cells. P23A demonstrates slightly low plasma membrane localisation. Both P23H and P23L show a low level of rhodopsin-GFP expression in the plasma membrane. Nuclei are stained with DAPI. Closeups (50x) of the regions highlighted by the red squares can be seen at the bottom. The overlap of rhodopsin-GFP with mCherry-CNX was demonstrated on segmented images. b) WT shows no significant overlap with CNX. c) P23A shows a minor overlap with CNX. On the other hand, strong localisation with CNX was observed in d) P23H and e) P23L.

calnexin, as well as poor plasma membrane localization, compared to P23A and WT, as shown Figure IV-2 (d) and (e) respectively.

IV.3.3 Nucleus volume distribution

The box and whiskers plot in Figure IV-3 summarises the distribution of nucleus-DAPI volume across phenotypes. The highest median for nucleus volume was observed in WT cells followed by P23H, P23A and P23L at 2120 μm^3, 2064 μm^3, 1558 μm^3, and 1485 μm^3 respectively. Moreover, we found a statistically significant difference between WT cells and both P23A,and P23L with $p<0.05$ for nucleus-DAPI volume.

IV.3.4 Quantification of live-cell rhodopsin-GFP phenotypes

The box and whiskers plot in Figure IV-4 represents the distribution of rhodopsin-GFP volume in the GMK cell line. The highest median for rhodopsin-GFP volume was observed in WT cell: 193 μm^3, followed by P23A 120 μm^3, P23L 114 μm^3 and P23H at 79 μm^3. Furthermore, we found a statistically significant difference for rhodopsin-GFP between WT cells and P23H where $p<0.05$.

Similar significance was observed when comparing the mean of rhodopsin-GFP volumes within WT cells and P23L. In contrast, no statistical significance was recorded between WT and P23A.

IV.3.5 Quantification of mCherry-CNX Volume

The box and whiskers plot in Figure IV-5 demonstrates the significance of the mean mCherry-CNX volume across phenotypes. Statistically significant differences were

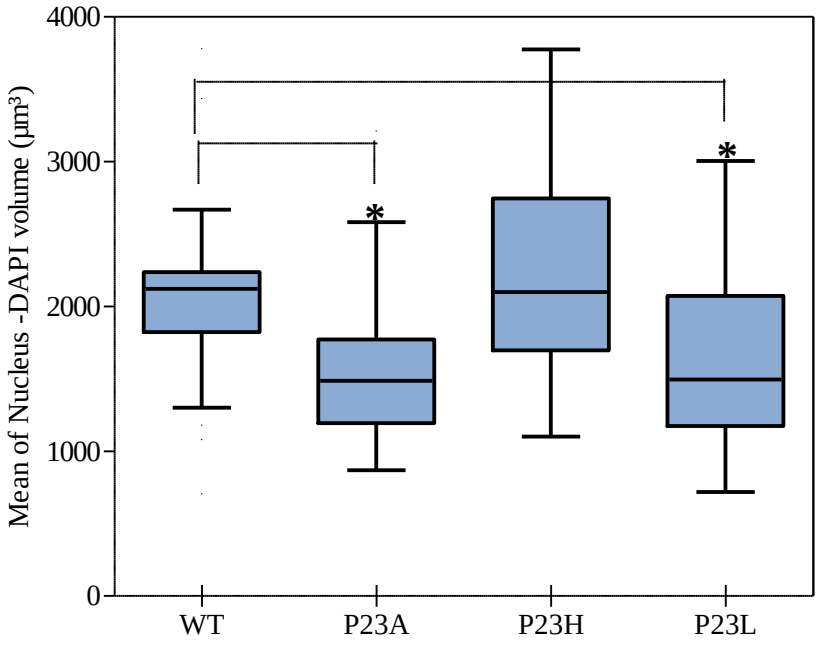

Figure IV-3 Nucleus-DAPI volume distribution after co-transfection

The boxes in the plot represent the middle half of the distribution of nucleus-DAPI volume in GMK cells, stretching from the 25th percentile to the 75th percentile. The bold line across the box represents the median (2120 µm³, 2064 µm³, 1558 µm³, and 1495 µm³) for WT, P23H, P23A and P23l respectively. The lengths of the lines above and below the box define the maximum and minimum nucleus-DAPI volume in µm³. Asterisks (*) denote $p < 0.05$ in comparison to WT.

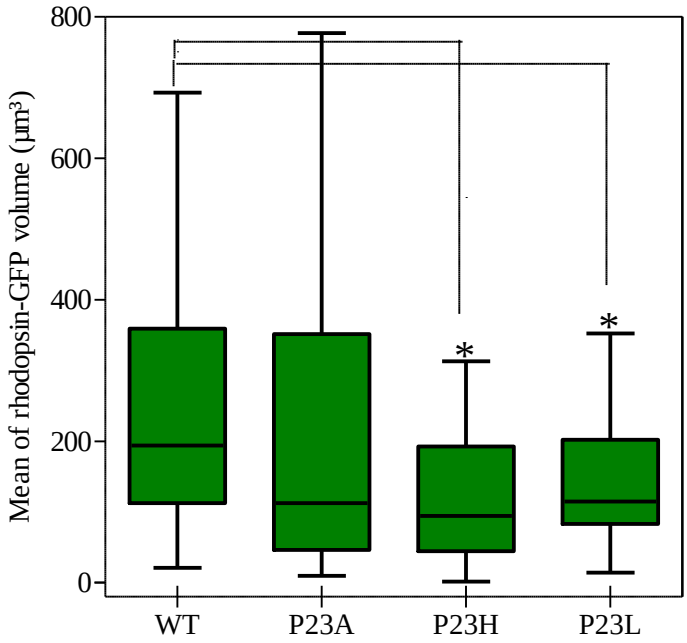

Figure IV-4 Rhodopsin-GFP volume distribution in co-transfected GMK cell line

The boxes in the plot represent the middle half of the distribution of rhodopsin-GFP volume, stretching from the 25th percentile to the 75th percentile. The bold line across the box represents the median (193 µm³, 120 µm³, 114 µm³, and 79 µm³) for WT, P23A, P23L and P23H respectively. The lengths of the lines above and below the box define the maximum and minimum rhodopsin-GFP volume in µm³. Asterisks (*) denote $p < 0.05$ in comparison to WT.

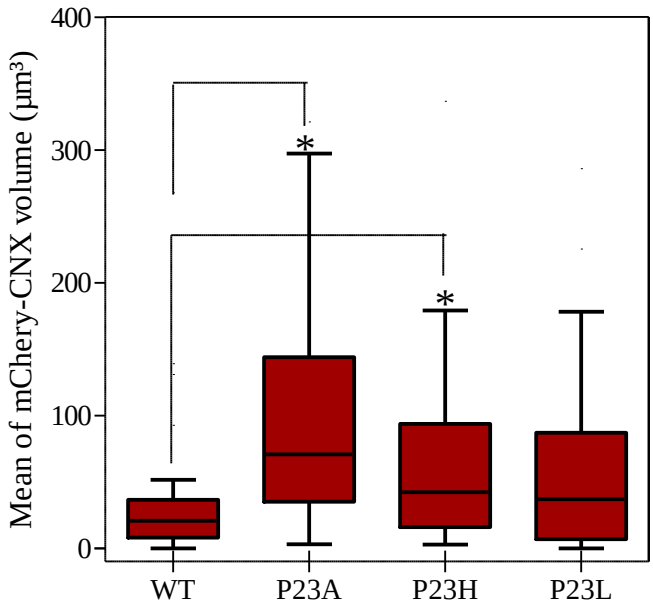

Figure IV-5 Volume distribution of mCherry-CNX in GMK cells

Box plots (25–75 percentile) and whiskers (Tukey method) showing comparisons of the distribution of mCherry-CNX volume. The bold line across the box represents the median (68 µm³, 45 µm³, 36 µm³ and 20 µm³) for P23A, P23H, P23L and WT respectively. Asterisks (*) denote $p < 0.05$ in comparison to WT.

detected between wild-type and both P23A and P23H with $p<0.05$. No statistical significance was recorded between WT and P23L. The highest median for mCherry-CNX volume observed in P23A followed by P23H, P23L and WT at 68 μm^3, 45 μm^3, 36 μm^3, and 20 μm^3 respectively.

IV.3.6 Quantification of the overlap of rhodopsin-GFP and mCherry-CNX after co-expression

The overlap volumes of rhodopsin-GFP and mCherry-CNX after their co-expression in GMK cells are illustrated is the box and whiskers plot in Figure IV-6. The highest median for the overlap volume is observed in P23L at 6 μm^3, followed by P23H with 3 μm^3 and P23A with 1 μm^3. WT cells showed an extremely low volume (less than 1 μm^3). Furthermore, statistically significant differences were detected between WT and both P23A and P23H with $p<0.05$. However, no statistical significance was recorded between WT and P23L.

IV.3.7 Visual interpretation of 2D time-lapse images after their co-transfection with rhodopsin-GFP and mCherry-CNX

Time-lapse images for GMK cells which were co-transfected with WT rhodopsin-GFP and mCherry-CNX are displayed in Figure IV-7. During the first hour of imaging rhodopsin-GFP signals were detected in the plasma membrane. A small amount of rhodopsin-GFP was occupying the same area as mCherry-CNX. However, after 12 hours of imaging the amount of rhodopsin localising with CNX increases gradually with heightened expression of the mCherry fluorescent signal. Moreover the

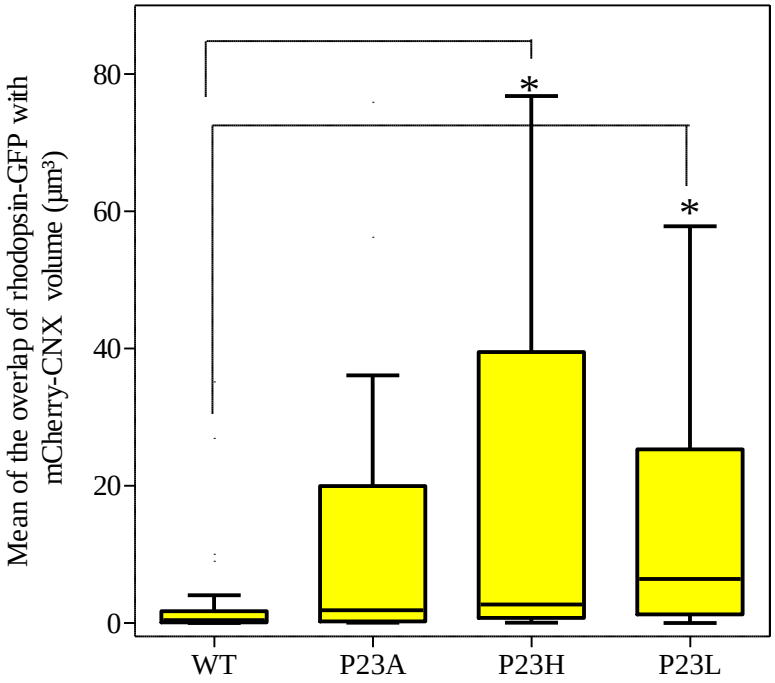

Figure IV-6 The volume distribution of rhodopsin-GFP overlapping with mCherry-CNX in the co-transfected GMK cell line

Box plots (25–75 percentile) and whiskers (Tukey method), represent the middle half of the volume distribution for the overlap of rhodopsin-GFP with mCherry-CNX. The bold line across the box represents the median (0.9 µm³, 1 µm³, 3 µm³ and 6 µm³) for WT, P23A, P23H and P23L respectively. Asterisks (*) denote $p < 0.05$ in comparison to WT.

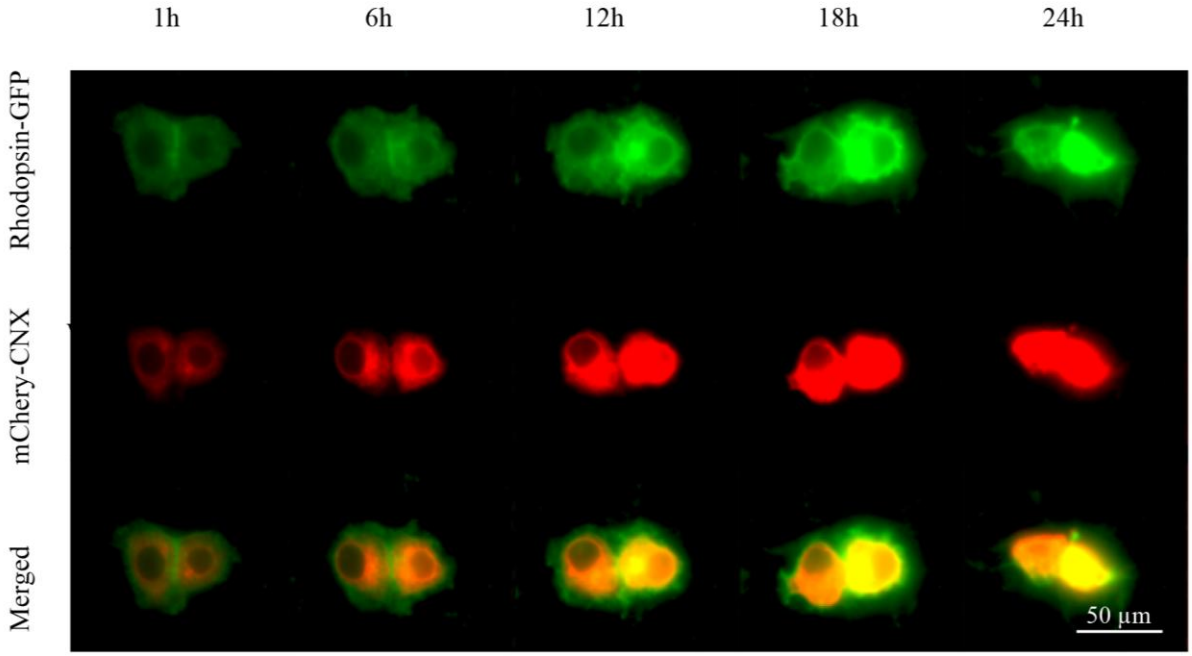

Figure IV-7 Live imaging of GMK cells co-expressing WT rhodopsin-GFP and mCherry-CNX.

A two-dimensional real-time series imaged using widefield epifluorescence for up to 24 h. The time points are given as hours (h), with the first image shown taken after 24 h post co-transfection. Rhodopsin-GFP signals were concentrated in the plasma membrane with a small amount of rhodopsin-GFP occupying the same area as mCherry-CNX (1h). After 12 hours of imaging the amount of rhodopsin localising with CNX start to increases gradually with heightened expression of the fluorescent signal. The cells start to become round and to lose their structural integrity. Cells appear to die between 18-24h.

cells started to lose their structural integrity and change their morphology to rounded cells. At the end of a time course of 24h hours of imaging, cells were dead. Cells co-expressing P23A rhodopsin-GFP and mCherry-CNX are shown in Figure IV-8. On the first time frame (1h), part of the rhodopsin-GFPsignal was detected on the plasma membrane. We also detect cytoplasmic clumps of rhodopsin localising with CNX. Rhodopsin signal on the cell membrane start to fade and concentrated more at the ER region with CNX after 12 hours.

CNX expression increases gradually during the time frames. The cells started to shrink and died some time before the end of the imaging between 12-24h. Time lapse images for GMK cells co-expressing mCherry-CNX and P23H and P23L rhodopsin-GFP and are displayed in Figure IV-9 and Figure IV-10 respectively. Contrary to WT, the rhodopsin-GFP signals in both mutants was found in the ER, colocalising with CNX from the first time frame (1h). Moreover, the cells start to become round after 6h for P23H and 12h for P23L. Cellular death was recorded for P23H after 12h, for P23L after 18h.

IV.3.8 Real-time quantification of rhodopsin-GFP and mCherry-CNX intensities

Representative time versus (rhodopsin-GFP and mCherry-CNX intensity) in live cells are demonstrated in Figure IV-11. The obtained fluorescence intensity values were corrected by subtracting the background noise, and plotted as arbitrary units (a.u). The time-lapse measurements for wild-type reveals that rhodopsin and CNX intensities do not show a high increase over time. Rhodopsin intensity recorded between 1500 and 2000 a.u. and CNX between 1000 and 1200 a.u.

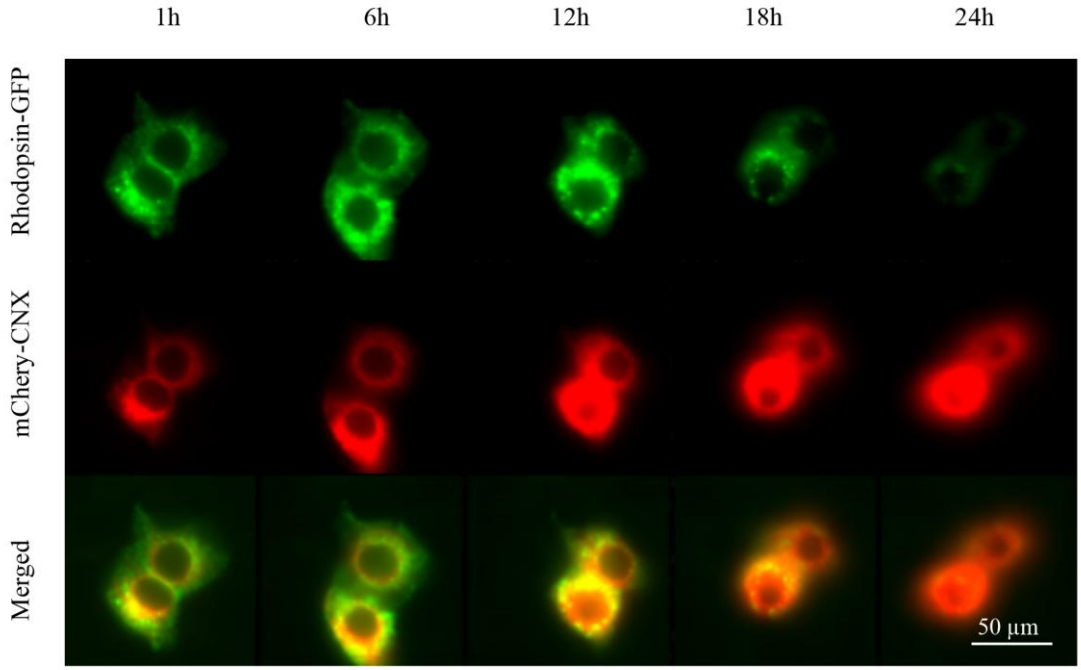

Figure IV-8 Live imaging of GMK cells co-expressing P23A rhodopsin-GFP and mCherry-CNX.

A two-dimensional real-time series imaged with widefield epifluorescence for up to 24 h. The time points are given as hours (h), with the first image shown taken after 24 h post co-transfection. The rhodopsin-GFP signal was concentrated between the plasma membrane and the ER (mCherry-CNX) (1h). After 12 hours of imaging the amount of rhodopsin localising with CNX started to increase gradually with heightened expression of the fluorescent signal. The cells started to become round and lose their structural integrity. Cells appear to die between 12-18h.

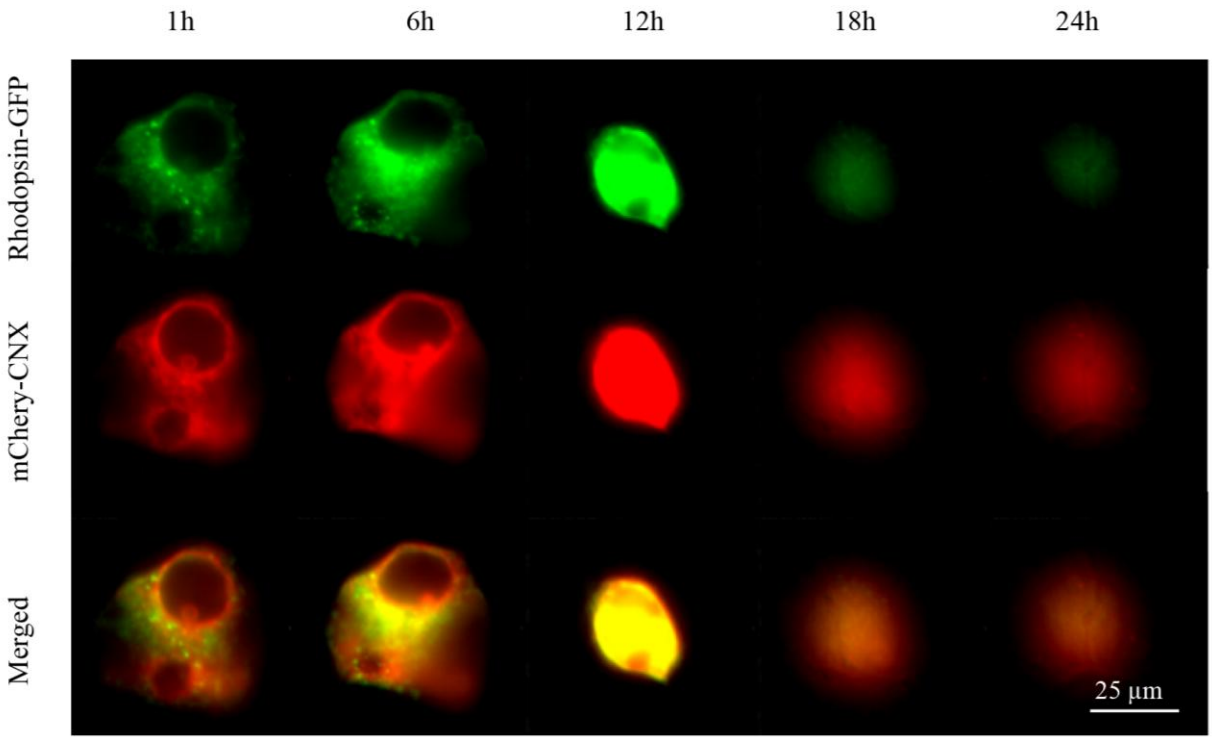

Figure IV-9 Live imaging of GMK cells co-expressing P23H rhodopsin-GFP and mCherry-CNX.

Two-dimensional real-time series imaged using widefield epifluorescence over 24 hours. The time points are given at 6 hour (h) intervals, with the first image shown taken 24 h post co-transfection. The rhodopsin-GFP signal is concentrated on the ER with mCherry-CNX (1h). After 6 hours of imaging the amount of rhodopsin localising with CNX starts to increase gradually with a high expression of the fluorescent signal. The cells start to become round and lose their structural integrity. Cells appear to die between 6-12h.

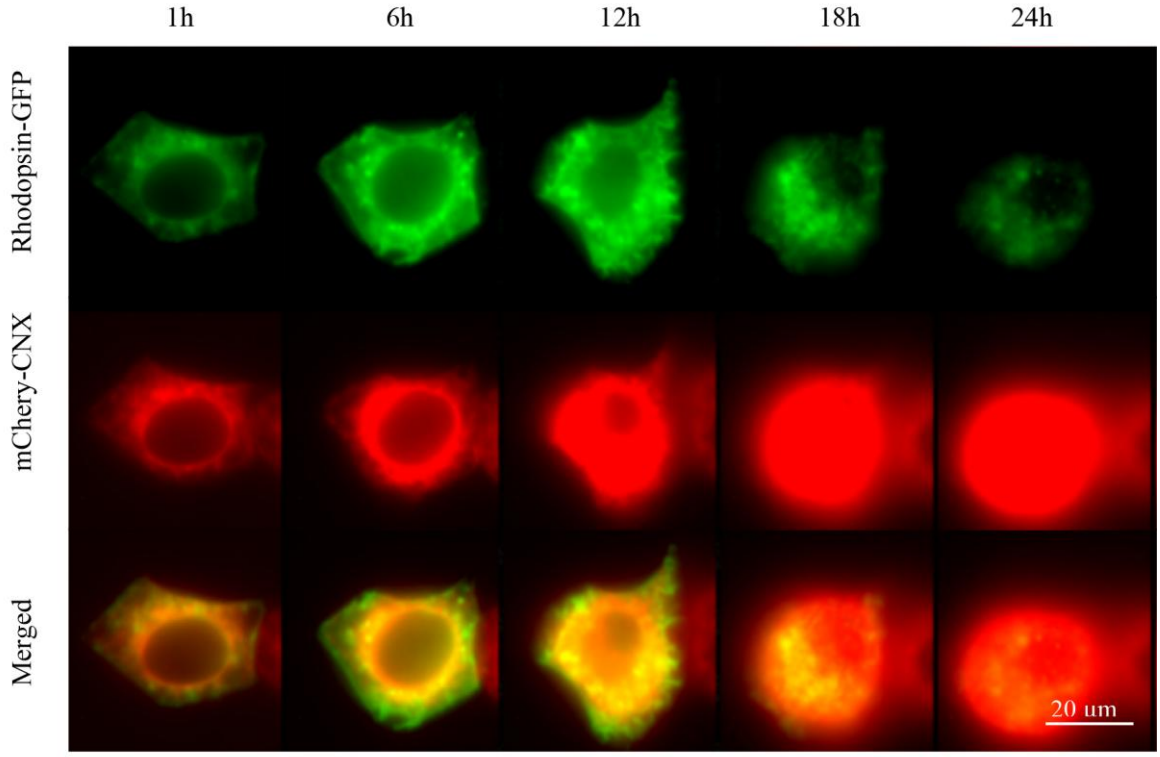

Figure IV-10 Live imaging of GMK cells co-expressing P23L rhodopsin-GFP and mCherry-CNX.

Two-dimensional real-time series imaged using widefield epifluorescence over 24 hours. The time points are given at 6 hour (h) intervals, with the first image shown having been taken 24 h post co-transfection. The rhodopsin-GFP signal was first concentrated on the ER with mCherry-CNX (1h). After 12 hours of imaging the amount of rhodopsin localising with CNX starts to increase gradually with a heightened expression of the fluorescent signal. The cells start to become round and lose their structural integrity. Cells appear to die between 12-18h.

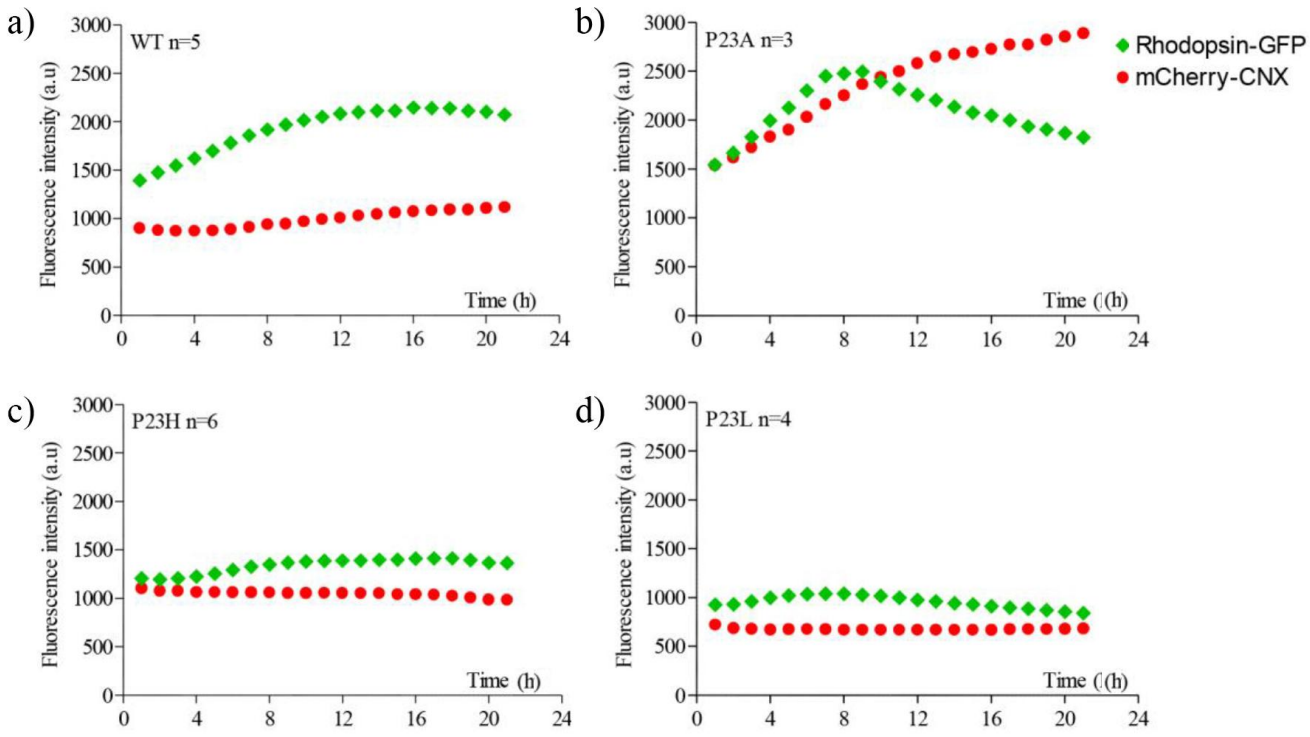

Figure IV-11 Real-time quantification of rhodopsin-GFP and mCherry-CNX intensities in GMK cell line.

a) Rhodopsin and CNX signals in WT cells steadily increase over time. b) Both signals in P23A gradually increase over time however CNX reached a peak at 3000 a.u after 20 hours meanwhile rhodopsin declined. c) For P23H Both signals during the first 8 hours increased, then reached a plateau between 1500 and 1000 a.u. d) P23Lwhich recorded the lowest rhodopsin and CNX intensity over time between 1000 and 5000 a.u.

To the contrary, P23A rhodopsin gradually increases and reaches a peak (around 2000 a.u) after 10h then decline, interestingly CNX share the same pattern with rhodopsin. CNX increases after 10h to reach it peak (around 3000 a.u) after 24h. P23H and P23L recorded with relatively same intensity for rhodopsin and CNX with slow increase in both signals during the first 8 hours then reached a plateau between 1500 and 1000 a.u for P23H and between 1000 and 5000 a.u for P23L. Moreover, P23L demonstrates the lowest rhodopsin and CNX intensity over time.

IV.4 Discussion

IV.4.1 The GMK cell line as a study model for ADRP

In this chapter we used the GMK cell line instead of HEK293S. The GMK cell line represents a well-characterized, immortalized line of African green monkey kidney (GMK) cells. The GMK cell line is susceptible to a broad range of viruses and used widely in the preparation of live and inactivated virus vaccines (Teferedegne *et al.*, 2014). This cell line has a large cytoplasm area which facilitates the observation and quantification of wild-type and mutant rhodopsin in fixed and live cells. Furthermore wide discrepancies between immunofluorescent staining and fluorescent protein tagging have been reported recently for around 20% from a large database (Stadler *et al.*, 2013). We used a mCherry-CNX construct to label the ER. As there is no published report addressing WT and mutant rhodopsin in the GMK cell line we will discuss this chapter's results against the background of the stable ADRP HEK cell line's results from chapter III. We will also investigate if the amounts of labelled CNX deliver similar results over either of those two techniques (immunostaining and transient transfection).

IV.4.1.1 P23A Rhodopsin is on the threshold between mutation and WT

Co-expression of rhodopsin-GFP and mCherry-CNX in GMK gives distinct phenotypical differences between WT and the investigated mutants.

The volume of P23A rhodopsin-GFP in GMK did not differ from that seen in WT. Interestingly, P23A rhodopsin in HEK293S was also reported to be similar to that found in WT. However, GMK cells expressing WT rhodopsin give the lowest CNX volume, whilst in P23A rhodopsin cells CNX is present in significantly higher volumes than in WT. Compared with our previous statistical significant test from Chapter III, we see that the P23A results differ from this Chapter's results only in regards to CNX volume and its overlap with rhodopsin. In HEK293 cells the CNX volume detected P23A via immunostaining does not show any significant differences to that found in WT although the overlap does differ.

In general, P23A in both cell lines demonstrate a resemblance to WT on both visual inspection and occasionally with quantification.

IV.4.1.2 P23H and P23L manifestation in GMK and HEK293 cell lines

The P23H mutation of rhodopsin belongs to a class (Class IIa) that is retained in the ER and is later translocated to the cytoplasm for degradation (Roof *et al.*, 1994). In the GMK cell line, P23H rhodopsin appears significantly different from WT rhodopsin. We have reported the same for P23H rhodopsin in HEK293S. From our quantification it can be seen that the volumes of CNX in GMK and HEK293 with P23H rhodopsin are significantly higher than in WT. This was reported in both cell

lines. Noorwez et al. (2009) transiently transfected CNX in the stable HEK293S cell line expressing WT and P23H. The highest amount of CNX was reported in P23H. By both visual inspection and image quantification the manifestation of P23H mutation appears the same in both the GMK and HEK293 cell lines.

P23L mutation in GMK cells gives a significantly lower level of rhodopsin production compared to WT. This has been reported before in COS-1 cells by Kaushal and Khorana (1994), and also in stable HEK293 cells (Krebs *et al.*, 2010). P23L rhodopsin shows more severe behaviour as it is concentrated in the cytoplasmic area and increasing the risk of more brutal ADRP pathology, as many clinical reports indicate that patients with P23L rhodopsin mutations have a more severe form of ADRP than those with P23A mutation (Krebs *et al.*, 2005). In GMK with P23L rhodopsin CNX volume does not demonstrate any significant difference from that found in WT. However, the overlap between rhodopsin and the ER marker is significantly higher than in WT cells.

IV.4.1.3 Time-lapse imaging after co-transfection accelerate cellular death

Expression levels of proteins within a population may vary over time or within a cell population (Aymoz *et al.*, 2016). Added to this we have established knowledge about the linear relationships between fluorescent protein concentration and protein of interest concentration (Lo *et al.*, 2015). As the acquired images for fixed cells demonstrated that GMK cells can successfully handle co-transfection, we decided to extend our image quantification from just fixed cells and to investigate live cells as well. In that attempt we sacrificed many factors in order not to disrupt normal cellular

homeostasis. We trade high image resolution and the 3D information from confocal microscopy with wide-field microscopy equipped with CoolLED pE excitation system and we acquired a 2D image every one hour with short excitation time. WFM detectors are far more sensitive than those used in CLSM - between 70 and 90%, compared to a confocal's 20% quantum efficiency.

After analysing the images, we saw that those from the first time-frame demonstrated a close resemblance to what we had observed in fixed cells with regard to WT and mutant rhodopsin-GFP production and its association with CNX. However, the rest of the images showed the high sensitivity of the GMK cell line to light excitation. We ended up doing the quantification on just the very low number of cells which managed to survive the first 6 hours of imaging, as death occurs after less than 6 h in severely mutant cells.

The results indicate that continued co-expression of rhodopsin-GFP (especially misfolding rhodopsin-GFP mutants) and mCherry-CNX induces cytotoxicity or accelerates cellular death. In live imaging datasets, cells lose their angular shape and filopodia, shrinking to a cytoplasmic sphere. As protein expression continues, cells show increased events of blebbing. This may be due to the membrane becoming crowded with rhodopsin-GFP, with the influx of new proteins causing pressure on the plasma membrane, until it in places dissociates from the cytoskeleton, causing blebbing and 'bursting' events of the plasma membrane. Cell integrity at these stages is severely compromised, as is further indicated by a shrinking of the cell and the loss of internal detail due to saturation of fluorescent intensity.

These cytotoxic events may be further aggravated by the generation of reactive oxygen species (ROS) during image acquisition.

In the next chapter, to investigate the contribution of phototoxicity to this cellular death, we performed live cell imaging using widefield fluorescence microscopy in order to help us see and report light-induced damage during fluorescent illumination.

Chapter V: Dynamic phenotyping: Assessing light-induced damage during fluorescence illumination

V.1 Introduction

V.1.1 Light can compromise cellular integrity in fluorescence microscopy

Photon-induced cell damage is a crucial consideration for *in vivo* light microscopy. Researchers, as well as scientific journals, are increasingly aware of this (Magidson and Khodjakov, 2013). It is also becoming clear that even very low levels of illumination can have a negative effect on cells and organisms, depending how sensitive an assessment is used. The impact of light on the observed process itself is obviously a problem for fluorescence microscopy: Observing the pathophysiological response of cells suffering incidental photodamage can lead to erroneous and deceptive conclusions. The effect of light does not necessarily have to be a negative one. Positive (hormetic) effects of light have been robustly demonstrated, as found for example in the field of low-level laser therapy (AlGhamdi *et al.*, 2015). However, in either case, it means that observing without disturbing is not possible in live fluorescence microscopy. The key is to assess the influence of light, and to minimise it as much as possible.

To obtain biologically relevant data, an image must have sufficient contrast, and enough spatial and temporal resolution to reliably document the observed process. These three factors are interdependent – no single factor can be changed without affecting the other two. However, at the heart of all three factors is sample health. Agreeing with previous studies (Dorn et al. 2008; Tinevez et al. 2012; Magidson & Khodjakov 2013), we submit that sample viability is of highest priority. The other parameters – contrast and spatiotemporal resolution – must be just sufficient to allow the reliable extraction of numerical data for quantification. Spatial deconvolution and

other image processing techniques reducing noise and improving contrast and spatial resolution may prove beneficial in extracting more information from our images.

V.1.2 Mechanisms of phototoxicity

Phototoxicity is a highly complex phenomenon (Diaspro et al. 2006; Débarre et al. 2014; Magidson & Khodjakov 2013). Microscopy technique, wavelength, intensity (peak and time-averaged) and exposure time (including intervals between stacks), fluorophore(s), their concentration and subcellular localisation, media, sample preparation, developmental stage, cell type and age, and synergetic effects of experimental perturbations all greatly affect a live sample under fluorescence microscopic observation. Upon irradiation of molecules in a given cell or solution, reactive chemical species with a single unpaired electron in an outer orbit (Riley, 1994) are created, the free radicals. This unstable configuration promotes reactions with adjacent molecules such as lipids, carbohydrates, and nucleic acids. The majority of free radicals relevant to photodamage are ROS. ROS, which mainly include hydrogen peroxide (H_2O_2), superoxide ($O2•^-$), hydroxyl rad-ical (•OH), peroxynitrite ($ONOO^-$), and hypochlorite (OCl^-), widely exist in living organisms and play crucial roles in cell signalling pathways (Hayyan *et al.*, 2016). ROS are strongly related to metabolic activities and are key mediators of cell function in both health and disease (Panieri and Santoro, 2015). They are continuously generated, transformed, and consumed in tissues to keep an intricate balance between ROS generation and elimination during the normal metabolic activity (Halliwell *et al.*, 2000).

ROS play an important role in stress response, apoptosis, activation of signal cascades, gene expression changes, normal development and regulation of lifespan

(Al-Mehdi *et al.*, 2012; Cadenas, 1989; Cadenas and Davies, 2000; D'Autréaux and Toledano, 2007; Dröge, 2002; Hancock *et al.*, 2001; Poli *et al.*, 2004; Van Raamsdonk and Hekimi, 2010; Wojtovich *et al.*, 2012).

During live imaging ROS are generated in the processes of fluorescing and photobleaching in two different types of reaction: The excited fluorophore can react directly with a molecular neighbour by transferring an electron, turning both the fluorophore and the electron-accepting molecule into radicals (type I reaction). Alternatively, the excited fluorophore can transfer its excess energy to molecular oxygen (type II reaction), which in turn becomes singlet oxygen (Block, 1990; Cadenas, 1989; Calmettes and Berns, 1983; Svoboda and Block, 1994). This oxygen species is highly reactive and has a long excited state lifetime, during which it can alter other molecules within the cell, giving rise to other types of ROS, thus amplifying phototoxic effects (Dahl *et al.*, 1987; Greenbaum *et al.*, 2000; Pryor, 1986; Redmond and Kochevar, 2006; Saetzler *et al.*, 1997).

The light-induced generation of ROS is perhaps the most crucial aspect of phototoxicity. It is important to understand that fluorescence microscopy relies exclusively on specific molecules which in their excited state tend to react with molecular oxygen to produce free radicals - and so imaging in fluorescence mode is automatically a phototoxic process by essence. Sudden exposure to high light intensities can provoke irreversible photoinhibition caused by the rapid accumulation of ROS, including H2O2, in chloroplasts. This leads to oxidative damage to the photosynthetic apparatus, which can trigger cell death (Exposito-Rodriguez *et al.*, 2013). ROS are generated at all wavelengths. UV light generates ROS in nucleus and cytosol (Aubin, 2003; Batista *et al.*, 2009; Davies, 2003; Dröge, 2002; Kaina, 2003). Light in the visible range triggers intracellular ROS production, with blue light a

particularly strong effect occurs (Lascaratos *et al.*, 2007; Osborne *et al.*, 2008; Wood *et al.*, 2007). While low concentrations of ROS can be buffered by the cell without damaging it, they may trigger a stress response. Typically, a cell will exit the cell cycle and enter into G0 upon expression of cyclin-dependent kinase inhibitors (Gartel and Radhakrishnan, 2005). A particular difficulty in defining a cellular response to phototoxicity is the high variability of the response. Photodamage can change cellular behaviour in entirely unpredictable ways, even for cells of the same type and in the same sample (Magidson and Khodjakov, 2013). Primary as well as secondary effects of phototoxicity (Figure V-1) are influenced by many different factors. However, in most cases, higher light intensity leads to more severe photodamage in mammalian cells (Knight et al., 2003).

V.1.3 HyPer, a GFP-based genetically encoded biosensor for intracellular hydrogen peroxide

A genetically encoded fluorescent biosensor, HyPer, is one of the most effective tools for measuring the *in vivo* concentrations of H_2O_2 (Belousov *et al.*, 2006). HyPer consists of the of an *E.coli's* regulatory domain transcription factor OxyR, which is used by this bacterium to monitor the levels of H_2O_2 (Choi *et al.*, 2001), inserted into a circularly permuted yellow fluorescent protein (Nagai *et al.*, 2001). Redox-active cysteine residues in the OxyR domain of HyPer is specifically oxidized by H2O2 and undergoes conformational changes that are transmitted to the fluorescent protein (Bilan and Belousov, 2015). The excitation spectrum of HyPer has two maxima (420 and 500 nm) which show differential changes in fluorescence emission (516 nm) after oxidation. Both forms can be visualized by laser excitation in a CLSM system or with

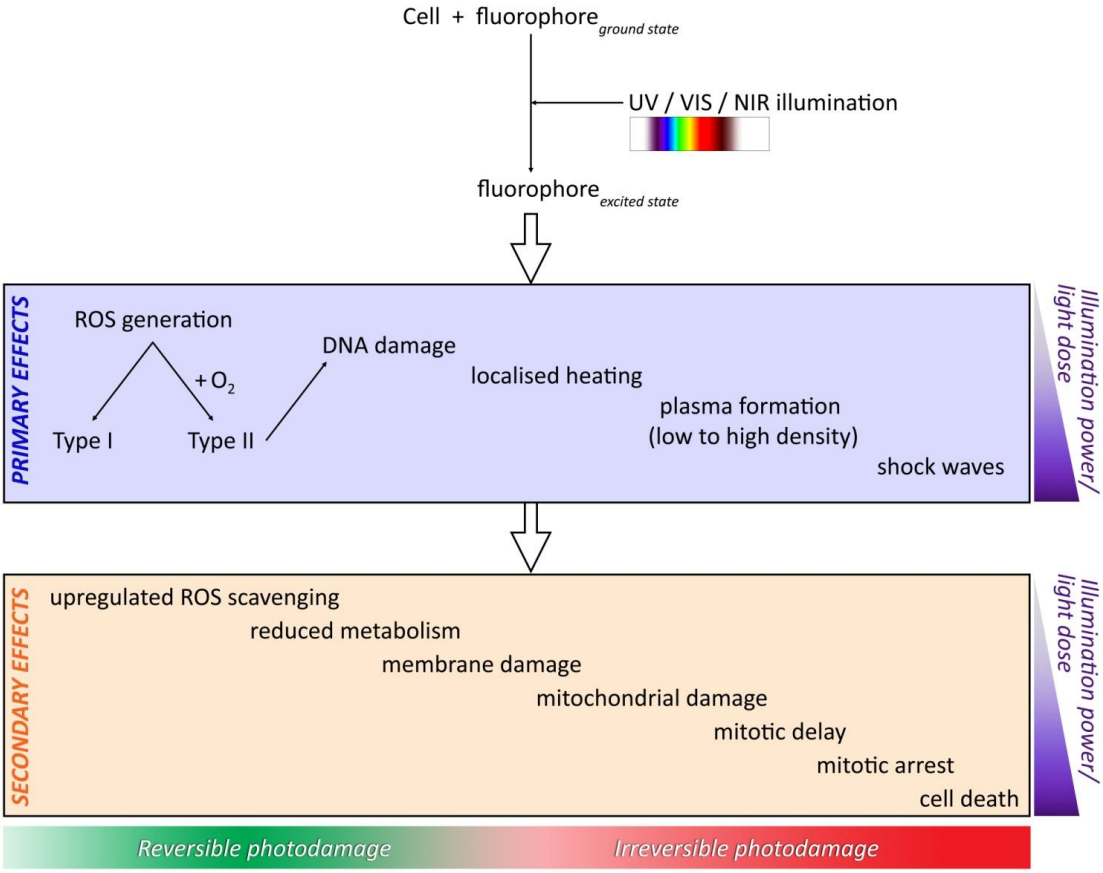

Figure V-1 Primary and secondary effects of phototoxicity.

Following photo-excitation, ROS generation will eventually leads to DNA damage and plasma formation. With continuous illumination, a cascade of reactions connected with alteration in cellular homeostasis parameters will cause cellular death.

WFM. The ability of HyPer to report increases in H_2O_2 *in vivo* has been demonstrated in E. coli, mammalian cells (Belousov et al., 2006), in the wound response of zebrafish larvae (Niethammer et al., 2009) and in Arabidopsis sgs3–11 plants (Exposito-Rodriguez et al., 2013).

V.1.4 Parameters and terminology relevant for phototoxicity

The main parameters considered in this study are listed in Table V-1. Intensity – also known as fluence rate, irradiance, radiant flux, or (surface) power density - is concerned with the amount of power the illumination has over a given surface. The SI unit is W/m^2. In the field of microscopy, mW/cm^2 is often used. The other important factor is the illumination time (exposure time), detailing for how long a sample was observed. This is measured in seconds (s), minutes (min) or hours (h). By multiplying irradiance with illumination time, we obtain the integral dose of light (also called fluence or exposure). This is the total amount of light a sample is exposed to for the duration of illumination. It is measured in energy per surface, expressed by the unit J/cm^2. Photodamage depends on both intensity and exposure time.

Phototoxicity, with respect to microscopy, is here defined as the ability of cellular photoproducts to induce cytotoxic effects when irradiated with UV/VIS/NIR light (Ibuki and Toyooka, 2015; Spielmann, 1994; Spielmann *et al.*, 2000) Although photodamage is often used synonymously, it can be defined as light-induced cellular damage that is visible using light (or fluorescence) microscopy. Applying this distinction allows a gradation of effects: Photodamage includes apoptosis as an end-point measure, and indicators such as cell cycle arrest, blebbing and rounding, indicating that the cell is stressed. However, phototoxicity affects a cell long before

Table V-1 Main measurements compared in this study

Term	Synonym	Definition	Unit(s)
Intensity*	Irradiance, fluence rate, dose rate, radiant flux, surface power density	Power (radiant energy) received by a given surface**	mW/cm^2
Illumination time	Exposure time	Total time a sample is subjected to illumination	s
Dose of light	Fluence, exposure, photon load	Product of irradiance and illumination time	J/cm^2

*Note that we use the radiometric definition of intensity. By contrast, luminous intensity (also called luminous flux) is a photometric term with the unit candela (cd), based on a human psychophysical system (Danloux-Dumesnils, 1969), and its use for scientific measurements is discouraged (Smith, 2013).

** Since the volume of different samples varies considerably, from tiny micro-organism and small single adherent cell to whole embryo or larger, the number of focal planes required for a 3D dataset varies significantly. It is thus preferable to use dose of light per surface (i.e. per single focal plane), rather than per volume.

these evident signs. Using low-level blue light exposure, Roehlecke and coworkers (Roehlecke et al., 2009) found reduced metabolism in human RPE cells which did not show any of the aforementioned visible stress symptoms. In highly photosensitive *Dictyostelium* cells, Graef and coworkers (Gräf et al., 2005) observed inhibition of mitotic progression by blue light exposure long before any bleaching effect of GFP was visible, as did Carlton and coworkers (Carlton et al., 2010) in *S. cerevisiae*.

Here we investigate the effects of blue light exposure from wide-field fluorescence microscopy on division rates and motility in GMK and PC3 cell cultures, respectively. The assessment criterion in GMK cells was the timing of mitosis, which has been proposed as the 'ideal canary in the gold mine' (Cole 2014). We further introduce a new parameter to assess phototoxicity: cell motility, in our case in the PC3 cell line. Finally, as a first step towards the quantification of ROS levels generated by illumination, we determine relative levels of hydrogen peroxide in GMK cells upon blue light irradiation using a transgenic biosensor for H_2O_2.

V.2 Experimental procedures and statistical analysis

V.2.1 Power density measurement

The 470 nm blue light intensity on the wide-field was controlled using the CoolLED pE excitation system (CoolLED, UK). This light was coming through a 20x objective lens and was monitored by an optical power meter ML9002 with MA9721A sensor ML9002A (Anritsu, Japan) and corrected by means of the responsivity curve on the back of the meter. Power per unit area (power density) was calculated in milliwatts per square centimetre mW/cm^2 then the exposure dose over one minute was

calculated as listed in Table V-2. In addition exposure doses (J/cm^2) given for longer than one minute as used in this chapter are shown in table Table V-3.

V.2.2 Determination of the effect of blue light on GMK cell proliferation by live microscopy

V.2.2.1 GMK cell preparation and image acquisition

GMK cells were grown in DMEM supplemented with 10 % FBS, 1 % penicillin/streptomycin and 1 % l-glutamine. 24 hrs before imaging, 80-90 monolayer confluence was reached. Cells were detached from the flask with TrypLE™. 2 x 10^4 cells were seeded on ibidi u-Slide 8 wells chamber plates (80826, ibidi GmbH, Munich, Germany) and kept overnight inside the tissue culture unit incubator at 37 °C, 5 % CO_2. Prior to the beginning of the experiment old growth media was removed and replaced with the appropriate amount of FluoroBrite™ DMEM supplemented with 10 % FBS, 1 % l-glutamine. Cell cultures undergoing this experiment were divided into dark control, light control and four experimental cultures (exp1, exp2, exp3 and exp4). Dark control was kept inside the tissue culture unit incubator, taken out only for imaging twice (time 0h and after 24h) and was not exposed to blue light. The rest of the cultures (light control / experimental cultures) were placed in an electric top stage microscope incubator (Model: H301, OkoLab, Italy) at 37 ^oC in 5 % CO_2. At 0.00 h those wells representing the experimental cultures (exp1, exp2, exp3 and exp4) were exposed to 20% of blue light 470 nm via the CoolLED pE excitation system (CoolLED, UK) with the following exposure doses: 9.3 J/cm^2, 13.9 J/cm^2, 18.5 J/cm^2 and 23.1 J/cm^2 respectively.

Table V-2 List of the different power densities used in this chapter

Blue light percentage (%)	Power density ($mW/cm^{2)}$	Exposure dose in (J/cm^2) in 1 min
2%	77.1 mW/cm^2	4.6 J/cm^2
5%	256.5 mW/cm^2	15.4 J/cm^2
10%	531.2 mW/cm^2	31.9 J/cm^2
20%	1040.6 mW/cm^2	62.4 J/cm^2
40%	1953.9 mW/cm^2	117.2 J/cm^2
60%	2710.6 mW/cm^2	162.6 J/cm^2
80%	3365.5 mW/cm^2	201.9 J/cm^2
100%	3922.2 mW/cm^2	235.3 J/cm^2

Table V-3 List of the different exposure doses used in this chapter

Exposure time (min)	Exposure dose in (J/cm^2) calculated with 77.1 mW/cm^2
1min	4.6 J/cm^2
2min	9.3 J/cm^2
3min	13.9 J/cm^2
4min	18.5 J/cm^2
5min	23.19 J/cm^2

Light control was not exposed to blue light radiation. Then time-lapse imaging was performed at 37 ^{O}C in 5 % CO_2 in a dark room environment to minimize light exposure to the sample and also to prevent leakage of room light into the camera. Multi-location differential interference contrast (DIC) images were taken by using a 12V 100W Halogen Lamp on automated WFM microscopy (Eclipse Ti; Nikon) using a 20× 0.75 NA objective lens. Two-dimensional time series frames were acquired with an Andor camera (Model: Luca-R DL-626, *Andor* Technology, UK) every one and a half hours up to 24 hours. The software used for image acquisition was NIS-Elements AR 4.13.04 (Build 925). All experiments were performed at least three times.

V.2.3 Determination of the GMK cell line proliferation from DIC images

Nikon NIS-Elements; 64 bit 3.21.03, Build 705 was used for DIC time-lapse image viewing and analysis. From the acquired images, we calculated the number of GMK cellular divisions in each time frame. Cellular division can be observed when the cells start to enlarge and become round, followed by two cells appearing at the same position in the next time frame image as shown in Figure V-2. The total number of cells in the final time frame was calculated as well. The cellular proliferation index was calculated by dividing the number of cell divisions by the total number of cells (Goodell *et al.*, 2012).

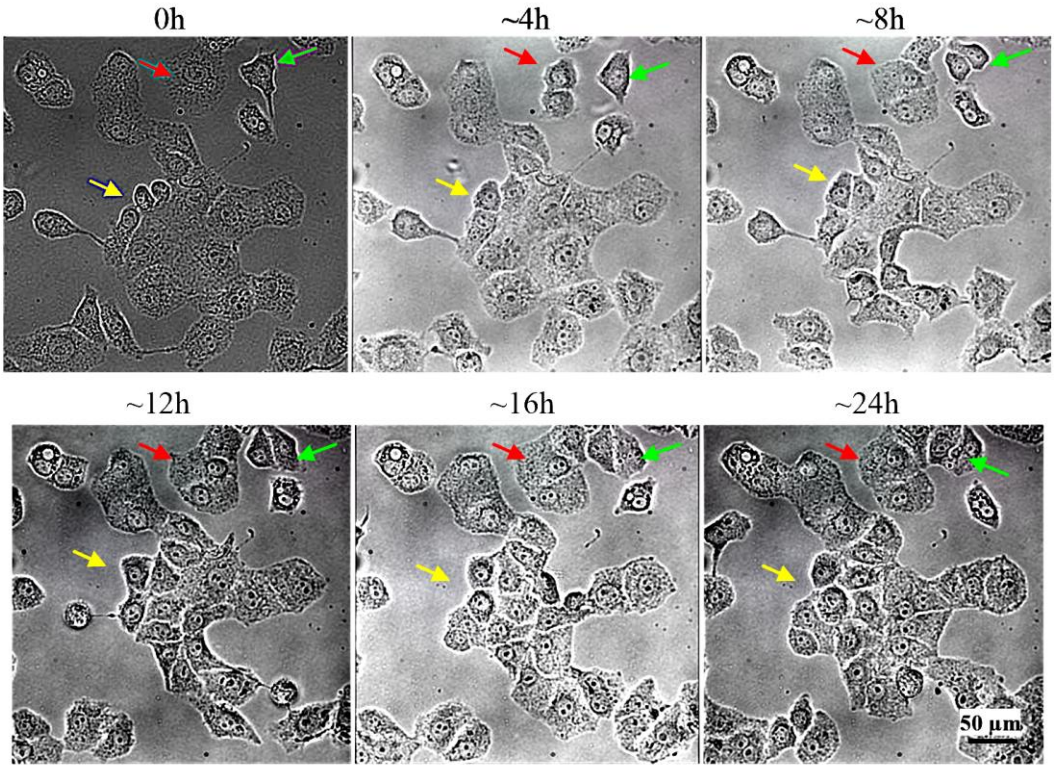

Figure V-2 DIC time-lapse images of GMK cells acquired by WFM microscope

Representative examples of GMK cells (control) undergoing cellular division (red, green and yellow arrows). Each event of cellular division has been counted manually. Scale bar 50 µm

V.2.1 Detection of H_2O_2 production as an indicator for phototoxicity within GMK after blue light exposure using HyPer

V.2.1.1 Transfection of GMK cells with Hyper

GMK cells were grown in DMEM supplemented with 10 % FBS, 1 % penicillin/streptomycin and 1 % l-glutamine. 24 hrs before co-transfection, 80-90 monolayer confluence was reached. Cells were detached from the flask with TrypLE™. 2 x 10^4 cells were seeded on ibidi u-Slide 8 wells chamber plates (80826, ibidi GmbH, Munich, Germany) and kept overnight inside the tissue culture unit incubator at 37 °C, 5 % CO_2. Cells were then transfected with 1 µg of pC1-HyPer-3 (HyPer) and 2 µl TurboFect (section II.2.6.5) then incubated for 48 hrs after transfection. Old growth media with the transfection reagent residue was removed and replaced with the appropriate amount of FluoroBrite™ DMEM supplemented with 10 % FBS, 1 % l-glutamine. Some of the cells were used to test the sensitivity of HyPer to H_2O_2 while the rest were used for blue light radiation experiments (test and control).

V.2.1.2 Testing the sensitivity of HyPer to H_2O_2 in GMK cell using CLSM microscope

To determine the response of HyPer to H_2O_2 we added a solution of H_2O_2 in 100 µL volume to one of the wells containing control cells to give a final concentration of 50 and 150 micro molar (µM). Images were acquired before and after the addition of H_2O_2. Time-lapse imaging was performed at 37 ^oC in 5 % CO_2 in a dark room environment to minimize light exposure to the sample and also to prevent leakage of

room light into the camera. Images were acquired continuously for up to 18 minutes with a Nikon A1si CLSM microscope with a plan-apochromatic VC 1.30 N.A. 40 x magnifying oil-immersion objective lens. The software used for image acquisition was NIS-Elements AR 4.13.01 (Build 916). Images were acquired in two channels, using one-way sequential line scans of two excitation lines, with laser power at 398 nm and at 488 nm.

V.2.1.3 Exposing GMK cell to blue light after their transfection with HyPer

Cells transfected with Hyper were placed on electric top stage microscope incubator (Model: H301,OkoLab, Italy) at 37 ^{o}C in 5 % CO_2, and were exposed to 2% of blue light 470 nm via the CoolLED pE excitation system (CoolLED, UK) with a radiation dose of 23.1 J/cm^2. Cells transfected with Hyper which represented the control sample were not exposed to blue light.

Live imaging was performed on both; control and the ones exposed to blue light at 37 ^{o}C in 5 % CO_2 in a dark room environment to minimize light exposure to the sample and also to prevent leakage of room light into the camera. Multiple location images were acquired over 24 hours with a Nikon A1si CLSM with a plan-apochromatic VC 1.30 N.A. 40 x magnifying oil-immersion objective lens. The software used for image acquisition was NIS-Elements AR 4.13.01 (Build 916). Images were acquired in two channels, using one-way sequential line scans of two excitation lines, with laser power of 12 and 3 at wavelengths of 398 nm and 488 nm respectively.

V.2.1.4 Ratio-metric image analysis for GMK cell transfected with Hyper

NIS-Elements; 64 bit 3.21.03, Build 705 was used in this analysis. Through the ratio view option in the software we visually observed and selected the cells of interest. We restricted our analysis to just the images in the first time frame. Automated fluorescent measurement was performed on regions of interest. This allowed us to measure and compare the ratio of the fluorescent signals in the selected cells. Data was then normalised and exported for graphing and statistical analysis.

V.2.1.5 PC3 cell preparation and image acquisition

Stable PC3 cells expressing GFP (PC3-GFP) were grown in RPMI-1640, supplemented with 10% FBS, L-glutamine and 1 % penicillin/streptomycin and 1 % l-glutamine. 24 hrs before imaging, 80-90 monolayer confluence was reached. Cells were detached from the flask with TrypLE™. 2 x 10^4 cells were seeded on ibidi u-Slide 8 wells chamber plates (80826, ibidi GmbH, Munich, Germany) and kept overnight inside the tissue culture unit incubator at 37 °C, 5 % CO_2. Prior to the beginning of the experiment old growth media was removed and replaced with the appropriate amount of FluoroBrite™ DMEM supplemented with 10 % FBS, 1 % l-glutamine. Cell cultures undergoing this experiment were divided into control and six experimental cultures (exp1, exp2, exp3, exp4, exp5 and exp6).

Samples were placed in electric top stage microscope incubator (Model: H301, OkoLab, Italy) at 37 ^oC in 5 % CO_2. At 0.00 h wells representing the experiments (exp1, exp2, exp3, exp4, exp5 and exp6) were exposed to different percentages of blue light 470 nm via a CoolLED pE excitation system for one minute (10%, 20%,

40%, 60%, 80% and 100%) respectively (see Table V-2). The light control sample was not exposed to blue light at this point. Time-lapse imaging was performed at 37 ^{o}C in 5 % CO_2 in a dark room environment to minimize light exposure to the sample and also to prevent leakage of room light into the camera. Multi-location time lapse images were taken by automated WFM microscopy (Eclipse Ti; Nikon) using a 20× 0.75 NA objective lens. GFP signals for PC3 cells were excited with a CoolLED pE excitation system (CoolLED, UK). PC3 was illuminated at 5% of 470 nm with 3 second exposure time) and imaged using a FITC filter. During imaging power density was kept constant at 256.5 mW/cm^2/stack. Two-dimensional time series frames were acquired with an Andor camera (Model: Luca-R DL-626, *Andor* Technology, UK) every 15 minutes for 24 hours. The software used for image acquisition was; NIS-Elements AR 4.13.04 (Build 925). All experiments were performed at least three times.

V.2.2 The determination of PC3 cell line motility via single cell tracking

On PC3 time-lapse images, analysis and tracking of single cell movements was performed using CellTracker which is implemented using MATLAB (Piccinini *et al.*, 2016). Three replicates from each control and experimental cell culture were analysed. The GUI of CellTracker is designed to intuitively support users during the analysis. We used semiautomatic tracking and selected the cells to be tracked. The algorithm defines a specific template for each selected cell and searches for the best match in the following frames. We only tracked cells that were present in the first frame; cells touching image borders were excluded. All tracks were examined and

those belonging to non-isolated cells deleted. The average speed (μm/min) for each cell was calculated as the sum length of the cell's trajectory divided by the total time over which the trajectory was measured. We extracted the cell track results from at least three independent experiments. Figure V-3 shows a representation of the cell tracking routine using CellTracker GUI.

V.2.3 Statistical analysis

A nonparametric test for independent samples (Kruskal-Wallis) was used to compare the means of different data. Furthermore, Dunn's nonparametric pairwise multiple comparisons test was used to verify whether there were any significant differences between the different blue light irradiated groups and the controls. An unpaired t test was used when comparing the significant difference between two groups. In all cases, a p-value of ≤ 0.05 was considered to be significant. Astrikes symbols were used to indicate statistical significance (* $p \leq 0.05$).

All graphing was performed using the graphing and statistical software GraphPad Prism 7. Box plots represent 25–75 percentiles and whiskers were assigned using the Tukey method.

V.3 Results

V.3.1 Low blue light exposure leads to delayed mitosis in GMK cells

The box and whiskers plot in Figure V-4 represents the proliferation index of the GMK cell line. The control sample was reported to have the highest median for cell proliferation at 37% followed by exp2 at 31%, exp1 at 28%, exp4 at 22% and exp3 at 17%. Beyond this, no statistically significant difference was recorded between control

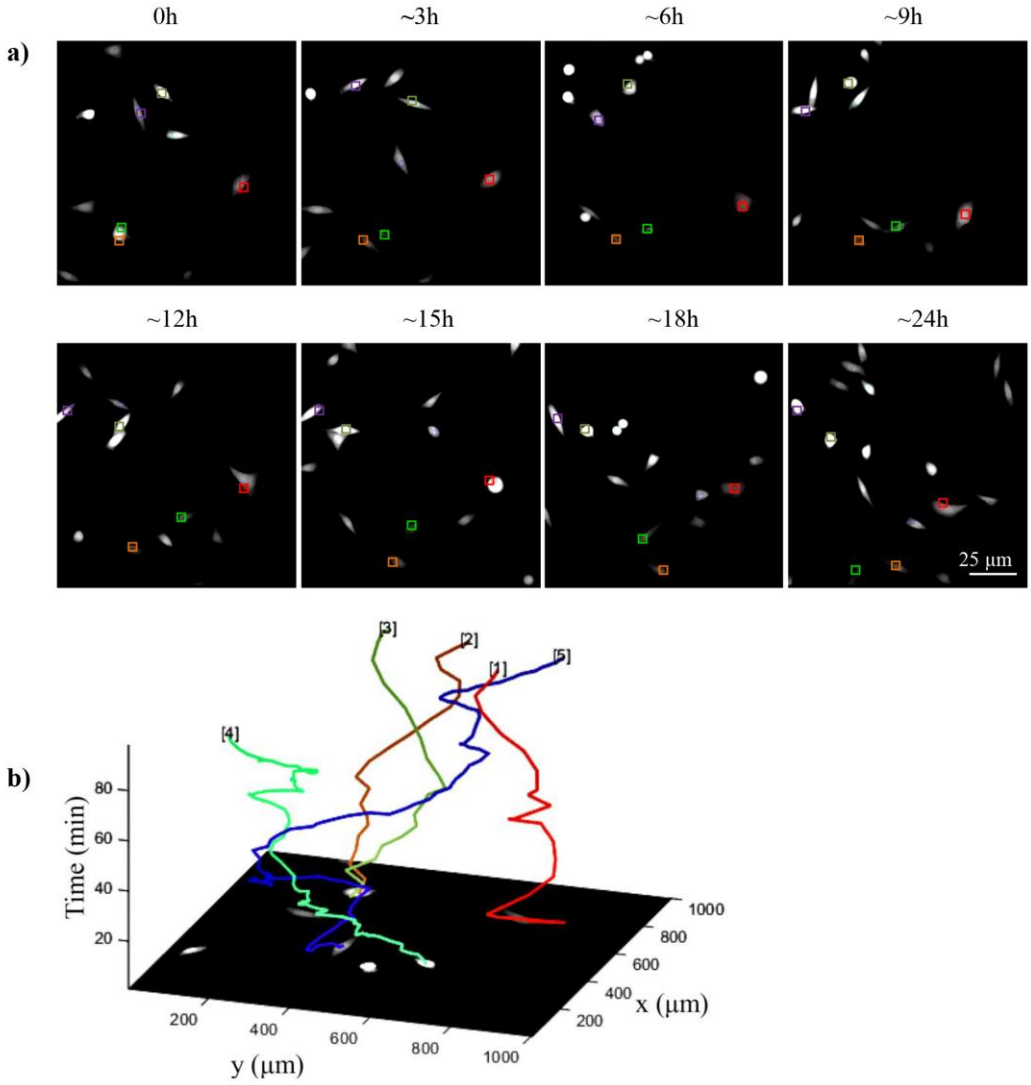

Figure V-3 Time-lapse images of PC3 cells acquired by WFM microscope.

a) Representative examples of PC3 cells tracks over time made using CellTrack. b) The 3D tracks plot displays all the tracks over time on a *x-y-z* plot, where the *z*-axis represents the cell trajectories on phase contrast images.

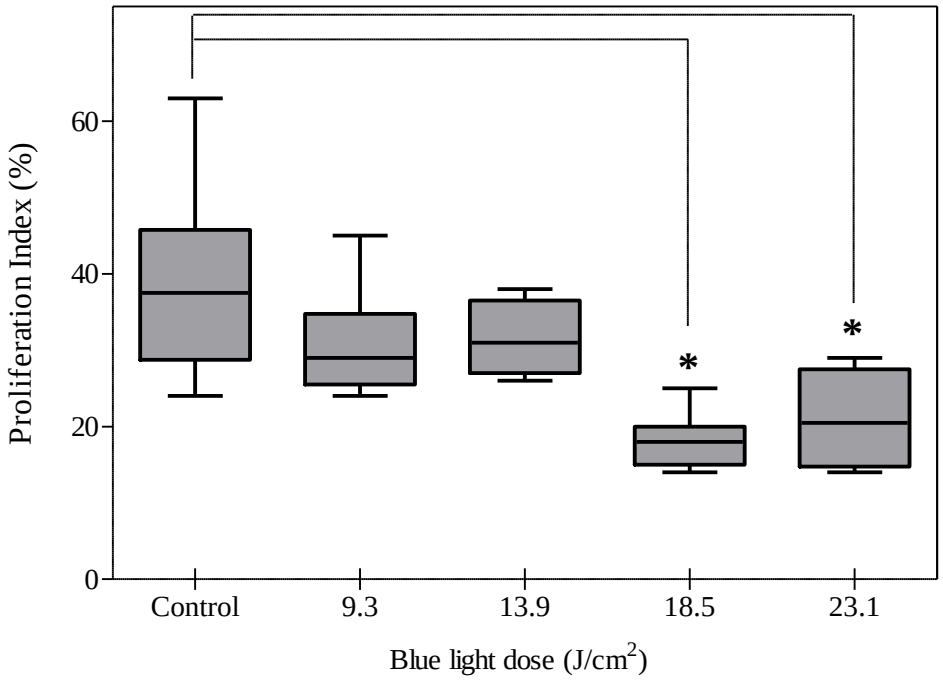

Figure V-4 Percentages of the GMK proliferation index distribution after treatment with different doses of blue light

The boxes in the plot represent the middle half distribution of the proliferation index in the GMK cell line, stretching from the 25th percentile to the 75th percentile. The bold line across the box represents the median (37, 28, 31, 17 and 20) for control, exp1, exp2, exp3, and exp4 respectively. Exposing GMK cells to 18.5 J/cm^2 and 23.1 J/cm^2 of blue light manifested in a significant reduction in the cellular proliferation index in exp3 and exp4. Asterisks (*) denote $p < 0.05$ in comparison with the control.

and exp1 and exp2 and that suggested that blue light radiation of 9.3 J/cm^2 and 13.9 J/cm^2 did not affect the rate of GMK cellular division. On the contrary, exposing GMK cells to 18.5 J/cm^2 and 23.1 J/cm^2 of blue light manifested in a significant reduction in the cellular proliferation rate in exp3 and exp4 in comparison with the control, with $p<0.05$.

V.3.2 HyPer demonstrates high sensitivity to changes in the concentration of H_2O_2 in the cell culture medium

We detected the fluorescence of HyPer upon irradiation of the cells with the ratio view between 398 nm and 488 nm lasers. The addition of 50 μM and 150 μM of H_2O_2 led to a fast change in the fluorescent signal as the oxidation state increased. The increased fluorescent signal following HyPer response to H_2O_2 is shown in representative images of GMK cells with their corresponding line chart in Figure V-5.

V.3.1 Blue light illumination induces H_2O_2 production in GMK cells

We used a spectrum scale (Figure V-6) together with the ratio view to represent the relative change between the oxidation and reduction states in GMK cells. HyPer intensity reaches it maximum response to about 3 fold with the addition of H_2O_2 solution. Moreover the background intensity did not change with the addition of H_2O_2 solution. The presence of a high concentration of H_2O_2 put the cells into the oxidative state (red), whilst when the H_2O_2 was very low HyPer in the ratio view was reported to be in the reduction state (blue). Figure V-6 shows a comparison between HyPer's response to the H_2O_2 in the control cell and in a cell imaged immediately after being irradiated with 23.1 J/cm^2 of blue light.

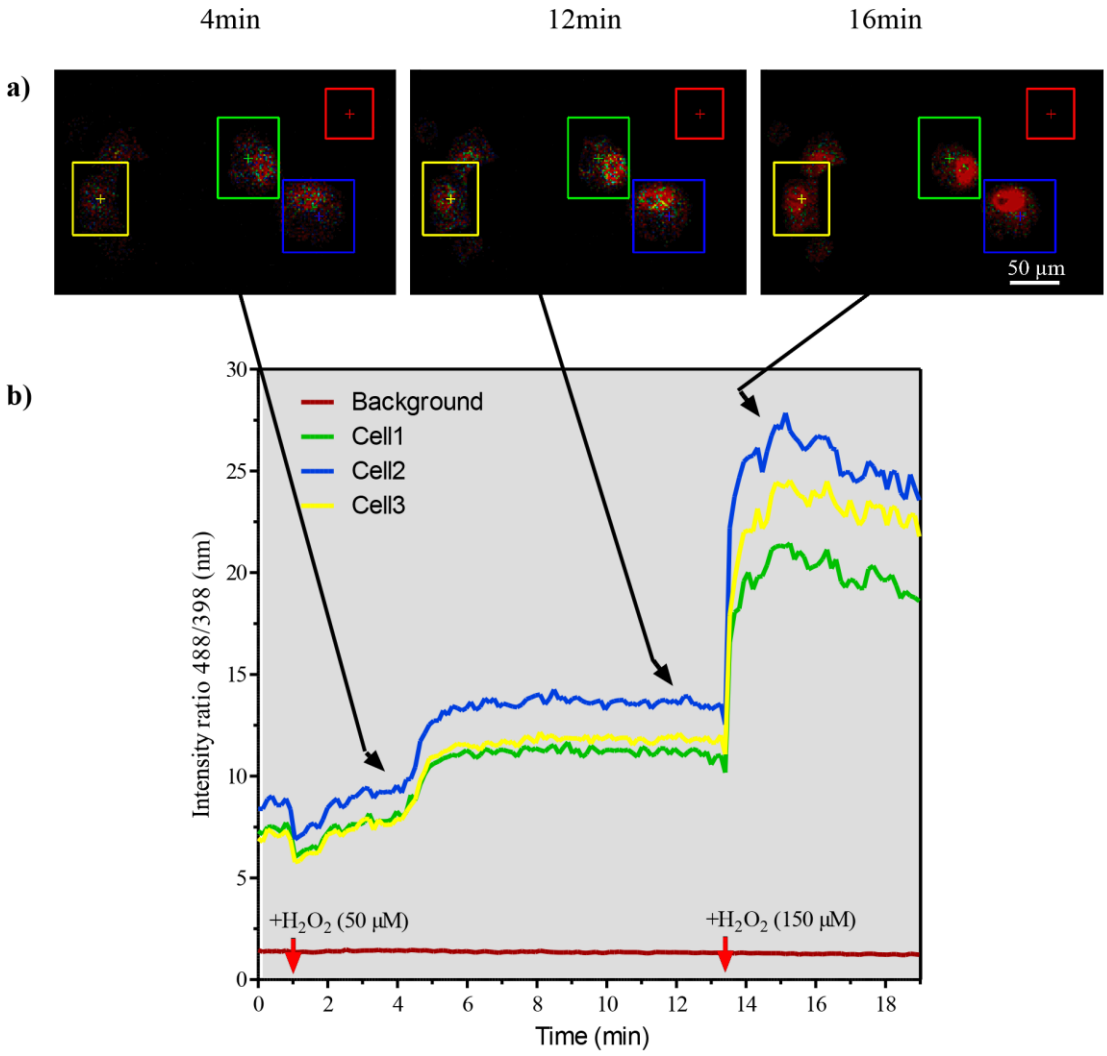

Figure V-5 Fluorescence lifetime CLSM imaging of GMK cells transfected with HyPer with corresponding intensity chart.

a) The response of HyPer to the addition of H2O2 to GMK cells is indicated by the increase in the fluorescent signal over. b) Each line in the chart represents the intensity's change in the regions of interest (coloured square) over time with the addition of H2O2 (red arrows). HyPer intensity reaches its maximum response of about 3 fold with the addition of H2O2 solution after 15 min. The background shows no change with the addition of H2O2.

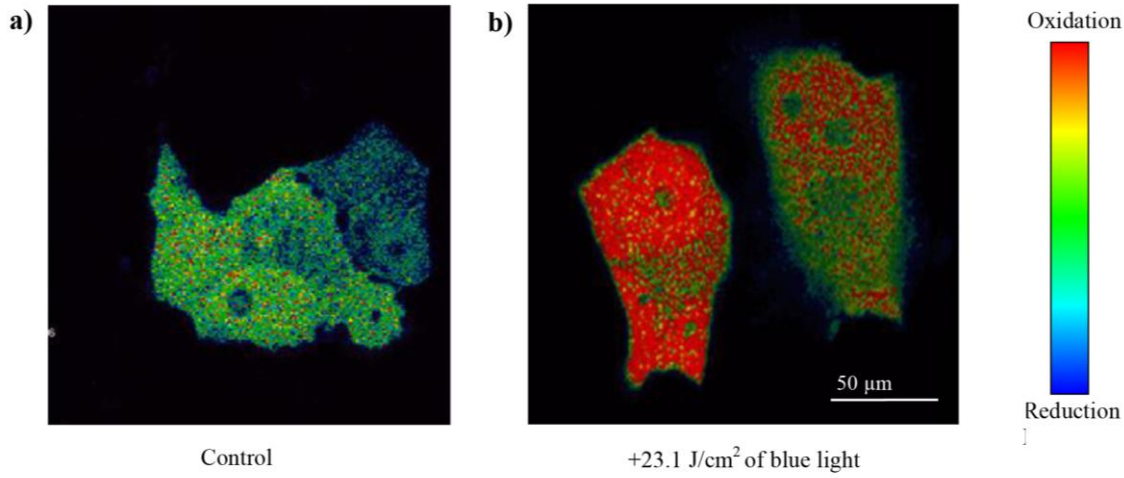

Figure V-6 Ratio view (488/398 nm) of HyPer response in control and blue light irradiated GMK cells.

a) The HyPer signal in the control cells does not indicate the presence of a high concentration of H_2O_2. b) Cells irradiated with 23.1 J/cm^2 of blue light demonstrate an increase in HyPer signal towards the oxidative state. The colour scale shows the spectrum between oxidation and reduction.

HyPer's response in the irradiated cell demonstrates an increase in H_2O_2 levels within the cell and hence increases in the oxidative state. On the other hand HyPer in the control did not indicate the presence of H_2O_2, which suggests that irradiation with 23.1 J/cm^2 of blue light induces the production of H_2O_2. Next we extracted the ratio of HyPer intensities (488/398 nm) from the CLSM images of the control (n=28) and irradiated cells (n=40) and plotted them as shown in Figure V-7. The normalised percentages of the fluorescent ratio of HyPer in the irradiated cells are higher than in the control cells with the median at 40% and this was reported to be significant in comparison to the control with $p<0.05$.

V.3.2 Blue light exposure reduces motility in PC3 cells

The effect of varying blue light power on PC3 cells' motility is illustrated in Figure V-8. Control cells were recorded to reach the highest speed at 0.49 μm/min. However, experimental groups were affected significantly ($p<0.05$) after being exposed to blue light with radiation doses between 31.9 J/cm^2 and 235.3 J/cm^2 for only one minute.

V.4 Discussion

The direct imaging of biological events as they unfold is a uniquely powerful approach. However, high light intensities can lead to irreversible damage in the observed cell, tissue or organism. Avoiding this photon-induced cell damage is key for *in vivo* light microscopy, since observing the pathophysiological response of cells suffering incidental photodamage often leads to false conclusions. In this Chapter, we propose simple methods to directly measure the relationship between blue light

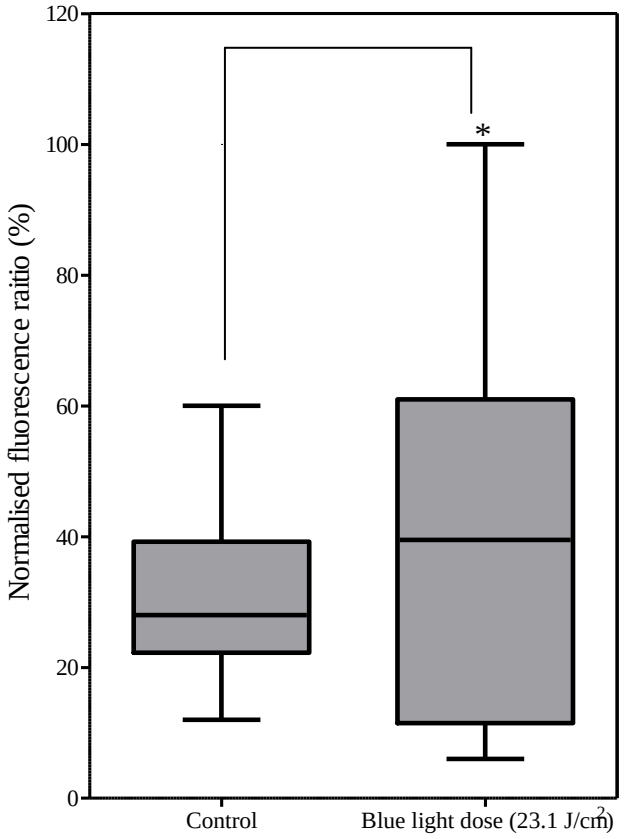

Figure V-7 Normalised HyPer fluorescence ratio in GMK cells

The boxes in the plot represent the middle half distribution of the HyPer fluorescence ratio in control (n=28) and in irradiated cells with 23.1 J/cm^2 of blue light (n=40). The bold line across the box represents the median (27 % and 40 %) for control and irradiated cells respectively. Percentages of HyPer in the irradiated cells are higher than in the control sample and were reported to be significantly different in comparison with the control. Asterisk (*) denotes $p < 0.05$.

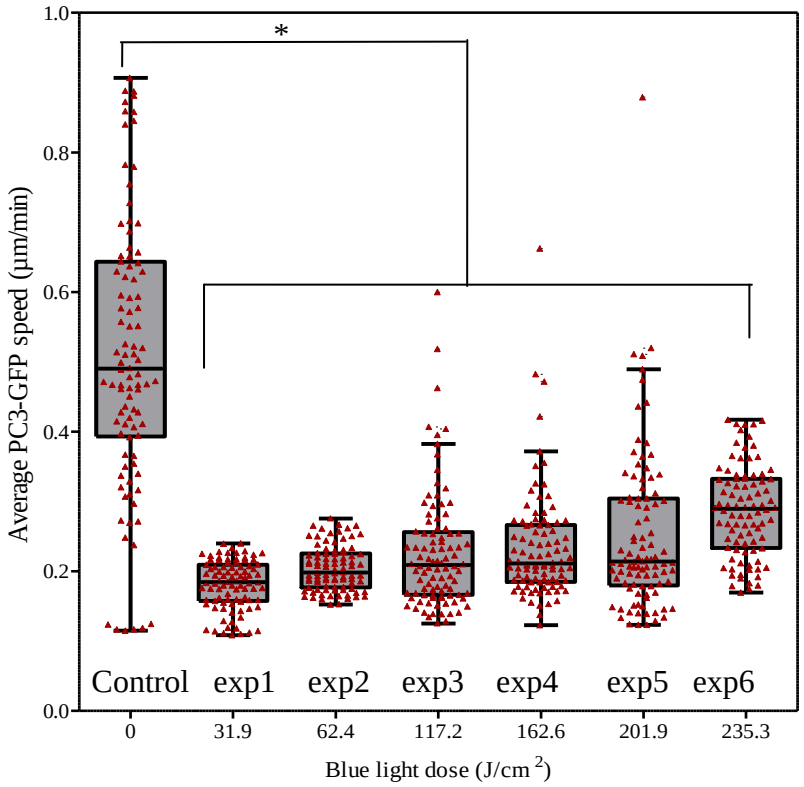

Figure V-8 Average speed of PC3 cells in µm/min after treatment with varying levels of blue light.

The box plot represents the middle half distribution of cell speed. The bold line across the box represents the median (0.49, 0.18, 0.19, 0.20, 0.21, 0.21 and 0.28) for control, exp1, exp2, exp3, exp4, exp5, and exp6 respectively. The overlaid dot plot represents the distribution of individual PC3 cell speeds which are affected significantly by radiation doses of blue light between 31.9 J/cm^2 and 235.3 J/cm^2. Asterisk (*) denotes $p < 0.05$ in comparison with the control.

exposure doses from WFM and phototoxicity in GMK and PC3 mammalian cell cultures.

V.4.1 Irradiation with blue light affect GMK cells cycle and caused delayed mitosis

Mitosis and cell cycle progression are regulated by a wide variety of external factors, amongst them are growth factors and extracellular matrix factors. The major control switches for the cell cycle are Cdks (cyclin dependent kinases). Cdks are enzymes that add negatively charged phosphate groups to other molecules in a process called phosphorylation. Through phosphorylation, Cdks signal the cell that it is ready to pass into the next stage of the cell cycle (LaBaer et al., 1997). Boonstra and Post (2004) reported that ROS may also play an important role in cell cycle progression. ROS are formed in substantial amounts in living cells and these highly reactive species can damage a variety of biomolecules, such as lipids, proteins, carbohydrates and nucleic acids. As a consequence the majority of the effects of ROS on cells are a-specific, depending on the localization, nature and concentration of the ROS involved (Boonstra and Post, 2004). High ROS concentration causes an induction of the cyclin kinase inhibitors those inhibiters reported to induced DNA damage and or block DNA synthesis which will eventually lead to mitotic arrest. From our experiment, we reported that exposing GMK cells to blue light illumination would cause an increase in ROS production. Illumination with a blue light dose between 9.3 and 13.9 J/cm^2 did not cause a significant decrease in cell division. However because the average proliferation is about 9% lower than control we cannot rule out the possibility of a hidden primary side effect which has not been revealed by this approach. Moreover

with the dose between 18.5 and 23.1 J/cm^2 a decrease in the cell proliferation rate was recorded and it can be link to a mitotic arrest which suggests that the secondary effect of photodamage is induced under this condition which may be due ROS causing an activation of cyclin kinase inhibitors (not investigated). Our results suggest that the dose at which blue light is delivered is critical to the eventual phototoxic impact.

V.4.2 Irradiation with blue light and H_2O_2 production in GMK cells

Of all ROS the most long-lived in biological systems is hydrogen peroxide (H_2O_2) (Belousov *et al.*, 2006). The production and accumulation of H_2O_2 occurs in many sub-cellular compartments. The chemical stability of H_2O_2 means that it can potentially diffuse or be transported away from its site of production to be neutralised or exert regulatory effects elsewhere in the cell or tissue (Exposito-Rodriguez *et al.*, 2013). After irradiation with the same dose that caused the mitotic arrest in the GMK cells (23.1 J/cm^2). We believe that HyPer is a good indicator of the presence of H_2O_2. The ratio between the fluorescence excited by 488 nm and 398 nm lasers can be used as a function of H_20_2 concentration as this ratio is proportional to H_2O_2 (Belousov et al., 2006). We expected the relative concentration of H_2O_2 to be higher in 23.1 J/cm^2 irradiated cells in comparison to control where no phototoxicity occurred. The significant increase in H_2O_2 detected by HyPer upon illumination could be an indication of ROS inducing secondary photodamage as we observed previously with the mitotic arrest in the GMK cells.

From our experiments, blue light irradiation with 13.9 J/cm^2 has been found to be the threshold for imaging GMK cells without inducing mitotic delay. Interestingly, in his photodamage assay Tinevez et al. (2012) posit a threshold value of 0.001 J/cm^2 for the

number of cell nuclei divisions in developing *C. elegans* embryos. This could be a clear indicator that phototoxicity is highly cell type dependant. However, *C. elegans* from Tinevez's study lives naturally in the absence of light, and its embryogenesis is highly photosensitive to epifluorescent illumination, which in the case of CLSM leads to arrested development (Mohler *et al.*, 1998)

V.4.3 Reduction in the speed of PC3 cells as an indicator of photodamage

Cell motility is a primary component of tumour cell invasion. It is considered to be a continuum of sequential events in which the cell extends pseudopodia, forms nascent attachments, assembles and contracts the cytoskeleton, and finally, as it translocates forward, disengages distal adhesions (Matsumoto *et al.*, 1995). Although several studies have looked over the effects of ROS on cell motility and migration, variable results have been reported were based on the type of ROS, it concentration, production site, and as well as the tissue type of the cells under question (Luanpitpong et al., 2010).

With the increasing evidence suggesting that signalling molecules presenting in the tumour microenvironment have a significant impact on the migratory properties of cancer cells (Kopfstein and Christofori, 2006; Laurent et al., 2005). For example, increased ROS in the tumour microenvironment has been associated with increased aggressiveness of cancer cells (Dröge, 2002).

We investigated the correlation of PC3 speed when a phototoxic light effect was introduced. We believed that exposing PC3 cells to blue light might generate an increasing concentration of ROS in PC3 microenvironment. ROS are likely to affect

cancer cell motility and invasiveness through multiple mechanisms (Laurent *et al.*, 2005). In our experiments, PC3 cell motility was analysed by tracking cells in movies generated by time-lapse microscopy. We quantified PC3 speed and the control sample was recorded to reach the highest speed at 0.49 μm/min. Cells irradiated with blue light doses between 31.9 J/cm^2 and 235.3 J/cm^2 showed a significant decrease in their speed to about 30 % lower than control. We believed that as happened in the case of GMK cells after irradiation, a phototoxic effect was also induced in PC3 cells. With the established knowledge that illuminating GMK cells with 235.3 J/cm^2 dose of blue light caused H_2O_2 production. We reasoned that doses between 31.9 J/cm^2 and 235.3 J/cm^2 can generate H_2O_2 in PC3 cells.

The radiation doses may induce an oxidative stress, which brings about the production of potentially destructive ROS, especially H_2O_2 and/or other kinds of ROS (not investigated). Managing the elevated level of ROS within the cell requires high cellular energy, which leads eventually to ATP depletion. Motility will decrease dramatically as the cell falls into an ATP budget state and uses its energy to preserve the cell's viability. And it has been reported before that ROS depleted ATP in human spermatozoa and inhibits sperm motility (De Lamirande and Gagnon, 1991).

Chapter VI: Summary and future work

Summary

In this thesis, we applied several methods of quantitative image analysis for the assessment and quantification of phenotypic changes in subcellular components, cellular homeostasis and dynamics within given cell lines.

We first started with an extensive review exploring background and origin of rhodopsin phenotypes associated with autosomal dominant retinitis pigmentosa (ADRP). This is followed by an overview of digital fluorescence microscopy and potential pitfalls arising from wrong analysis, interpretation, photodamage, and/or sample handling and preparation.

Statistical methods were applied throughout the research in order to demonstrate the effectiveness of the quantification approach and to validate the results we obtained against: visual interpretation and/or related literature and/or the experiment control.

In Chapter III, we investigated three point mutations in the rhodopsin gene which are strongly linked to its misfolding, resulting in endoplasmic reticulum retention and degradation. These mutations were expressed stably in HEK293S cell line. Rhodopsin association with calnexin was also investigated. For this task we used two automated image analysis algorithms to quantify aggresomes and determine the distribution of rhodopsin phenotypic variations within and among the cellular models for autosomal dominant retinitis pigmentosa using 3D digital microscopy. Visual interpretation was part of this task however with the variations in those phenotypes appearance requires image-based quantification for robustness, which makes visual interpretation on its own time-consuming and limited conclusions that can be drawn.

By using the novel method published by (Obara et al., 2013), we successfully detected the number of aggresomes in mutant rhodopsin, however the sensitivity of this

algorithm was so high it over-estimated the number of aggresomes in wild-type which makes the intervention by visual observer necessary for correcting this finding. Automated threshold based segmentation successfully characterises the volumes of rhodopsin-GFP and CNX-mAb in the stable cell line. Our findings support those from published literature.

It was reported that, in stable transfected HEK293S cells, total opsin levels were ten-fold lower in P23H than in WT cells (Noorwez et al., 2009). The methodology they used was immunoprecipitation and Western blotting. Our results using image quantification largely support their findings. We found that P23H rhodopsin is 19% less than WT. Interestingly, P23A rhodopsin quantification recorded to be not significant compared to WT and we reached the same conclusion with visual interpretation which showed that P23A cells are like WT, expressing high levels of rhodopsin-GFP.

After image quantification and evaluation of rescued P23H mutation. The rescued P23H mutant showed a significantly higher volume of rhodopsin-GFP expression compared to the non-rescued P23H mutant. Although the exact mechanism of the rescue is not explained by image analysis, we reasoned that the correct folding of rhodopsin is critically important for rhodopsin translocation into the cellular membrane as we observed in P23H rescued images.

For CNX-mAb the difference between WT and P23H was statistically significant with the highest CNX-mAb volume in P23H. Interestingly, Noorwez et al. (2009) analyzed the levels of CNX in the cell lysates, CNX was associated with P23H than with WT. In our quantification, the detected overlap of CNX-mAb with rhodopsin-GFP in both P23A and P23H mutation was recorded to be significantly higher than WT.

Optimally stained samples subjected to the correct parameters for image acquisition are critical for reliable outcome. On feasible and non-feasible images we reached the conclusion that not all acquired images can produce reliable quantitative results. In contrast to good quality feasible images, the unfeasible images belonging to P23L and P23L-rescued showed lack of quality as the automated algorithm failed to quantify them we tried to correlate the quantification results with visual inspection however they did not match.

Finally, the stable transfected HEK293S cell line had been considered to be a good model for studying ADRP, and testing the automated quantification, however the morphology of this cell line is not satisfactory for highlighting the high production of rhodopsin-GFP expression. And that triggered the need to peruse the testing of the automated algorithm in a cell with decent endomembrane area.

In Chapter IV we investigated the interaction and localisation of rhodopsin phenotypes with CNX in the GMK cells. We used the same automated quantification algorithm that we have validated in Chapter III. Co-expression of rhodopsin-GFP and mCherry-CNX in GMK gives distinct phenotypical differences between WT and the investigated mutants.

In general, P23A in both cell lines demonstrates a resemblance to WT on both visual inspection and occasionally with quantification.

Volumes of CNX in GMK and HEK293 with P23H rhodopsin are significantly higher than in WT. P23L mutation in GMK cells gives a significantly lower level of rhodopsin production compared to WT. This has been reported before in COS-1 cells by Kaushal and Khorana (1994), and also in stable HEK293 cells (Krebs et al., 2010).

In GMK with P23L rhodopsin CNX volume does not demonstrate any significant difference from that found in WT. However, the overlap between rhodopsin and the ER marker is significantly higher than in WT cells.

We decided to extend our image quantification from just fixed cells and to investigate live cells. In that attempt, we sacrificed many factors in order not to disrupt normal cellular homeostasis. We trade high image resolution and the 3D information from confocal microscopy with wide-field microscopy equipped with CoolLED excitation. Images from the first time-frame demonstrate a close resemblance to what we had observed in fixed GMK cells with regard to WT and mutant rhodopsin-GFP production and its association with CNX. However, the rest of the images showed the high sensitivity of the GMK cell line to light excitation. We ended up doing the quantification on just the very low number of cells that managed to survive the first 6 hours of imaging, as death occurs after less than 6 h in severely mutant cells.

The results indicate that continued co-expression of rhodopsin-GFP (especially misfolding rhodopsin-GFP mutants) and mCherry-CNX induces cytotoxicity or accelerates cellular death. In live imaging datasets, cells lose their angular shape and filopodia, shrinking to a cytoplasmic sphere. As protein expression continues, cells show increased events of blebbing. These cytotoxic events may be further aggravated by the generation of reactive oxygen species during image acquisition.

In Chapter V we investigated the contribution of phototoxicity to cellular phototoxicity to this cellular death recorded in Chapter IV, we performed live cell imaging using wide-field microscopy in order to help us see and report light-induced damage during fluorescent illumination. Our results suggest that the dose at which blue light is delivered is critical to the eventual phototoxic impact. We then investigated the level of the H2O2, the brutal member of the ROS superoxide's

family, after irradiation with the same dose that caused the mitotic arrest in the GMK cells (23.1 J/cm^2). The relative concentration of H_2O_2 to be higher in 23.1 J/cm^2 irradiated cells in comparison to control where no phototoxicity occurred. The significant increase in H_2O_2 detected by HyPer upon illumination could be an indication of ROS inducing secondary photodamage as we observed previously with the mitotic arrest in the GMK cells. In conclusion, quantifying the damage induced by light on living cells is not straightforward. Phototoxicity depends on many factors such as cell type, imaging conditions, duration of the experiment and the intracellular distribution and concentrations of fluorophores. With our straightforward methods, we directly measured the relationship between the blue light irradiation from WFM and the incidence of phototoxicity in GMK and PC3 mammalian cell culture. Cell division and cell motility are exquisitely delicate processes, and are a highly sensitive way to assess phototoxic effects.

Future work

One of the most promising directions taken in this thesis is the sensitive assessment of phototoxicity using cell motility and mitotic delay, and monitoring the increase in intracellular hydrogen peroxide as an end product of ROS generation using the HyPer biosensor. Integration of these findings into a single model could provide a practical working model for phototoxicity. A preliminary attempt has been recently presented at the 3rd international Light-sheet Fluorescence Microscopy conference (see 'Related publications and presentations'). A suitable model for phototoxicity was based the Gompertz distribution (Gompertz, 1825; Kirkwood, 2015), widely used to describe the distribution of adult deaths. We propose a qualitative model of the generic biphasic response of a cell to illumination and exposure time. The y-axis values are inverted, so the downward slope in the graph represents declining cell health. Plotted in three spatial dimensions, it provides an intuitive landscape for a simple biphasic model of phototoxicity. The high plateau stands for cells in homeostasis. The bassin of the graph represents the zone of cell death. Low light microscopy is found along the top left side of the graph. In this model, the slope does not increase linearly, but exponentially. This is consistent with the higher phototoxicity evident in high-intensity techniques such as confocal laser scanning microscopy (CLSM).

The projected, inverted Gompertz distribution (Figure F-1) provides a three-dimensional landscape that qualitatively agrees with published studies. However, a quantitative experimental approach is needed in which the two fundamental image

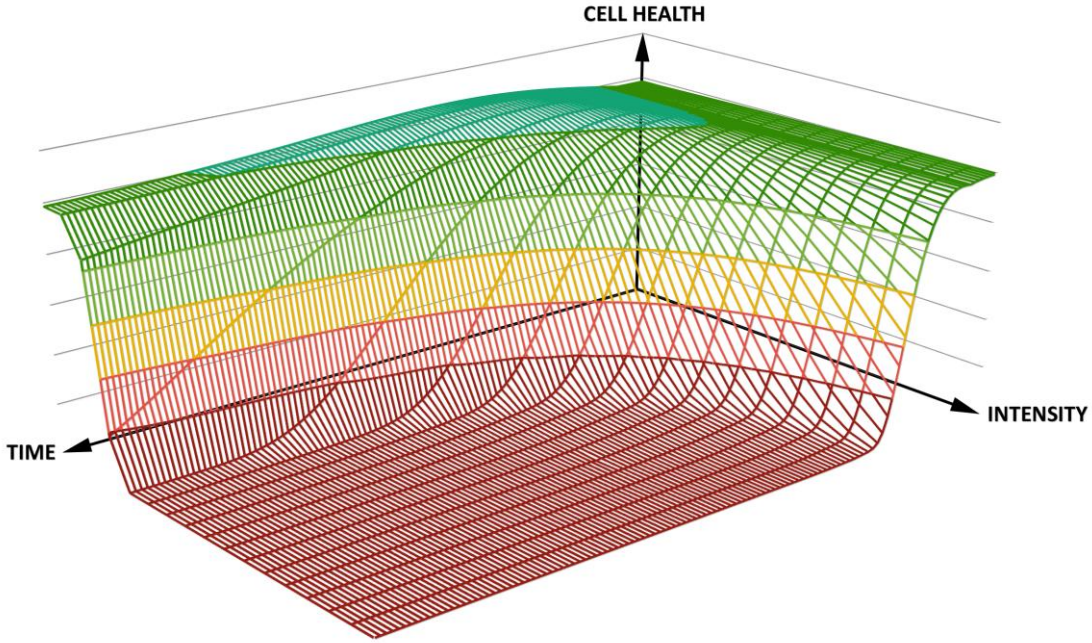

Figure F-1 Qualitative three-dimensional inverted Gompertz distribution as a model for biphasic effects of phototoxicity on cellular or organismal health.

acquisition parameters (intensity and exposure time) are systematically varied, while their effect on cellular homeostasis is assessed. Using such an array of image acquisition conditions and their cellular consequences could provide sufficient datapoints to construct a robust 3D 'landscape' of phototoxicity for the cells in question. Phototoxicity is sample-dependent, so caution should be exercised in drawing conclusions from this model to other kinds of samples. However, such a model would provide very useful information on how single cells deal with an increase in intracellular hydrogen peroxide caused by illumination, and show how exposure time and intensity are not reciprocal effects. By including different intervals between acquisitions (allowing fluorophores and cells to recover from illumination effects between images), optimal parameters may further be found. Since we are using mammalian cell lines, blue light excitation and fluorescent proteins in the green and yellow emission range, the results would provide highly relevant practical considerations for a majority of routinely used microscopy approaches.

Finally, generating stable GMK cells co-expressing rhodopsin phenotypes and calnexin is a project we want to undertake in order to examine how different pharmacological rescues approaches affect the interaction between rhodopsin and calnexin.

Related publications and presentations

- Assessing and reporting phototoxicity in live imaging: Notes from LSFM2016. Pierre Philippe Laissue, Rana Alghamdi, Pavel Tomancak, Emmanuel G. Reynaud, Hari Shroff (Manuscript submitted).
- Blue light illumination at low intensity and short exposure times reduces cell motility and delays mitosis in PC3 and GMK cell lines. Rana Alghamdi, Marino Exposito-Rodriguez and Pierre Philippe Laissue. In preparation.
- Interactions between CD74 and CD44 expressed in human breast cancer derived cells. Al Ssadh Hussain, Alabdulmenaim Waleed, Alghamdi Rana, Spencer Patrick and Nelson Fernández. (Manuscript submitted)
- Assessing, Reducing and Reporting Phototoxicity In Lightsheet and Conventional Fluorescence Microscopy. Rana Alghamdi, Marino Exposito-Rodriguez and Pierre Philippe Laissue. 3rd Light Sheet Fluorescence Microscopy International Conference, Sheffield, UK, August 2016.
- Quantification of GFP-tagged rhodopsin phenotypes and their localisation with calnexin-mAb in a cellular model of Autosomal Dominant Retinitis Pigmentosa. Alghamdi RA, Boguslaw O, South K, Opefi CA, Reeves PJ, Laissue PP. The 9th Saudi students conference, London, UK, February 2016.
- Quantified phenotype analysis in a cell model for Autosomal Dominant Retinitis Pigmentosa. Alghamdi RA, Boguslaw O, South K, Opefi CA, Reeves PJ, Laissue PP. International Microscopy Congress, Prague, Czech Republic. September 2014.
- Quantified, three-dimensional, object-based colocalisation for characterising cellular phenotypes. Obara B, Alghamdi R, Jabeen A, Fernandez N, South K,

Reeves PJ & Laissue PP. 26th International Conference on 3D Image Processing in Microscopy, Focus on Microscopy, Maastricht, Netherland, Mar 2013.

References

Adler, J. and Parmryd, I. (2014) Quantifying Colocalization: Thresholding, Void Voxels and the Hcoef. *Public Library of Science,* **9**, e111983.

Al-Mehdi, A.-B., Pastukh, V. M., Swiger, B. M., Reed, D. J., Patel, M. R., Bardwell, G. C., Pastukh, V. V., Alexeyev, M. F. and Gillespie, M. N. (2012) Perinuclear mitochondrial clustering creates an oxidant-rich nuclear domain required for hypoxia-induced transcription. *Science signaling,* **5**, ra47.

AlGhamdi, K. M., Kumar, A., Ashour, A. E. and AlGhamdi, A. A. (2015) A comparative study of the effects of different low-level lasers on the proliferation, viability, and migration of human melanocytes in vitro. *Lasers in medical science,* 1-11.

Atchison, D. A. and Smith, G. (2000) Optics of The Human Eyes. 269.

Aubin, F. (2003) Mechanisms involved in ultraviolet light-induced immunosuppression. *European Journal of Dermatology,* **13**, 515-523.

Ayers, G. and Dainty, J. C. (1988) Iterative blind deconvolution method and its applications. *Optics letters,* **13**, 547-549.

Aymoz, D., Wosika, V., Durandau, E. and Pelet, S. (2016) Real-time quantification of protein expression at the single-cell level via dynamic protein synthesis translocation reporters. *Nature communications,* **7**.

Bartosz, G. (1997) Oxidative stress in plants. *Acta Physiologiae Plantarum,* **19**, 47-64.

Batista, L. F., Kaina, B., Meneghini, R. and Menck, C. F. (2009) How DNA lesions are turned into powerful killing structures: insights from UV-induced apoptosis. *Mutation Research/Reviews in Mutation Research,* **681**, 197-208.

Belousov, V. V., Fradkov, A. F., Lukyanov, K. A., Staroverov, D. B., Shakhbazov, K. S., Terskikh, A. V. and Lukyanov, S. (2006) Genetically encoded fluorescent indicator for intracellular hydrogen peroxide. *Nature Methods,* **3**, 281-286.

Bernas, T., ZARĘBSKI, M., Cook, R. and Dobrucki, J. (2004) Minimizing photobleaching during confocal microscopy of fluorescent probes bound to chromatin: role of anoxia and photon flux. *Journal of Microscopy,* **215**, 281-296.

Berson, E. L., Rosner, B., Sandberg, M. A. and Dryja, T. P. (1991) Ocular findings in patients with autosomal dominant retinitis pigmentosa and a rhodopsin gene defect (Pro-23-His). *Archives of ophthalmology,* **109**, 92-101.

Bhandawat, V., Reisert, J. and Yau, K. W. (2005) Elementary response of olfactory receptor neurons to odorants. *Science,* **308**, 1931-4.

Bilan, D. S. and Belousov, V. V. (2015) HyPer family probes: state of the art. *Antioxidants and Redox Signaling*.

Block, S. (1990) Optical tweezers: a new tool for biophysics. *Modern cell biology,* **9**, 375-402.

Bolisetty, S. and Jaimes, E. A. (2013) Mitochondria and reactive oxygen species: physiology and pathophysiology. *International journal of molecular sciences,* **14**, 6306-6344.

Boonstra, J. and Post, J. A. (2004) Molecular events associated with reactive oxygen species and cell cycle progression in mammalian cells. *Gene,* **337**, 1-13.

Brayton, C. (2011) Nature and Nurture: Impacts on Mouse Phenotypes and Translational Research. *In:* Brakebusch, C. and Pihlajaniemi, T. (eds.) *Mouse*

as a Model Organism: From Animals to Cells. Dordrecht: Springer Netherlands.

Cadenas, E. (1989) Biochemistry of oxygen toxicity. *Annual review of biochemistry*, **58**, 79-110.

Cadenas, E. and Davies, K. J. (2000) Mitochondrial free radical generation, oxidative stress, and aging. *Free Radical Biology and Medicine*, **29**, 222-230.

Calmettes, P. P. and Berns, M. W. (1983) Laser-induced multiphoton processes in living cells. *Proceedings of the National Academy of Sciences*, **80**, 7197-7199.

Chabre, M. (1985) Trigger and amplification mechanisms in visual phototransduction. *Annu Rev Biophys Biophys Chem*, **14**, 331-60.

Chandler, D. E. and Roberson, R. W. (2009) *Bioimaging: Current Concepts in Light & Electron Microscopy.* Jones & Bartlett Publishers.

Chansawang, N., Obara, B., Geider, R. J. and Laissue, P. P. (2016) Three-Dimensional Visualisation and Quantification of Lipids in Microalgae Using Confocal Laser Scanning Microscopy. *In:* McGenity, J. T., Timmis, N. K. and Nogales, B. (eds.) *Hydrocarbon and Lipid Microbiology Protocols: Ultrastructure and Imaging.* Berlin, Heidelberg: Springer Berlin Heidelberg.

Chiang, W.-C., Kroeger, H., Sakami, S., Messah, C., Yasumura, D., Matthes, M. T., Coppinger, J. A., Palczewski, K., LaVail, M. M. and Lin, J. H. (2015) Robust Endoplasmic Reticulum-Associated Degradation of Rhodopsin Precedes Retinal Degeneration. *Molecular neurobiology*, **52**, 679-695.

Chieco, P., Jonker, A., De Boer, B. A., Ruijter, J. M. and Van Noorden, C. J. F. (2013) Image Cytometry: Protocols for 2D and 3D Quantification in Microscopic Images. *Progress in Histochemistry and Cytochemistry*, **47**, 211-333.

Choi, H.-J., Kim, S.-J., Mukhopadhyay, P., Cho, S., Woo, J.-R., Storz, G. and Ryu, S.-E. (2001) Structural Basis of the Redox Switch in the OxyR Transcription Factor. *Cell*, **105**, 103-113.

Coling, D. and Kachar, B. (2001) Theory and application of fluorescence microscopy. *Current Protocols in Neuroscience*, 2.1. 1-2.1. 11.

Combs, C. A. (2010) Fluorescence microscopy: a concise guide to current imaging methods. *Current Protocols in Neuroscience*, 2.1. 1-2.1. 14.

Cranfill, P. J., Sell, B. R., Baird, M. A., Allen, J. R., Lavagnino, Z., de Gruiter, H. M., Kremers, G.-J., Davidson, M. W., Ustione, A. and Piston, D. W. (2016) Quantitative assessment of fluorescent proteins. *Nature Methods*.

D'Autréaux, B. and Toledano, M. B. (2007) ROS as signalling molecules: mechanisms that generate specificity in ROS homeostasis. *Nature reviews Molecular cell biology*, **8**, 813-824.

Dahl, T., RobertMiddenand, W. and Hartman, P. (1987) Pure singlet oxygen cytotoxicity for bacteria. *Photochemistry and photobiology*, **46**, 345-352.

Danloux-Dumesnils, M. (1969) *The metric system: a critical study of its principles and practice.* Burns & Oates.

Davies, M. J. (2003) Singlet oxygen-mediated damage to proteins and its consequences. *Biochemical and Biophysical Research Communications*, **305**, 761-770.

De Lamirande, E. and Gagnon, C. (1991) Reactive oxygen species and human spermatozoa. II. Depletion of adenosine triphosphate plays an important role in the inhibition of sperm motility. *Journal of Andrology*, **13**, 379-386.

De Vos, W. H., Hoebe, R. A., Joss, G. H., Haffmans, W., Baatout, S., Van Oostveldt, P. and Manders, E. M. (2009) Controlled light exposure microscopy reveals dynamic telomere microterritories throughout the cell cycle. *Cytometry Part A,* **75**, 428-439.

Debarre, D., Olivier, N., Supatto, W. and Beaurepaire, E. (2014) Mitigating Phototoxicity during Multiphoton Microscopy of Live Drosophila Embryos in the 1.0–1.2 μ m Wavelength Range. *Public Library of Science,* **9**, e104250.

Diaspro, A., Chirico, G., Usai, C., Ramoino, P. and Dobrucki, J. (2006) Photobleaching. *Handbook of Biological Confocal Microscopy.* Springer.

Diaz Zamboni, J. E., Osella, D., Paravani, E. V. and Casco, V. H. (2015) Evaluation and Validation of a Semiautomatic Image Analysis Method: Quantification of Nares Cell Proliferation of Rhinella arenarum (Anura) Detected with the Avidin-Biotin Complex/Peroxidase, DAB. *Journal of Histology,* **2015**.

Dixit, R. and Cyr, R. (2003) Cell damage and reactive oxygen species production induced by fluorescence microscopy: effect on mitosis and guidelines for non-invasive fluorescence microscopy. *The Plant Journal,* **36**, 280-290.

Dixit, R., Cyr, R. and Gilroy, S. (2006) Using intrinsically fluorescent proteins for plant cell imaging. *The Plant Journal,* **45**, 599-615.

Dobrucki, J. W. (2001) Interaction of oxygen-sensitive luminescent probes Ru (phen) 3 2+ and Ru (bipy) 3 2+ with animal and plant cells in vitro: Mechanism of phototoxicity and conditions for non-invasive oxygen measurements. *Journal of Photochemistry and Photobiology B: Biology,* **65**, 136-144.

Dobrucki, J. W. (2013) Fluorescence Microscopy. *Fluorescence Microscopy: From Principles to Biological Applications.* Wiley-VCH Verlag GmbH & Co. KGaA.

Dobrucki, J. W., Feret, D. and Noatynska, A. (2007) Scattering of exciting light by live cells in fluorescence confocal imaging: phototoxic effects and relevance for FRAP studies. *Biophys Journal,* **93**, 1778-86.

Downer, N. W. and Cone, R. A. (1985) Transient dichroism in photoreceptor membranes indicates that stable oligomers of rhodopsin do not form during excitation. *Biophysical Journal,* **47**, 277-84.

Dröge, W. (2002) Free radicals in the physiological control of cell function. *Physiol Rev,* **82**, 47-95.

Dryja, T. P., McGee, T. L., Reichel, E., Hahn, L. B., Cowley, G. S., Yandell, D. W., Sandberg, M. A. and Berson, E. L. (1990) A point mutation of the rhodopsin gene in one form of retinitis pigmentosa. *Nature,* **343**, 364-366.

Dunn, K. W., Kamocka, M. M. and McDonald, J. H. (2011) A practical guide to evaluating colocalization in biological microscopy. *American Journal of Physiology. Cell Physiology,* **300**, C723-42.

Eils, R. and Athale, C. (2003) Computational imaging in cell biology. *Journal of Cell Biology,* **161**.

Exposito-Rodriguez, M., Laissue, P. P., Littlejohn, G. R., Smirnoff, N. and Mullineaux, P. M. (2013) Chapter Ten - The Use of HyPer to Examine Spatial and Temporal Changes in H2O2 in High Light-Exposed Plants. *In:* Enrique, C. and Lester, P. (eds.) *Methods in Enzymology.* Academic Press.

Filipek, S., Teller, D. C., Palczewski, K. and Stenkamp, R. (2003) The crystallographic model of rhodopsin and its use in studies of other G protein-coupled receptors. *Annual review of biophysics and biomolecular structure,* **32**, 375-97.

Fink, C., Morgan, F. and Loew, L. M. (1998) Intracellular fluorescent probe concentrations by confocal microscopy. *Biophys Journal*, **75**, 1648-58.

Frederick, J. M., Krasnoperova, N. V., Hoffmann, K., Church-Kopish, J., Ruther, K., Howes, K., Lem, J. and Baehr, W. (2001) Mutant rhodopsin transgene expression on a null background. *Investigative Ophthalmology and Visual Science*, **42**, 826-833.

Frigault, M. M., Lacoste, J., Swift, J. L. and Brown, C. M. (2009) Live-cell microscopy – tips and tools. *Journal of cell science*, **122**, 753-767.

Gal, A., Apfelstedt-Sylla, E., Janecke, A. and Zrennert, E. (1997) Rhodopsin mutations in inherited retinal dystrophies and dysfunctions. *Progress in Retinal and Eye Research*, **16**, 51-79.

García-Mata, R., Bebök, Z., Sorscher, E. J. and Sztul, E. S. (1999) Characterization and Dynamics of Aggresome Formation by a Cytosolic Gfp-Chimera. *The Journal of cell biology*, **146**, 1239-1254.

Garriga, P. and Manyosa, J. (2002) The eye photoreceptor protein rhodopsin. Structural implications for retinal disease1. *FEBS letters*, **528**, 17-22.

Genetics, H. R. (2012) *RHO - rhodopsin* [Online]: http://ghr.nlm.nih.gov/gene/RHO. US National Library of Medicine, National Institutes of Health, Department of Health & Human Services. Last accessed 12 November

Gerlich, D. and Ellenberg, J. (2001) 4D imaging to assay complex dynamics in live specimens. *Biology*, **2**, 268-275.

Gerlich, D. and Ellenberg, J. (2003) 4D imaging to assay complex dynamics in live specimens. *Nature cell biology*, S14-9.

Godley, B. F., Shamsi, F. A., Liang, F.-Q., Jarrett, S. G., Davies, S. and Boulton, M. (2005) Blue light induces mitochondrial DNA damage and free radical production in epithelial cells. *Journal of Biological Chemistry*, **280**, 21061-21066.

Gompertz, B. (1825) On the nature of the function expressive of the law of human mortality, and on a new mode of determining the value of life contingencies. *Philosophical transactions of the Royal Society of London*, **115**, 513-583.

Goodell, P. P., Krasinskas, A. M., Davison, J. M. and Hartman, D. J. (2012) Comparison of Methods for Proliferative Index Analysis for Grading Pancreatic Well-Differentiated Neuroendocrine Tumors. *American Journal of Clinical Pathology*, **137**, 576-582.

Gorbatyuk, M. S., Gorbatyuk, O. S., LaVail, M. M., Lin, J. H., Hauswirth, W. W. and Lewin, A. S. (2012) Functional rescue of P23H rhodopsin photoreceptors by gene delivery. *Advances in experimental medicine and biology*, **723**, 191-7.

Gorbatyuk, M. S., Knox, T., LaVail, M. M., Gorbatyuk, O. S., Noorwez, S. M., Hauswirth, W. W., Lin, J. H., Muzyczka, N. and Lewin, A. S. (2010) Restoration of visual function in P23H rhodopsin transgenic rats by gene delivery of BiP/Grp78. *Proceedings of the National Academy of Sciences*, **107**, 5961-5966.

Gordon, A., Colman-Lerner, A., Chin, T. E., Benjamin, K. R., Richard, C. Y. and Brent, R. (2007) Single-cell quantification of molecules and rates using open-source microscope-based cytometry. *Nature Methods*, **4**, 175-181.

Graham, F. L., Smiley, J., Russell, W. C. and Nairn, R. (1977) Characteristics of a Human Cell Line Transformed by DNA from Human Adenovirus Type 5. *Journal of General Virology*, **36**, 59-72.

Greenbaum, L., Rothmann, C., Lavie, R. and Malik, Z. (2000) Green fluorescent protein photobleaching: a model for protein damage by endogenous and exogenous singlet oxygen. *Biological chemistry*, **381**, 1251-1258.

Gurcan, M. N., Boucheron, L. E., Can, A., Madabhushi, A., Rajpoot, N. M. and Yener, B. (2009) Histopathological image analysis: A review. *IEEE reviews in biomedical engineering*, **2**, 147-171.

Haidekker, M. (2011) *Advanced biomedical image analysis.* John Wiley & Sons.

Hall, T. S. (1969) *Ideas of life and matter.*

Halliwell, B., Clement, M. V. and Long, L. H. (2000) Hydrogen peroxide in the human body. *FEBS letters*, **486**, 10-13.

Hamel, C. (2006) Retinitis pigmentosa. *Orphanet Journal of Rare Diseases*, **1**, 40.

Hamilton, N. (2009) Quantification and its Applications in Fluorescent Microscopy Imaging. *Traffic*, **10**, 951-961.

Hancock, J., Desikan, R. and Neill, S. (2001) Role of reactive oxygen species in cell signalling pathways. *Biochemical Society Transactions*, **29**, 345-349.

Hargrave, P. (2001) Rhodopsin Structure, Function, and Topography The Friedenwald Lecture. *Investigative Ophthalmology and Visual Science*, **42**, 3-9.

Hartong, D. T., Berson, E. L. and Dryja, T. P. (2006) Retinitis pigmentosa. *The Lancet*, **368**, 1795-1809.

Hayyan, M., Hashim, M. A. and AlNashef, I. M. (2016) Superoxide Ion: Generation and Chemical Implications. *Chemical reviews*, **116**, 3029-3085.

Hebert, D. and Molinari, M. (2007) In and out of the ER: protein folding, quality control, degradation, and related human diseases. *Physiol Rev*, **87**, 1377-1408.

Hecht, E. (1987) *Optics.* Addison Wesley.

Heck, M. and Hofmann, K. P. (2001) Maximal rate and nucleotide dependence of rhodopsin-catalyzed transducin activation: initial rate analysis based on a double displacement mechanism. *Journal of Biological Chemistry*, **276**, 10000-9.

Hirao, K., Natsuka, Y., Tamura, T., Wada, I., Morito, D., Natsuka, S., Romero, P., Sleno, B., Tremblay, L., Herscovics, A., Nagata, K. and Hosokawa, N. (2006) EDEM3, a soluble EDEM homolog, enhances glycoprotein endoplasmic reticulum-associated degradation and mannose trimming. *The Journal of biological chemistry*, **281**, 9650-9658.

Hockberger, P. E., Skimina, T. A., Centonze, V. E., Lavin, C., Chu, S., Dadras, S., Reddy, J. K. and White, J. G. (1999) Activation of flavin-containing oxidases underlies light-induced production of H(2)O(2) in mammalian cells. *Proceedings of the National Academy of Sciences of the United States of America*, **96**, 6255-6260.

Hoebe, R., Van Der Voort, H., Stap, J., Van Noorden, C. and Manders, E. (2008) Quantitative determination of the reduction of phototoxicity and photobleaching by controlled light exposure microscopy. *Journal of Microscopy*, **231**, 9-20.

Hogan, M. J., Alvarado, J. A. and Weddell, J. E. (1971) *Histology of the Human Eye: An Atlas and Textbook.* Saunders Philadelphia, PA.

Holmes, T. J. (1988) Maximum-likelihood image restoration adapted for noncoherent optical imaging. *Journal of the Optical Society of America*, **5**, 666-673.

Holmes, T. J., Bhattacharyya, S., Cooper, J. A., Hanzel, D., Krishnamurthi, V., Lin, W.-c., Roysam, B., Szarowski, D. H. and Turner, J. N. (1995) Light

microscopic images reconstructed by maximum likelihood deconvolution. *Handbook of Biological Confocal Microscopy.* Springer.

Holmes, T. J., Biggs, D. and Abu-Tarif, A. (2006) Blind deconvolution. *Handbook of Biological Confocal Microscopy.* Springer.

Hu, Y., Osuna-Highley, E., Hua, J., Nowicki, T. S., Stolz, R., McKayle, C. and Murphy, R. F. (2010) Automated analysis of protein subcellular location in time series images. *Bioinformatics,* **26**, 1630-1636.

Huang, K. and Murphy, R. F. (2004) Boosting accuracy of automated classification of fluorescence microscope images for location proteomics. *BMC bioinformatics,* **5**, 1.

Ibuki, Y. and Toyooka, T. (2015) Evaluation of chemical phototoxicity, focusing on phosphorylated histone H2AX. *J Radiat Res,* **56**, 220-8.

Illing, M., Rajan, R., Bence, N. and Kopito, R. (2002) A rhodopsin mutant linked to autosomal dominant retinitis pigmentosa is prone to aggregate and interacts with the ubiquitin proteasome system. *The Journal of biological chemistry,* **277**, 34150-34160.

Johnson, S., Halford, S., Morris, A. G., Patel, R. J., Wilkie, S. E., Hardcastle, A. J., Moore, A. T., Zhang, K. and Hunt, D. M. (2003) Genomic organisation and alternative splicing of human RIM1, a gene implicated in autosomal dominant cone-rod dystrophy (CORD7). *Genomics,* **81**, 304-14.

Kaina, B. (2003) DNA damage-triggered apoptosis: critical role of DNA repair, double-strand breaks, cell proliferation and signaling. *Biochemical pharmacology,* **66**, 1547-1554.

Kandori, H., Shichida, Y. and Yoshizawa, T. (2001) Photoisomerization in rhodopsin. *Biochemistry (Moscow),* **66**, 1197-1209.

Kauffman, G. B. and Adloff, J. (2009) The 2008 Nobel Prize in Chemistry: Osamu Shimomura, Martin Chalfie & Roger Y Tsien: The green Fluorescent Protein. *Chemical Educator,* **14**, 70-78.

Kaushal, S. and Khorana, H. G. (1994) Structure and function in rhodopsin. 7. Point mutations associated with autosomal dominant retinitis pigmentosa. *Biochemistry,* **33**, 6121-6128.

Kherlopian, A. R., Song, T., Duan, Q., Neimark, M. A., Po, M. J., Gohagan, J. K. and Laine, A. F. (2008) A review of imaging techniques for systems biology. *BMC Systems Biology,* **2**, 74.

Kirkwood, T. B. (2015) Deciphering death: a commentary on Gompertz (1825)'On the nature of the function expressive of the law of human mortality, and on a new mode of determining the value of life contingencies'. *Philosophical Transactions of the Royal Society B,* **370**, 20140379.

Kisselev, O. G. (2005) Focus on molecules: rhodopsin. *Experimental Eye Research,* **81**, 366-7.

Knight, M. M., Roberts, S. R., Lee, D. A. and Bader, D. L. (2003) Live cell imaging using confocal microscopy induces intracellular calcium transients and cell death. *American Journal of Physiology-Cell Physiology,* **284**, C1083-C1089.

Koenekoop, R. (2009) Why do Cone Photoreceptors Die in Rod-Specific Forms of Retinal Degenerations? *Ophthalmic genetics,* **30**, 152-154.

Koester, H. J., Baur, D., Uhl, R. and Hell, S. W. (1999) Ca 2+ fluorescence imaging with pico-and femtosecond two-photon excitation: signal and photodamage. *Biophysical journal,* **77**, 2226-2236.

Kolb, H. (2003) How the retina works. *American Scientist,* **91**, 28-35.

König, K., Becker, T., Fischer, P., Riemann, I. and Halbhuber, K.-J. (1999) Pulse-length dependence of cellular response to intense near-infrared laser pulses in multiphoton microscopes. *Optics letters*, **24**, 113-115.

Kopfstein, L. and Christofori, G. (2006) Metastasis: cell-autonomous mechanisms versus contributions by the tumor microenvironment. *Cellular and Molecular Life Sciences*, **63**, 449-468.

Kopito, R. R. (2000) Aggresomes, inclusion bodies and protein aggregation. *Trends in Cell Biology*, **10**, 524-530.

Kosmaoglou, M. and Cheetham, M. E. (2008) Calnexin is not essential for mammalian rod opsin biogenesis. *Molecular Vision*, **14**, 2466-74.

Kosmaoglou, M., Kanuga, N., Aguilà, M., Garriga, P. and Cheetham, M. E. (2009) A dual role for EDEM1 in the processing of rod opsin. *Journal of cell science*, **122**, 4465-72.

Krebs, M. P., Holden, D. C., Joshi, P., Clark III, C. L., Lee, A. H. and Kaushal, S. (2010) Molecular mechanisms of rhodopsin retinitis pigmentosa and the efficacy of pharmacological rescue. *Journal of Molecular Biology*, **395**, 1063-1078.

Kroeger, H., Chiang, W.-C. and Lin, J. H. (2012) Endoplasmic reticulum-associated degradation (ERAD) of misfolded glycoproteins and mutant P23H rhodopsin in photoreceptor cells. *Advances in experimental medicine and biology*, **723**, 559-65.

LaBaer, J., Garrett, M. D., Stevenson, L. F., Slingerland, J. M., Sandhu, C., Chou, H. S., Fattaey, A. and Harlow, E. (1997) New functional activities for the p21 family of CDK inhibitors. *Genes and Development*, **11**, 847-862.

Lakowicz, J. R. (1999) Introduction to Fluorescence. *Principles of Fluorescence Spectroscopy*. Boston, MA: Springer US.

Laksameethanasan, D., Tan, R. Z., Toh, G. W. and Loo, L.-H. (2013) cellXpress: a fast and user-friendly software platform for profiling cellular phenotypes. *BMC bioinformatics*, **14**, S4.

Lascaratos, G., Ji, D., Wood, J. P. and Osborne, N. N. (2007) Visible light affects mitochondrial function and induces neuronal death in retinal cell cultures. *Vision research*, **47**, 1191-1201.

Laurent, A., Nicco, C., Chéreau, C., Goulvestre, C., Alexandre, J., Alves, A., Lévy, E., Goldwasser, F., Panis, Y. and Soubrane, O. (2005) Controlling tumor growth by modulating endogenous production of reactive oxygen species. *Cancer research*, **65**, 948-956.

Lee, J. S. H., Hale, C. M., Panorchan, P., Khatau, S. B., George, J. P., Tseng, Y., Stewart, C. L., Hodzic, D. and Wirtz, D. (2007) Nuclear Lamin A/C Deficiency Induces Defects in Cell Mechanics, Polarization, and Migration. *Biophysical journal*, **93**, 2542-2552.

Lefkowitz, R. J. (2004) Historical review: a brief history and personal retrospective of seven-transmembrane receptors. *Trends Pharmacol Sciences*, **25**, 413-22.

Leskov, I. B., Klenchin, V. A., Handy, J. W., Whitlock, G. G., Govardovskii, V. I., Bownds, M. D., Lamb, T. D., Pugh, E. N., Jr. and Arshavsky, V. Y. (2000) The gain of rod phototransduction: reconciliation of biochemical and electrophysiological measurements. *Neuron*, **27**, 525-37.

Levy, D. L. and Heald, R. (2012) Mechanisms of intracellular scaling. *Annu Rev Cell Dev Biol*, **28**, 113-35.

Li, T., Snyder, W. K., Olsson, J. E. and Dryja, T. P. (1996) Transgenic mice carrying the dominant rhodopsin mutation P347S: evidence for defective vectorial transport of rhodopsin to the outer segments. *Proceedings of the National Academy of Sciences,* **93**, 14176-14181.

Lichtman, J. W. and Conchello, J.-A. (2005) Fluorescence microscopy. *Nature Methods,* **2**, 910-919.

Lin, J. H., Li, H., Yasumura, D., Cohen, H. R., Zhang, C., Panning, B., Shokat, K. M., LaVail, M. M. and Walter, P. (2007) IRE1 Signaling Affects Cell Fate During the Unfolded Protein Response. *Science,* **318**, 944-949.

Lo, C. A., Kays, I., Emran, F., Lin, T. J., Cvetkovska, V. and Chen, B. E. (2015) Quantification of Protein Levels in Single Living Cells. *Cell Rep,* **13**, 2634-44.

Loo, L.-H., Laksameethanasan, D. and Tung, Y.-L. (2014) Quantitative Protein Localization Signatures Reveal an Association between Spatial and Functional Divergences of Proteins. *PLoS Computational Biology,* **10**, e1003504.

Luanpitpong, S., Talbott, S. J., Rojanasakul, Y., Nimmannit, U., Pongrakhananon, V., Wang, L. and Chanvorachote, P. (2010) Regulation of lung cancer cell migration and invasion by reactive oxygen species and caveolin-1. *Journal of Biological Chemistry,* **285**, 38832-38840.

Machida, S., Kondo, M., Jamison, J. A., Khan, N. W., Kononen, L. T., Sugawara, T., Bush, R. A. and Sieving, P. A. (2000) P23H rhodopsin transgenic rat: correlation of retinal function with histopathology. *Investigative Ophthalmology and Visual Science,* **41**, 3200-3209.

Magidson, V. and Khodjakov, A. (2013) Circumventing photodamage in live-cell microscopy. *Methods in cell biology,* **114**.

Manders, E. M. M., Visser, A. E., Koppen, A., de Leeuw, W. C., van Liere, R., Brakenhoff, G. J. and van Driel, R. (2003) Four-dimensional imaging of chromatin dynamics during the assembly of the interphase nucleus. *Chromosome Research,* **11**, 537-547.

Matsumoto, K., Ziober, B. L., Yao, C. C. and Kramer, R. H. (1995) Growth factor regulation of integrin-mediated cell motility. *Cancer Metastasis Rev,* **14**, 205-17.

McDonald, A., Harris, J., MacMillan, D., Dempster, J. and McConnell, G. (2012) Light-induced Ca(2+) transients observed in widefield epi-fluorescence microscopy of excitable cells. *Biomedical Optics Express,* **3**, 1266-1273.

McKeone, R., Wikstrom, M., Kiel, C. and Rakoczy, P. E. (2014) Assessing the correlation between mutant rhodopsin stability and the severity of retinitis pigmentosa. *Molecular Vision,* **20**, 183.

McKie, A., McHale, J., Keen, J., Tarttelin, E., Goliath, R., van Lith-Verhoeven, J., Greenberg, J., Ramesar, R., Hoyng, C., Cremers, F., Mackey, D., Bhattacharya, S., Bird, A., Markham, A. and Inglehearn, C. (2001) Mutations in the pre-mRNA splicing factor gene PRPC8 in autosomal dominant retinitis pigmentosa (RP13). *Hum Mol Genet,* **10**, 1555-1562.

Meijering, E. (2010) Neuron tracing in perspective. *Cytometry Part A,* **77**, 693-704.

Meijering, E. (2012) Cell segmentation: 50 years down the road [life sciences]. *IEEE Signal Processing Magazine,* **29**, 140-145.

Mendes, H. F. and Cheetham, M. E. (2008) Pharmacological manipulation of gain-of-function and dominant-negative mechanisms in rhodopsin retinitis pigmentosa. *Hum Mol Genet,* **17**, 3043-3054.

Minke, B. and Cook, B. (2002) TRP channel proteins and signal transduction. *Physiol Reviews,* **82**, 429-72.

Mirzadegan, T., Benko, G., Filipek, S. and Palczewski, K. (2003) Sequence analyses of G-protein-coupled receptors: similarities to rhodopsin. *Biochemistry,* **42**, 2759-67.

Mohler, W. A., Simske, J. S., Williams-Masson, E. M., Hardin, J. D. and White, J. G. (1998) Dynamics and ultrastructure of developmental cell fusions in the Caenorhabditis elegans hypodermis. *Current biology,* **8**, 1087-1091.

Murphy, R. F. (2010) Communicating subcellular distributions. *Cytometry Part A,* **77**, 686-692.

Murphy, R. F., Velliste, M. and Porreca, G. Robust classification of subcellular location patterns in fluorescence microscope images. Neural Networks for Signal Processing, 2002. Proceedings of the 2002 12th IEEE Workshop on 2002. IEEE, 67-76.

Murphy, R. F., Velliste, M. and Porreca, G. (2003) Robust numerical features for description and classification of subcellular location patterns in fluorescence microscope images. *Journal of VLSI signal processing systems for signal, image and video technology,* **35**, 311-321.

Nagai, T., Sawano, A., Park, E. S. and Miyawaki, A. Circularly permuted green fluorescent proteins engineered to sense Ca2+. Proceedings of the National Academy of Sciences March 13, 2001 2001. 3197-3202.

Nathans, J. and Hogness, D. S. (1984) Isolation, sequence analysis, and intron-exon arrangement of the gene encoding bovine rhodopsin. *Cell,* **34**, 807-814.

Neumann, B., Walter, T., Hériché, J.-K., Bulkescher, J., Erfle, H., Conrad, C., Rogers, P., Poser, I., Held, M., Liebel, U., Cetin, C., Sieckmann, F., Pau, G., Kabbe, R., Wünsche, A., Satagopam, V., Schmitz, M. H. A., Chapuis, C., Gerlich, D. W., Schneider, R., Eils, R., Huber, W., Peters, J.-M., Hyman, A. A., Durbin, R., Pepperkok, R. and Ellenberg, J. (2010) Phenotypic profiling of the human genome by time-lapse microscopy reveals cell division genes. *Nature,* **464**, 721-727.

Niethammer, P., Grabher, C., Look, A. T. and Mitchison, T. J. (2009) A tissue-scale gradient of hydrogen peroxide mediates rapid wound detection in zebrafish. *Nature,* **459**, 996-999.

Nishigaki, T., Wood, C. D., Shiba, K., Baba, S. A. and Darszon, A. (2006) Stroboscopic illumination using light-emitting diodes reduces phototoxicity in fluorescence cell imaging. *BioTechniques,* **41**, 191.

Noboyuki, O. (1979) A Threshold Selection Method from gray Level histogram. *IEEE Transactions on Systems, Man and Cybernetics,* **9**, 62-66.

Noorwez, S., Kuksa, V., Imanishi, Y., Zhu, L., Filipek, S. Ç., Palczewski, K. and Kaushal, S. (2003) Pharmacological Chaperone-mediated in Vivo Folding and Stabilization of the P23H-opsin Mutant Associated with Autosomal Dominant Retinitis Pigmentosa. *Journal of Biological Chemistry,* **278**, 14442-14450.

Noorwez, S., Reddy, R. and Kaushal, S. (2009) Calnexin Improves the Folding Efficiency of Mutant Rhodopsin in the Presence of Pharmacological Chaperone 11-cis-Retinal. *Journal of Biological Chemistry,* **284**, 33333-33342.

Noorwez, S. M., Ostrov, D. A., McDowell, J. H., Krebs, M. P. and Kaushal, S. (2008) A high-throughput screening method for small-molecule pharmacologic

chaperones of misfolded rhodopsin. *Investigative Ophthalmology and Visual Science,* **49**, 3224-3230.

Nyquist, H. (1928) Certain topics in telegraph transmission theory. *American Institute of Electrical Engineers,* **47**, 617-644.

Obara, B., Byun, J., Fedorov, D. and Manjunath, B. Automatic nuclei detection and data flow in Bisquik system. Workshop on Bio-Image Informatics: Biological Imaging, Computer Vision and Data Mining, Santa Barbara, CA, USA 2008. 17-18.

Obara, B., Jabeen, A., Fernandez, N. and Laissue, P. P. (2013) A novel method for quantified, superresolved, three-dimensional colocalisation of isotropic, fluorescent particles. *Histochemistry and cell biology,* **139**, 391-402.

Oda, Y., Hosokawa, N., Wada, I. and Nagata, K. (2003) EDEM As an Acceptor of Terminally Misfolded Glycoproteins Released from Calnexin. *Science,* **299**, 1394-1397.

Oh, K. T., Weleber, R. G., Lotery, A., Oh, D. M., Billingslea, A. M. and Stone, E. M. (2000) Description of a new mutation in rhodopsin, Pro23Ala, and comparison with electroretinographic and clinical characteristics of the Pro23His mutation. *Archives of ophthalmology,* **118**, 1269-76.

Olivari, S., Galli, C., Alanen, H., Ruddock, L. and Molinari, M. (2005) A novel stress-induced EDEM variant regulating endoplasmic reticulum-associated glycoprotein degradation. *The Journal of biological chemistry,* **280**, 2424-2428.

Oliver, J. D., Roderick, H. L., Llewellyn, D. H. and High, S. (1999) ERp57 functions as a subunit of specific complexes formed with the ER lectins calreticulin and calnexin. *Molecular biology of the cell,* **10**, 2573-2582.

Olsson, J. E., Gordon, J. W., Pawlyk, B. S., Roof, D., Hayes, A., Molday, R. S., Mukai, S., Cowley, G. S., Berson, E. L. and Dryja, T. P. (1992) Transgenic mice with a rhodopsin mutation (Pro23His): A mouse model of autosomal dominant retinitis pigmentosa. *Neuron,* **9**, 815-830.

Opefi, C. A., South, K., Reynolds, C. A., Smith, S. O. and Reeves, P. J. (2013) Retinitis Pigmentosa Mutants Provide Insight into the Role of the N-terminal Cap in Rhodopsin Folding, Structure, and Function. *The Journal of biological chemistry*, M113.483032--M113.483032-.

Openshaw, A., Branham, K. and Heckenlively, J. (2008) Understanding Retinitis Pigmentosa. University of Michigan Kellogg Eye Center.

Osborne, N. N., Li, G. Y., Ji, D., Mortiboys, H. J. and Jackson, S. (2008) Light affects mitochondria to cause apoptosis to cultured cells: possible relevance to ganglion cell death in certain optic neuropathies. *Journal of neurochemistry,* **105**, 2013-2028.

Palczewski, K., Kumasaka, T., Hori, T., Behnke, C. A., Motoshima, H., Fox, B. A., Le Trong, I., Teller, D. C., Okada, T., Stenkamp, R. E., Yamamoto, M. and Miyano, M. (2000) Crystal structure of rhodopsin: A G protein-coupled receptor. *Science,* **289**, 739-45.

Panieri, E. and Santoro, M. M. (2015) ROS signaling and redox biology in endothelial cells. *Cellular and Molecular Life Sciences,* **72**, 3281-3303.

Pawley, J. B. (1995) *Handbook of Biological Confocal Microscopy.* Springer.

Peirson, B. (2013) Wilhelm Johannsen's Genotype-Phenotype Distinction. *Embryo Project Encyclopedia*.

Peng, H. (2008) Bioimage informatics: a new area of engineering biology. *Bioinformatics,* **24**, 1827-1836.

Phelan, J. K. and Bok, D. (2000) A brief review of retinitis pigmentosa and the identified retinitis pigmentosa genes. *Molecular Vision,* **6**, 116-124.

Piccinini, F., Kiss, A. and Horvath, P. (2016) CellTracker (not only) for dummies. *Bioinformatics,* **32**, 955-957.

Pierce, K. L., Premont, R. T. and Lefkowitz, R. J. (2002) Seven-transmembrane receptors. *Nature reviews Molecular cell biology*, **3**, 639-50.

Poli, G., Leonarduzzi, G., Biasi, F. and Chiarpotto, E. (2004) Oxidative stress and cell signalling. *Current medicinal chemistry,* **11**, 1163-1182.

Preston, K. (1976) Computer processing of biomedical images. *Computer,* **9**, 54-68.

Pryor, W. A. (1986) Cancer and free radicals. *Antimutagenesis and Anticarcinogenesis Mechanisms.* Springer.

Rajan, R. S., Illing, M. E., Bence, N. F. and Kopito, R. R. (2001) Specificity in intracellular protein aggregation and inclusion body formation. *Proceedings of the National Academy of Sciences*, **98**, 13060-13065.

Rao, H., Wang, J., Tang, K., Pan, W. and Detre, J. (2006) Using CASL Perfusion fMRI to Image Natural Vision. *ISMRM 14th Scientific Meeting and Exhibition.* Washington, USA.

Rattner, A., Sun, H. and Nathans, J. (1999) Molecular genetics of human retinal disease. *Annual Review of Genetics,* **33**, 89-131.

Redmond, R. W. and Kochevar, I. E. (2006) Spatially resolved cellular responses to singlet oxygen. *Photochemistry and photobiology,* **82**, 1178-1186.

Redmond, T. M., Yu, S., Lee, E., Bok, D., Hamasaki, D., Chen, N., Goletz, P., Ma, J. X., Crouch, R. K. and Pfeifer, K. (1998) Rpe65 is necessary for production of 11-cis-vitamin A in the retinal visual cycle. *Nature Genetics,* **20**, 344-351.

Reeves, P. J., Kim, J.-M. and Khorana, H. G. (2002) Structure and function in rhodopsin: a tetracycline-inducible system in stable mammalian cell lines for high-level expression of opsin mutants. *Proceedings of the National Academy of Sciences of the United States of America,* **99**, 13413-8.

RetNet (2012) *RetNet* [Online]: https://sph.uth.edu/RetNet US National Library of Medicine, National Institutes of Health, Department of Health & Human Services. Last accessed 20 November.

Riley, P. (1994) Free radicals in biology: oxidative stress and the effects of ionizing radiation. *International journal of radiation biology,* **65**, 27-33.

Rizk, A., Paul, G., Incardona, P., Bugarski, M., Mansouri, M., Niemann, A., Ziegler, U., Berger, P. and Sbalzarini, I. F. (2014) Segmentation and quantification of subcellular structures in fluorescence microscopy images using Squassh. *Nature protocols,* **9**, 586-96.

Roehlecke, C., Schaller, A., Knels, L. and Funk, R. H. W. (2009) The influence of sublethal blue light exposure on human RPE cells. *Molecular Vision,* **15**, 1929-1938.

Rogalski, A. A., Bergmann, J. E. and Singer, S. (1984) Effect of microtubule assembly status on the intracellular processing and surface expression of an integral protein of the plasma membrane. *Journal of Cell Biology,* **99**, l01-l.

Roof, D. J., Adamian, M. and Hayes, A. (1994) Rhodopsin accumulation at abnormal sites in retinas of mice with a human P23H rhodopsin transgene. *Investigative Ophthalmology and Visual Science,* **35**, 4049-4062.

Rosenbaum, E. E., Hardie, R. C. and Colley, N. J. (2006) Calnexin is essential for rhodopsin maturation, Ca2+ regulation, and photoreceptor cell survival. *Neuron,* **49**, 229-41.

Russ, J. C. (2004) Seeing the scientific image. *Proceedings of the Royal Microscopical Society,* **39**, 1-15.

Russ, J. C. and Woods, R. P. (1995) *The image processing handbook.*

Saetzler, R., Jallo, J., Lehr, H., Philips, C., Vasthare, U., Arfors, K. and Tuma, R. (1997) Intravital fluorescence microscopy: impact of light-induced phototoxicity on adhesion of fluorescently labeled leukocytes. *Journal of Histochemistry and Cytochemistry,* **45**, 505-513.

Sakami, S., Kolesnikov, A. V., Kefalov, V. J. and Palczewski, K. (2014) P23H opsin knock-in mice reveal a novel step in retinal rod disc morphogenesis. *Hum Mol Genet,* **23**, 1723-1741.

Sakmar, T. P. and Huber, T. (2009) Rhodopsin. *New Encyclopedia of Neuroscience,* **8**.

Saliba, R., Munro, P., Luthert, P. and Cheetham, M. (2002) The cellular fate of mutant rhodopsin: quality control, degradation and aggresome formation. *Journal of cell science,* **115**, 2907-2918.

Schnell, U., Dijk, F., Sjollema, K. A. and Giepmans, B. N. (2012) Immunolabeling artifacts and the need for live-cell imaging. *Nature Methods,* **9**, 152-158.

Schrag, J. D., Bergeron, J. J. M., Li, Y., Borisova, S., Hahn, M., Thomas, D. Y. and Cygler, M. (2001) The Structure of Calnexin, an ER Chaperone Involved in Quality Control of Protein Folding. *Molecular cell,* **8**, 633-644.

Schrodinger, LLC (2015) The PyMOL Molecular Graphics System, Version 1.8.

Sezgin, M. (2004) Survey over image thresholding techniques and quantitative performance evaluation. *Journal of Electronic imaging,* **13**, 146-168.

Shannon, C. E. (1949) Communication in the presence of noise. *Proceedings of the IRE,* **37**, 10-21.

Smith, K. (2013) *The science of photobiology.* Springer Science & Business Media.

Smrcka, A. (2008) G protein βγ subunits: central mediators of G protein-coupled receptor signaling. *Cellular and Molecular Life Sciences,* **65**, 2191-2214.

South, K. (2012) *Constitutively active rhodopsin mutants: Biochemical and structural characterisation.* dissertation.: PhD Thesis.

Spielmann, H. (1994) In vitro phototoxicity testing. *Alternatives To Laboratory Animals,* **22**, 314-348.

Spielmann, H., Müller, L., Averbeck, D., Balls, M., Brendler-Schwaab, S., Castell, J. V., Curren, R., De Silva, O., Gibbs, N. and Liebsch, M. The second ECVAM workshop on phototoxicity testing. The Report and Recommendations of ECVAM Workshop 2000. 777-814.

Stadler, C., Rexhepaj, E., Singan, V. R., Murphy, R. F., Pepperkok, R., Uhlén, M., Simpson, J. C. and Lundberg, E. (2013) Immunofluorescence and fluorescent-protein tagging show high correlation for protein localization in mammalian cells. *Nature Methods*.

Stuurman, N. and Swedlow, J. R. (2012) Software tools, data structures, and interfaces for microscope imaging. *Cold Spring Harb Protoc,* **2012**, 50-61.

Sung, C. H., Davenport, C. M., Hennessey, J. C., Maumenee, I. H., Jacobson, S. G., Heckenlively, J. R., Nowakowski, R., Fishman, G., Gouras, P. and Nathans, J. (1991a) Rhodopsin mutations in autosomal dominant retinitis pigmentosa. *Proceedings of the National Academy of Sciences,* **88**, 6481-6485.

Sung, C. H., Davenport, C. M. and Nathans, J. (1993) Rhodopsin mutations responsible for autosomal dominant retinitis pigmentosa. Clustering of functional classes along the polypeptide chain. *The Journal of Biological Chemistry.*, **268**, 26645-26649.

Sung, C. H., Schneider, B. G., Agarwal, N., Papermaster, D. S. and Nathans, J. (1991b) Functional heterogeneity of mutant rhodopsins responsible for autosomal dominant retinitis pigmentosa. *Proceedings of the National Academy of Sciences*, **88**, 8840-8844.

Svoboda, K. and Block, S. M. (1994) Biological applications of optical forces. *Annual review of biophysics and biomolecular structure*, **23**, 247-285.

Teferedegne, B., Macauley, J., Foseh, G., Dragunsky, E., Chumakov, K., Murata, H., Peden, K. and Lewis, A. M. (2014) MicroRNAs as potential biomarkers for VERO cell tumorigenicity. *Vaccine*, **32**, 4799-4805.

Terakita, A. (2005) The opsins. *Genome Biology*, **6**, 213.

Thomas, P. and Smart, T. (2005) HEK293 cell line: a vehicle for the expression of recombinant proteins. *Journal of Pharmacological and Toxicological Methods*, **51**, 187-200.

Tinevez, J.-Y., Dragavon, J., Baba-Aissa, L., Roux, P., Perret, E., Canivet, A., Galy, V. and Shorte, S. (2012) A quantitative method for measuring phototoxicity of a live cell imaging microscope. *Methods in Enzymology*, **506**, 291-309.

Tsai, B., Ye, Y. and Rapoport, T. A. (2002) Retro-translocation of proteins from the endoplasmic reticulum into the cytosol. *Nature Reviews. Molecular Cell Biology*, **3**, 246-255.

Tukey, J. W. (1977) Box-and-whisker plots. *Exploratory Data Analysis*, 39-43.

Ushioda, R., Hoseki, J., Araki, K., Jansen, G., Thomas, D. and Nagata, K. (2008) ERdj5 Is Required as a Disulfide Reductase for Degradation of Misfolded Proteins in the ER. *Science*, **321**, 569-572.

Van Raamsdonk, J. M. and Hekimi, S. (2010) Reactive oxygen species and aging in Caenorhabditis elegans: causal or casual relationship? *Antioxidants and Redox Signaling*, **13**, 1911-1953.

von Bartheld, C. S. and Wouters, F. S. (2015) Quantitative techniques for imaging cells and tissues. *Cell and tissue research*, **360**, 1.

Wagner, M., Weber, P., Bruns, T., Strauss, W. S., Wittig, R. and Schneckenburger, H. (2010) Light dose is a limiting factor to maintain cell viability in fluorescence microscopy and single molecule detection. *International journal of molecular sciences*, **11**, 956-966.

Waters, J. C. (2009) Accuracy and precision in quantitative fluorescence microscopy. *Journal of Cell Biology*.

Winslow, T. (2007) *Anatomy of the human eye* [Online]: http://teresewinslow.com/portshow.asp.

Wojtovich, A. P., Nadtochiy, S. M., Brookes, P. S. and Nehrke, K. (2012) Ischemic preconditioning: the role of mitochondria and aging. *Experimental gerontology*, **47**, 1-7.

Wolpert, L. (1995) Evolution of the cell theory. *Philosophical Transactions of the Royal Society B: Biological Sciences*, **349**, 227-33.

Wood, J. P., Lascaratos, G., Bron, A. J. and Osborne, N. N. (2007) The influence of visible light exposure on cultured RGC-5 cells. *Molecular Vision*.

Wright, A., Bubb, W. A., Hawkins, C. L. and Davies, M. J. (2002) Singlet Oxygen–mediated Protein Oxidation: Evidence for the Formation of Reactive Side

Chain Peroxides on Tyrosine Residues. *Photochemistry and photobiology,* **76**, 35-46.

Xue, L., Gollapalli, D. R., Maiti, P., Jahng, W. J. and Rando, R. R. (2004) A palmitoylation switch mechanism in the regulation of the visual cycle. *Cell,* **117**, 761-771.

Yoshida, H., Matsui, T., Hosokawa, N., Kaufman, R., Nagata, K. and Mori, K. (2003) A time-dependent phase shift in the mammalian unfolded protein response. *Developmental Cell,* **4**, 265-271.

Youn, H., Cullen, A., Chou, B. and Sivak, J. (2010) Phototoxicity of ultraviolet (UV) radiation: evaluation of UV-blocking efficiency of intraocular lens (IOL) materials using retinal cell culture and in vitro bioassays. *Open Toxicol Journal,* **4**, 3-20.

Zdolsek, J. M., Olsson, G. M. and Brunk, U. T. (1990) Photooxidative damage to lysosomes of cultured macrophages by acridine orange. *Photochemistry and photobiology,* **51**, 67-76.

Zhou, X. and Wong, S. T. (2006) Informatics challenges of high-throughput microscopy. *IEEE Signal Processing Magazine,* **23**, 63-72.

Appendices

Appendix A. Control sample for rhodopsin-GFP transfection experiments using GFP-tagged empty vector.

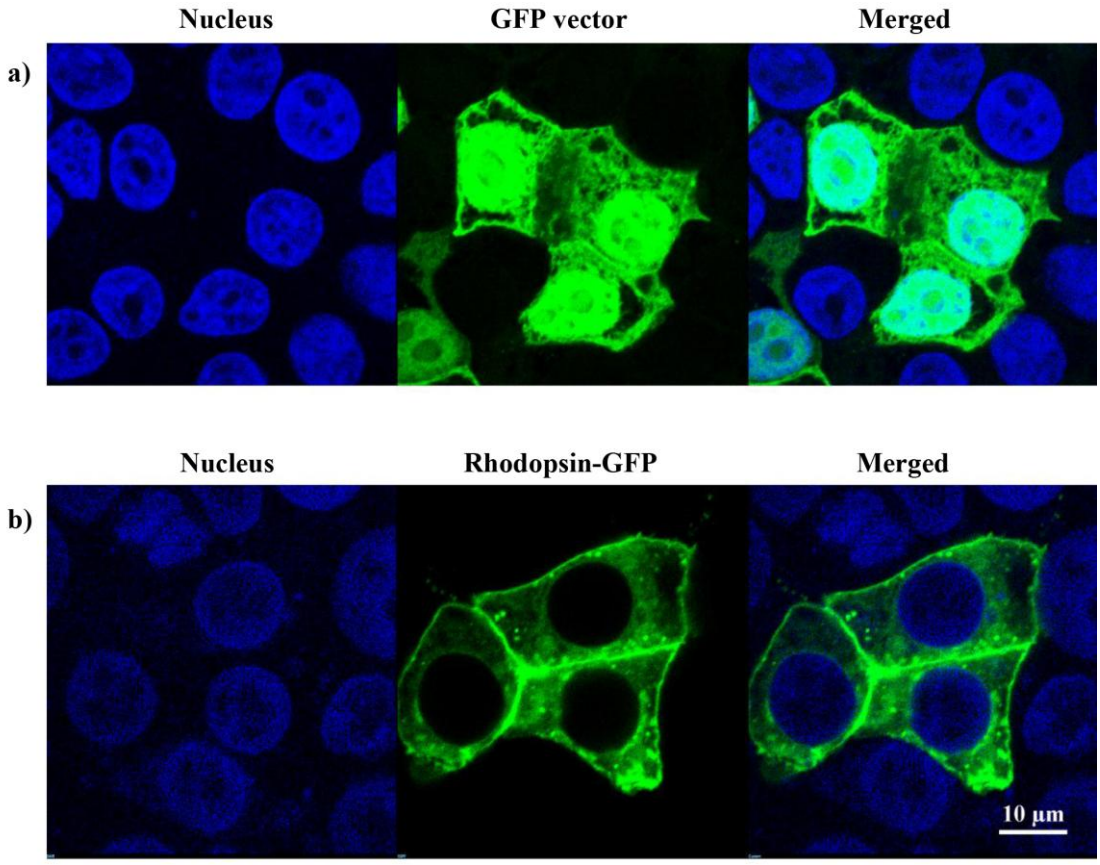

Figure A-1 Fixed HEK293S cells transfected with GFP, nuclei were stained with DAPI.

a) HEK293S cells transiently transfected with GFP tagged empty vector (control). GFP signals are located on the entire cell including the nucleus.

b) Stable HEK293S cells expressing wild-type rhodopsin-GFP. Rhodopsin-GFP signals are located on the cytoplasm and on the plasma membrane.

Appendix B. Control samples for CNX-mCherry transfection experiments using mCherry-tagged empty vector.

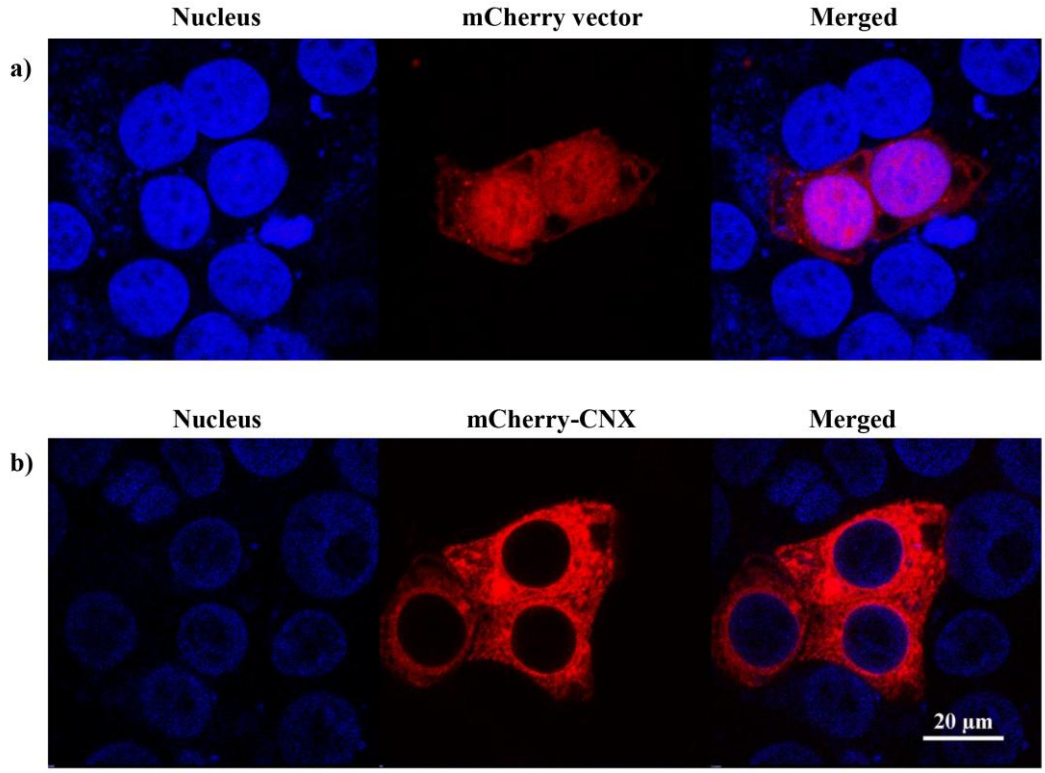

Figure A-2 Fixed GMK cells transfected with mCherry, nuclei were stained with DAPI.

a) GMK cells transiently transfected with mCherry empty vector (control). The red mCherry signals are located on the entire cell including the nucleus.

b) GMK cells transienty transfected with CNX-mCherry. The red mCherry signals are located around the nucleus and on the cytoplasm.

Appendix C. Improve immunofluorescence staining with Sequential fixation

Sequential fixation increases signal to nose ratio as an outcome of efficient antibody antigen binding. Figure A-3 shows the efficiency of antibody staining with calnexin-mAb after using two different cells fixation protocols. In Figure A-3a cells were fixed with formaldehyde and permeabilised with 0.5 % Triton X100. Whereas, in Figure A-3b cells were fixed with formaldehyde and then permeabilised by methanol. Using of methanol in our fixation protocol to permeabilised the cells cconsiderably improves immunofluorescence staining as it facilitate the antibody binding to it antigen, preserve the cellular structural integrity, therefore give strength to the fluorescence signal intensity by increasing signal to noise ratio and lead to reliable segmentation and proper quantification.

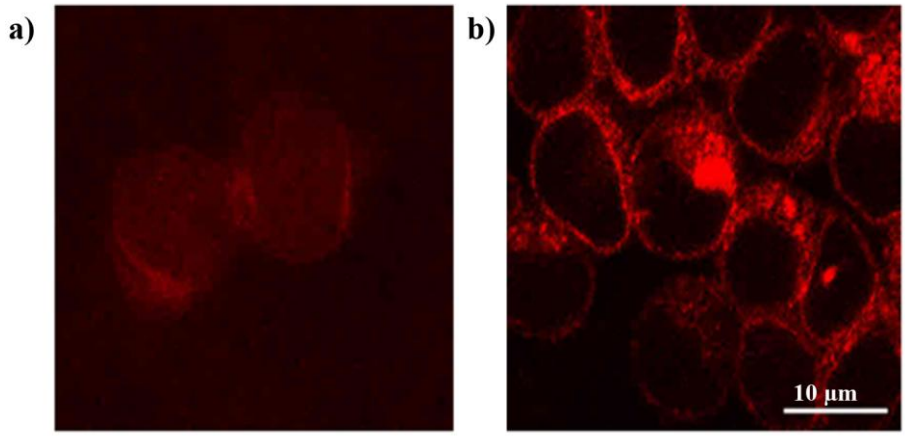

Figure A-3 Immunostaining of HEK293S with calnexin-mAb

a) Formaldehyde fixation without methanol.

b) Sequential fixation using formaldehyde and methanol.

Appendix D. Negative control sample for immunofluorescence staining

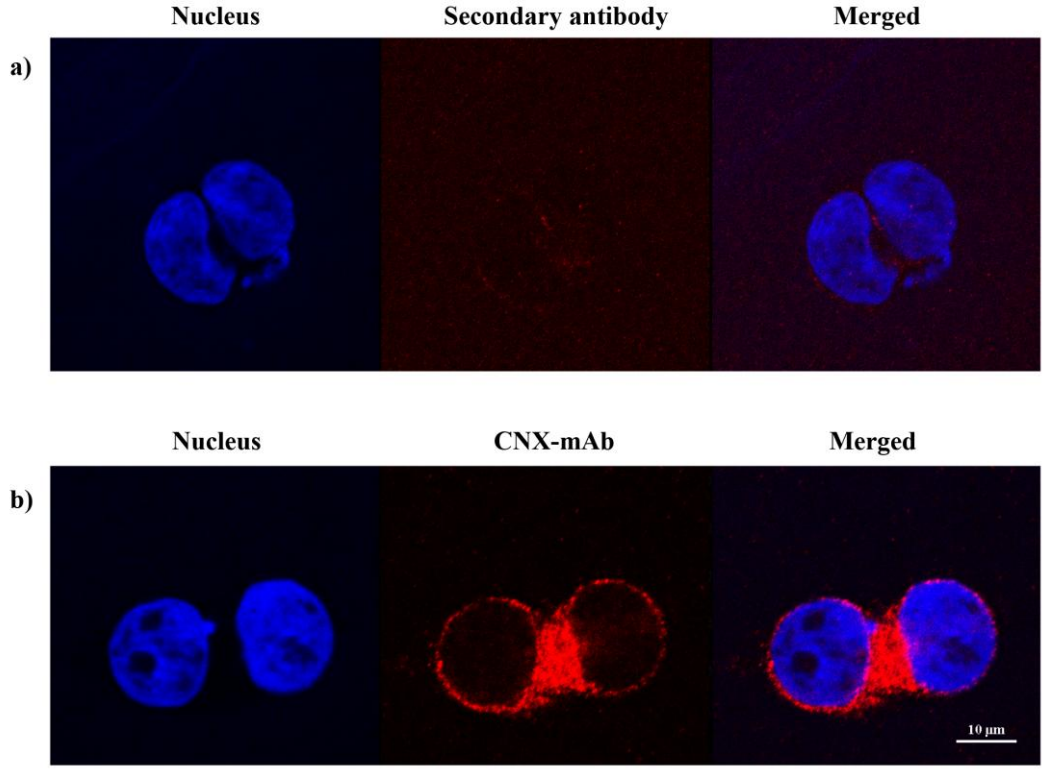

Figure A-4 Immunofluorescence staining of fixed HEK293S cells, nuclei are stained with DAPI.

a) Negative control cells are fixed and incubated with the secondary antibody without being incubated with theprimary antibody. No clear signals are recorded.

b) Cells were fixed and incubated with both the primary antibody and the secondary antibody CNX-mAb.